MEASUREMENT OF SCATTERING LENGTHS USING $K_{\pi 3}$ DECAY

A Thesis Submitted to the College of

Graduate Studies and Research

in Partial Fulfillment of the Requirements

for the Degree of Doctor of Philosophy

in the Deptartment of Physics and Engineering Physics

University of Saskatchewan

Saskatoon

By

Troy Baker

Spring 2000

Abstract

The determination of N-N and $\pi\pi$ scattering lengths is of fundamental importance in the studies of hadron dynamics. A direct measurement of $\pi\pi$ scattering lengths is impossible due to a lack of processes with just two pions in both the initial and final state. Therefore indirect methods must be used. In the past, $\pi N \rightarrow \pi\pi N$ and K_{e4} decay[1] have been employed. These analyses are complicated due to problems of a) extrapolation to threshold, b) contribution of higher multipoles, and c) inelasticity effects. In this thesis we present a novel analysis of stopped $K^+_{\pi 3}$ decays ($K^+ \rightarrow \pi^+\pi^0\pi^0$) to deduce the scattering lengths (a_0^0 and a_0^2) in a nearly model independent way. The model of Sawyer and Wali[2], incorporating Chew and Mandelstam's[3] result for $\pi\pi$ scattering, was used to analyze the data. The data is a kinematically complete determination of $K_{\pi 3}$ decays, a byproduct of the T-violation experiment at KEK[4]. It is fit to an amplitude

$$A^{\tau'}(s_1, s_2, s_3) = -\frac{\lambda}{2\lambda_\pi}\left(2\lambda_\pi + \frac{1}{2}\left[t_0^2(s_1) + t_0^2(s_2)\right] + \frac{1}{3}\left[t_0^0(s_3) - t_0^2(s_3)\right]\right) \qquad (0.1)$$

where λ, λ_π are the $K\pi \rightarrow \pi\pi$ and $\pi\pi \rightarrow \pi\pi$ coupling constants, s_i are the center of mass energies of pion pairs and, t_I $(I = 0, 2)$ is the S wave scattering amplitude for isospin I given by the Roy equation: $t_I(s) = \sqrt{\frac{s}{s-4m_\pi^2}} e^{i\delta(s)} \sin\delta(s)$. Here $\delta(s)$ is phase shift which depends on the scattering length, a. We deduce $\pi^+\pi^0$ $(\pi^0\pi^0)$ scattering lengths to be $a_0^0 = 0.199 \pm 0.003(stat) \pm 0.002(syst)$ and $a_0^2 =$

$-0.0285 \pm 0.0008(stat)^{+0.0012}_{-0.0007}(syst)$. This also is the first experimental determination of Weinberg's universal curve[5]

$\mathfrak{W} = 2a_0^0 - 5a_0^2 = 0.540 \pm 0.007(stat)^{+0.005}_{-0.007}(syst)$.

Acknowledgements

I would like to thank C. Rangacharyulu for his guidance and advice in my post-graduate work. I would also like to extend gratitude to J. Imazato, Y. Kuno, M. Aoki, Y. Kudenko, A. Ivashkin, O. Mineev, M. Khabibullin, J. Macdonald, M. Hasinoff, Y.-M. Shin, P. Depommier, S. Shimizu, T. Yokoi, Y. Igarashi, T. Ikeda, M. Blecher, and G. Y. Lim for their excellent work and making this possible. I would also like to thank my parents Mary and George Baker for their support.

I would like to thank the Department of Physics and Engineering Physics for financial support. My thesis work was also supported by the Herzberg Scholarship.

Contents

List of Tables

List of Figures

Chapter 1

Introduction

1.1 Classical Concepts

The essence of physics is the study of interactions. In particle physics, this includes detection of particles (interaction between the particle and detector), study of decay processes (decay is one type of interaction), or scattering processes. In solid state physics, this includes superconductivity (Cooper pairs) and lasers (interaction of stimulating photon with lasing material).

A fundamental characteristic of an interaction is the strength. In classical physics, parameters such as mean free path and index of refraction have been used. The mean free path of a particle is defined as the average distance the particle travels before it hits (interacts) with another particle. The index of refraction of a medium is the ratio of the speed of a wave in vacuum to the speed in the medium. If the interaction is weak, then a particle does not interact with its neighbours very often. Thus, the

interaction will have a large mean free path. This means that the particle will travel in nearly a straight line and thus it's effective speed is close to the speed in a vacuum, *i.e.* an index of refraction that is close to unity. Similarly, a strong interaction will have a small mean free path and a large index of refraction.

The concept of cross section is common to both classical as well as nuclear physics. The cross section of a point particle scattering from a hard sphere of radius a is given by

$$\sigma = 4\pi a^2 \tag{1.1}$$

In nuclear physics, S wave scattering is given by

$$\sigma = \frac{4\pi}{k^2} \sin^2 \delta(k) \tag{1.2}$$

where k is the momentum of scattered particle and $\delta(k)$ is the known as the phase shift. At low energies, the cross section approaches a constant given by

$$\sigma = 4\pi a^2 \tag{1.3}$$

where a is the scattering length. In general, the scattering length if often denoted a_L^I where the superscript, I, is the isospin and the subscript, L, is the angular momentum of the scattering process. As can be seen, this equation is exactly the same as the classical definition. Therefore, the scattering length is related to the classical radius of the interacting particles. Note, however, that the scattering is related to the strength and range of the interaction and not the actual size. Also, the sign of the scattering length yields information on the presence or absence of a bound state. As discussed in [16], the scattering length can be related to the index of refraction as

$$n = 1 - \frac{2\pi N a}{k^2} \tag{1.4}$$

where N is the number of nuclei per unit volume.

1.2 Hadron Dynamics

The theory of hadron interactions is quantum chromodynamics (QCD). This theory is similar to quantum electrodynamics (QED), a successful model of electromagnetic interactions. There are two features that make QCD calculations more difficult. The first is the particles which mediate the colour force, namely gluons, have a colour charge and therefore can interact with other gluons whereas the photon, the electromagnetic mediator, has no electric charge. The second property is the coupling constant. At small distances, or high energies, the coupling constant is small and perturbative methods can be used for QCD calculations. However, at larger distances, or low energies, non-perturbative methods must be used since the coupling constant becomes very large. One method uses low energy effective models, such as chiral perturbation theory (χPT), for these calculations. Low energy properties such as scattering lengths are important parameters of these theories.

The pion, as the lowest mass meson, commonly occurs in the study of hadron interactions and decays. For example, the strong force is primarily mediated by the pion. Also resonance production and hadronic decays are likely to produce multi-pion final states, either directly (*i.e.* $\pi N \to \pi\pi N$, $\rho \to \pi\pi$) or indirectly (*i.e.* $\eta'(958) \to \rho\gamma$). The resulting final state in many cases is influenced by π interactions and in

particular $\pi\pi$ scattering.

1.3 Previous Measurements

1.3.1 $\pi N \rightarrow \pi\pi N$

The majority of these scattering length measurements have been conducted using a pion beam incident on a hydrogen target to produce an additional pion. Most measurements use the method of Chew and Low[17] to determine the scattering lengths. Two recent measurements were done by Alekseeva[18] and Kermani[19]. Alekseeva measured $\pi\pi$ scattering for center of mass energies in the range 300 to 1200 MeV. The result of this experiment yielded $a_0^0 = 0.24 \pm 0.03$. The other recent measurement was done at TRIUMF by Kermani. This experiment used a pion beam with energies down to 223 MeV. Their result was $a_0^0 = 0.204 \pm 0.014(stat) \pm 0.008(syst)$.

A second method of analyzing $\pi N \rightarrow \pi\pi N$ was proposed by Olsson and Turner[20]. This method was used in the measurement of Lowe[21]. Their measurement of $\pi^- p \rightarrow \pi^0\pi^0$ found $a_0^0 = 0.207 \pm 0.028$ and $a_0^2 = -0.022 \pm 0.011$.

1.3.2 $K^+ \rightarrow \pi^+\pi^- e^+\nu$ (K_{e4})

A single measurement, done by Rosselet[1], with no baryons in the final state has been done using the decay $K^+ \rightarrow \pi^+\pi^- e^+\nu$. This experiment used a 2.8 GeV/c K^+ beam and detected the three charged decay products. About 30000 K_{e4} events were used to determine the phase shifts. The scattering length a_0^0 was extracted using the

phenomenological model of Basdevant, *et. al.*[22]. The value reported in the original paper was $a_0^0 = 0.28 \pm 0.05$. Modern papers quote the value found in Nagels[23], $a_0^0 = 0.26 \pm 0.05$.

Chapter 2

Theory of $\pi\pi$ Scattering

> It has become obvious in recent times that no further substantial progress will be made in the theory of strong interaction phenomena involving pions and nucleons until *something* is understood about the pion-pion interaction. — Chew and Mandelstam[3]

Interest in $\pi\pi$ scattering started in the late '50s. The initial theoretical work (Chew and Low[17], Chew and Mandelstam[3]) simply described the form of the scattering amplitudes. The method of Chew and Low (using $a + b \rightarrow c + d + e$ to measure d-e scattering) has been the basis for most of the measurements of the $\pi\pi$ scattering lengths as described in Section 1.3. The first attempt to predict these scattering lengths was made by Weinberg[5] in 1966. Over the past three decades various other models[9, 10, 11, 12, 13, 24, 14] have been used to predict the scattering lengths. Most of these calculations have demonstrated a limiting case in which Weinberg's result is recovered. Section 2.1 gives a general discussion of $\pi\pi$ scattering.

Various models and scattering length predictions are discussed in Section 2.2. The discussion relating $K_{\pi 3}$ decay to $\pi\pi$ scattering is contained in section 2.3.

2.1 $\pi\pi \rightarrow \pi\pi$ scattering

2.1.1 Scattering Amplitude and Scattering Length

The general amplitude for $\pi\pi$ scattering can be written as

$$\langle \pi_c \pi_d \,|\mathfrak{M}|\, \pi_a \pi_b \rangle = \delta_{ab}\delta_{cd} A(s,t,u) + \delta_{ac}\delta_{bd} A(t,u,s) + \delta_{ad}\delta_{bc} A(u,s,t) \tag{2.1}$$

where the subscripts a,b,c, and d are isospin indices, and

$$s = (p_a + p_b)^2 = (p_c + p_d)^2 \tag{2.2}$$

$$t = (p_a - p_c)^2 = (p_d - p_b)^2 \tag{2.3}$$

$$u = (p_a - p_d)^2 = (p_c - p_b)^2. \tag{2.4}$$

are the Mandelstam variables which satisfy $s+t+u = 4m_\pi^2$. The form of the function A is constrained by crossing symmetry, isospin conservation and Bose symmetry. Bose symmetry further requires that the function $A(x,y,z)$ be symmetric in the last two arguments. The general form of the scattering amplitude can be split into three components according to isospin

$$T^0(s,t) = 3A(s,t,u) + A(t,u,s) + A(u,s,t) \tag{2.5}$$

$$T^1(s,t) = A(t,u,s) - A(u,s,t)$$

$$T^2(s,t) = A(t,u,s) + A(u,s,t)$$

where T^I denotes the scattering amplitude for isospin I. Similarly, the partial wave expansion can be used to write scattering amplitudes with definite angular momentum.

$$T^I(s,t) = 32\pi \sum_{L=0}^{\infty} (2L+1) P_L(\cos\theta) t_L^I(q) \tag{2.6}$$

where t_L^I are scattering amplitudes for isospin I and angular momentum L. Note that the right hand side uses the parameterization $q = \frac{s-4m_\pi^2}{2}$ and $\cos\theta = 1 + \frac{2t}{s-4m_\pi^2}$ which are the momentum transfer and the scattering angle respectively. Implicit in the above sum is the constraint, from Bose symmetry, that L and I are either both odd or both even. The unitarity condition[25, 3] is

$$\Im\, t_L^I(q) = \frac{q}{\sqrt{q^2+m^2}} \left| t_L^I(q) \right|^2 \tag{2.7}$$

where $\Im\, z$ is the imaginary part of z. The scattering amplitude is then

$$t_L^I(q) = \frac{\sqrt{q^2+m_\pi^2}}{q} e^{i\delta_L^I(q)} \sin\delta_L^I(q) \tag{2.8}$$

where δ_L^I is the phase shift. The scattering amplitude at threshold can be defined as

$$t_L^I(0) = \lim_{q\to 0} t_L^I(q) = m_\pi \left. \frac{d\delta_L^I}{dq} \right|_{q=0} \tag{2.9}$$

Noting that the scattering length a_L^I is by definition the derivative of the phase shift, the above equation is a simple relation between scattering length and scattering amplitude at threshold ($q = 0$ or $s = 4m_\pi^2$). Using all of the above information and using the approximation that only S-wave ($L = 0$) contributes, gives the relations

$$a_0^0 = \frac{3A(4m_\pi^2,0,0) + A(0,0,4m_\pi^2) + A(0,4m_\pi^2,0)}{32\pi m_\pi} \tag{2.10a}$$

$$a_0^2 = \frac{A(0,0,4m_\pi^2) + A(0,4m_\pi^2,0)}{32\pi m_\pi}. \tag{2.10b}$$

In general, the scattering amplitudes do contain higher angular momentum states (P-, D-, etc. waves), however these terms are negligible at threshold and thus do not contribute to the scattering lengths. This measurement of $\pi\pi$ scattering using stopped $K_{\pi 3}$ decay limits the pions to very near threshold which also limits the contributions from higher waves.

2.1.2 Chew and Mandelstam: Integral Equations

Integral equations for $\pi\pi$ scattering amplitudes have been derived by Chew and Mandelstam[3] and Roy[26]. Chew and Mandelstam start with the once subtracted dispersion relations

$$t_0^I(\nu) = c_I + \frac{\nu - \nu_{sym}}{\pi}\int_{-\infty}^{-1} \frac{\Im t_L^I(\nu')\, d\nu'}{(\nu' - \nu)(\nu' - \nu_{sym})} + \frac{\nu - \nu_{sym}}{\pi}\int_0^{\infty} \frac{\Im t_L^I(\nu')\, d\nu'}{(\nu' - \nu)(\nu' - \nu_{sym})} \tag{2.11}$$

introducing the dimensionless parameter $\nu = \frac{s}{4m_\pi^2} - 1$. The subtraction point is $s = t = u = 4m_\pi^2/3$ which is equivalent to $\nu_{sym} = -2/3$. The first integral is referred to as the "left hand cut" or "unphysical" integral and the second as "right hand cut" or "physical" integral. The subtraction constants c_I are related to the $\pi\pi \rightarrow \pi\pi$ coupling constant λ_π.

$$c_0 = -5\lambda_\pi \tag{2.12}$$

$$c_2 = -2\lambda_\pi \tag{2.13}$$

For the physical integral, the unitarity relation (2.7) can be used to express the imaginary, or absorptive, part of the amplitude in terms of the squared magnitude of

amplitude. Although the unitarity condition does not hold for the unphysical integral, Chew and Mandelstam show that absorptive parts can be expressed as the absorptive parts of amplitudes in the physical region using the isospin crossing matrix.

$$\Im\ t_0^I(\nu) = \int_0^{-\nu-1} \frac{d\nu'}{\nu} \sum_{I'} \beta_{II'} \Im\ t_0^{I'}(\nu') \tag{2.14}$$

for $\nu < -1$ and where $\beta_{II'}$ is twice the usual crossing matrix

$$\beta_{II'} = \begin{pmatrix} \frac{2}{3} & 2 & \frac{10}{3} \\ \frac{2}{3} & 1 & \frac{-5}{3} \\ \frac{2}{3} & -1 & \frac{1}{3} \end{pmatrix} \tag{2.15}$$

Since the amplitude on the right in (2.14) is in the physical region, the unitarity relation now applies. Putting together the three equations (2.14), (2.7), and (2.11) allows the two integral equations of out interest to be written as

$$t_0^0(\nu) = -5\lambda_\pi + R(t_0^{0\dagger} t_0^0; \nu) + L(\frac{2}{3} t_0^{0\dagger} t_0^0 + \frac{10}{3} t_0^{2\dagger} t_0^2; \nu) \tag{2.16}$$

$$t_0^2(\nu) = -2\lambda_\pi + R(t_0^{2\dagger} t_0^2; \nu) + L(\frac{2}{3} t_0^{0\dagger} t_0^0 + \frac{1}{3} t_0^{2\dagger} t_0^2; \nu) \tag{2.17}$$

where $R(x, \nu)$ and $L(x, \nu)$ are the right and left hand integrals respectively. As will be shown in Section 2.3, integral equations of similar forms will be found for $K\pi \to \pi\pi$ scattering.

2.2 Models of $\pi\pi$ Scattering

In the previous section, the scattering lengths a_0^I were related to the amplitude $A(s, t, u)$ in equation 2.10. Therefore, if the explicit form $A(s, t, u)$ in a particular

Table 2.1: The scattering lengths and Weinberg's universal curve $\mathfrak{W} = 2a_0^0 - 5a_0^2$ predicted in various models. The last column indicates the section where the model is described.

Model	a_0^0	a_0^2	$\mathfrak{W}$	Section
Weinberg[5]	0.16	-0.046	0.56	2.2.1
χPT[9]	0.20	-0.042	0.61	2.2.2
NJL - SU(2)[12]	0.22	-0.074	0.81	2.2.3
NJL - SU(3)[13]	0.26	-0.062	0.83	2.2.3

model can be found, then scattering lengths predictions easily follow. This section will review some of the various models of $\pi\pi$ scattering. Table 2.1 summarizes the various theoretical predictions.

2.2.1 Weinberg: Current Algebra

To proceed further, some assumptions must be made about the explicit form of the function $A(x, y, z)$. In Weinberg's calculation[5], $A(x, y, z)$ is expanded to the second order in momentum.

$$A(s, t, u) = B_0 + B_1(t + u) + B_2 s + \cdots \tag{2.18}$$

Although primarily interested in the physical region, the above function is not constrained to this region. Weinberg considers various limits in the off mass shell region to determine the constants B_i $(i = 1, 2, 3)$. In this case, off mass shell means the constraint $p_\pi^2 = m_\pi^2$ is lifted as well as $s + t + u = 4m_\pi^2$. In the limiting case where two of the four-momentum go to zero the scattering amplitude (2.1) becomes

$$\mathfrak{M} = M^{(0)} - 8\left(\frac{g_V}{F_\pi}\right)^2 \frac{(u - s)}{2}(\delta_{ad}\delta_{bc} - \delta_{ab}\delta_{cd}) \tag{2.19}$$

where g_V is the coupling between the pion field and the divergence of the pion field and $F_\pi = 93.4$ MeV is the pion decay constant, and $M^{(0)}$ is a constant. Comparing this with (2.1), (2.18) and (2.10) along with the length scale given by the Goldberger-Tremain relation[1] as $L = \frac{g_V^2 m_\pi}{2\pi F_\pi^2} = 0.115 m_\pi^{-1}$ yields the now famous Weinberg universal curve[2]

$$\mathfrak{W} = 2a_0^0 - 5a_0^2 = 6L = 0.69 m_\pi^{-1} \tag{2.20}$$

A second constraint comes from the Adler self consistency which yields the vanishing of the matrix element for the case $s = t = u = m_\pi^2$. This is the limit of what pure current algebra can say about $\pi\pi$ scattering. In order to complete the calculation, further assumptions of pion properties are required. The initial assumption was that the pion field divergences formed a chiral quadruplet with an isoscalar field.[3] This was not the only assumption made for the transformation of the pion field[6, 7, 27], but it is now considered to be the correct one since it is equivalent to chiral perturbation theory (χPT) and is the limiting case nearly all models have. This final piece of information yields the ratio of scattering lengths to be $\frac{a_0^0}{a_0^2} = -\frac{7}{2}$. Combining this with (2.20) yields the prediction $a_0^0 = 0.20$ and $a_0^2 = -0.06$ as quoted in [5]. Recent papers quote this as $a_0^0 = 0.16$ and $a_0^2 = -0.046$ using the modern value of $\mathfrak{W}$.

[1] This is the value quoted in Weinberg's original paper[5]. However in modern papers such as [15] this length has been changed to $0.093 m_\pi^{-1}$.

[2] Similar to the previous footnote, modern papers quote this value as 0.56

[3] This isoscalar field is now associated with the σ meson. However in Weinberg's paper[5] he states that the σ is "some scalar field which may or may not have something to do with a real 0^+ π-π resonance".

2.2.2 Chiral Perturbation Theory

The basic model[28, 29] starts with $SU(2)_L \times SU(2)_R$ symmetric Lagrangian, where the left handed and right handed fields transform independently. It is assumed that the ground state breaks this symmetry (spontaneous symmetry breaking) which yields 3 massless, pseudoscalar Goldstone bosons[30]. However, a non-zero quark mass breaks this chiral symmetry (dynamical symmetry breaking). Since the quark masses are small, this can be treated as a perturbation. One of the effects of quark mass is to give the Goldstone bosons, that is the pions, a small mass. The leading order (tree level or order p^2) of chiral perturbation theory (χPT) Lagrangian is

$$\mathfrak{L} = \frac{F^2}{4}\mathrm{Tr}\left[D_\mu U^\dagger D^\mu U + 2BMU + 2U^\dagger BM\right] \tag{2.21}$$

where F and B are constants not determined by the theory, $M = \mathrm{diag}(m_u, m_d)$ is the quark mass matrix, and $U = \exp(i\sigma_k\phi^k/F)$ contains the pion fields ϕ^k $(k = 1, 2, 3)$. The constant F is the pseudoscalar decay constant, and BM is fixed by Gell-Mann–Okubo mass relations such as $m^2_{\pi^+} = B(m_u + m_d)$. At this order, χPT yields identical predictions to Weinberg. The next order (one loop or order p^4) of χPT introduces 12 new constants of which only 10 can be determined by experiment. Using estimates of these low energy constants Gasser and Leutwyler[9] determines $a^0_0 = 0.20$ and $a^2_0 = -0.042$.

2.2.3 Nambu and Jona-Lasinio: Analogy with Superconductivity

The Nambu–Jona-Lasinio[31] model (NJL) is based on an analogy with superconductivity model on Bardeen, Cooper, Schriffer[32] (BCS). In the NJL model, it is assumed that there are bare fermion fields, left handed and right handed, which form a quasiparticle fermion in analogy to the BCS condensate formed of negative charge electrons and positive charged holes. This quasiparticle was interpreted as the nulceon in [31], but a modern interpretation associates these quasiparticles with quark degrees of freedom. Also, the refinements of the BCS theory predict collective excitations of the quasiparticle pairs which leads to a pseudoscalar particle in the NJL model[12]. This is, of course, the pion field.

The scattering lengths have been determined in both SU(2)[12] and SU(3)[13]. The main thrust of the SU(2) calculation was determining the effect that non-zero energy densities have on various parameters. This is done by introducing a low energy cutoff in addition to the high energy cutoff common to NJL models. The $\pi\pi$ scattering amplitude has three terms: a) the first order Born (or box) diagram, b) scalar-isoscalar (σ) exchange, and c) vector-isovector (ρ) exchange. These terms are written in terms of integrals over the applicable energy region. For the vacuum case, that is low energy cutoff is zero, yields the scattering lengths $a_0^0 = 0.22$ and $a_0^2 = -0.074$. The SU(3) calculation is very similar except that the medium effects are not considered (no lower energy cutoff) but contributions from strange quarks are

added. The resulting scattering lengths are $a_0^0 = 0.26$ and $a_0^2 = -0.062$.

2.3 $K_{\pi 3}$ Decay and $K\pi \to \pi\pi$ Scattering

The decay $K \to \pi\pi\pi$ can be related to $K\pi \to \pi\pi$ scattering using well known crossing relations. The accomplishment of Sawyer and Wali[2] was to carry this one step further to find a correspondence between the decay amplitude and $\pi\pi$ scattering amplitude. The result for $K^+ \to \pi^+\pi^+\pi^-$ (or τ) decay was fully derived by Sawyer and Wali. Their formulation also works for $K^+ \to \pi^+\pi^0\pi^0$ (or τ'), the decay channel we measure, but the final result was not stated. A detailed description, highlighting the $K^+ \to \pi^+\pi^0\pi^0$ channel, is given below. In this section τ (and τ') refer to the archaic notation of the CP-odd eigenstate of the kaon.

The starting point, similar to Chew and Mandelstam[3], is a once subtracted dispersion relation.

$$A^{\tau'}(s_1, s_2, s_3) = \lambda' + \frac{s_3 - s_0}{\pi} \int ds' \frac{\rho'(s')}{(s' - s_3)(s' - s_0)} + \frac{s_2 - s_0}{\pi} \int ds' \frac{\sigma'(s')}{(s' - s_2)(s' - s_0)} + \frac{s_1 - s_0}{\pi} \int ds' \frac{\sigma'(s')}{(s' - s_1)(s' - s_0)} \tag{2.22}$$

The center of mass energies are denoted $s_{1,2}$ for the $\pi^+\pi^0$ systems and s_3 for the $\pi^0\pi^0$ system. These energies are constrained to be $s_1 + s_2 + s_3 = M_K^2 + 3m_\pi^2 = 3s_0$ which also defines s_0. The spectral functions are denoted as ρ' and σ' and the $K\pi \to \pi\pi$ coupling constant is denoted λ'. A similar equation also holds for τ decay with spectral functions ρ and σ and coupling constant λ. States of definite angular momentum are projected out using (2.6). However the isospin projections are slightly different as

discussed below.

There are two important points to keep in mind in the following discussion. Firstly, the physical region for $K\pi$ scattering is $s_3 > (M_K + m_\pi)^2 \gtrsim 16m_\pi^2$. However, we are interested in $K_{\pi 3}$ decay which corresponds to an unphysical region ($4m_\pi^2 < s_3 \lesssim 16m_\pi^2$) in the scattering analysis. Although this requires careful consideration, as asserted in reference [2] the scattering results are not changed. Secondly, although this analysis concentrates on the τ' decay channel, charge exchange in $\pi\pi$ scattering causes τ decay to contribute to scattering in τ' at the same level.

Two important relations are necessary to proceed. The first relates the spectral functions to the imaginary part of the amplitude.

$$\Im\ A(q^2) = [4(q^2 + m_\pi^2)]\alpha \tag{2.23}$$

where α represents one of the spectral functions. The second relation is analogous to the unitarity condition (2.7) in $\pi\pi$ scattering.

$$\Im\ A(K\pi_a, \pi_b\pi_c) = \frac{q}{\sqrt{q^2 + m_\pi^2}} \sum A(K\pi_a, 2\pi) t(2\pi, \pi_b\pi_c) \tag{2.24}$$

where t represents pion scattering amplitudes. The sum in this equation is over intermediate states and isospin. There are 4 amplitudes that can be considered, which are shown in Table 2.2. Also shown is the associated spectral function used in eqn. 2.23.

Combining equations (2.23) and (2.24) yields the following relations for the four spectral functions.

Table 2.2: Scattering amplitudes and the corresponding spectral function

Amplitude	Spectral Function
$A_1(K^+\pi^+, \pi^+\pi^+)$	ρ
$A_2(K^+\pi^-, \pi^+\pi^-)$	σ
$A_3(K^+\pi^-, \pi^0\pi^0)$	ρ'
$A_4(K^+\pi^0, \pi^+\pi^0)$	σ'

$$\frac{4(q^2+m_\pi^2)^{\frac{3}{2}}}{q}\rho = A_1 t_0^{2\dagger} \tag{2.25a}$$

$$\frac{4(q^2+m_\pi^2)^{\frac{3}{2}}}{q}\sigma = A_2(\frac{1}{3}t_0^{2\dagger} + \frac{2}{3}t_0^{0\dagger}) + A_3(-\frac{1}{3}t_0^{2\dagger} + \frac{1}{3}t_0^{0\dagger}) \tag{2.25b}$$

$$\frac{4(q^2+m_\pi^2)^{\frac{3}{2}}}{q}\rho' = A_2(-\frac{2}{3}t_0^{2\dagger} + \frac{2}{3}t_0^{0\dagger}) + A_3(\frac{2}{3}t_0^{2\dagger} + \frac{1}{3}t_0^{0\dagger}) \tag{2.25c}$$

$$\frac{4(q^2+m_\pi^2)^{\frac{3}{2}}}{q}\sigma' = A_4 t_0^{2\dagger} \tag{2.25d}$$

Recognizing that for the scattering process, only one of the integrals in (2.22) is in the physical region and the other two are in the unphysical region yields the integral equations for the amplitudes

$$A_1(\nu) = \lambda + R(\rho,\nu) + \overline{L}(2\sigma,\nu) \tag{2.26a}$$

$$A_2(\nu) = \lambda + R(\sigma,\nu) + \overline{L}(\rho+\sigma,\nu) \tag{2.26b}$$

$$A_3(\nu) = \lambda' + R(\rho',\nu) + \overline{L}(2\sigma',\nu) \tag{2.26c}$$

$$A_4(\nu) = \lambda' + R(\sigma',\nu) + \overline{L}(\rho'+\sigma',\nu) \tag{2.26d}$$

again introducing the dimensionless parameter $\nu = \frac{s}{4m_\pi^2} - 1$. The integrals $R(x,\nu)$ and $\overline{L}(x,\nu)$ are right hand and left hand integrals respectively. Note that opposite to the $\pi\pi$ scattering case that the right hand integral is "physical" and left hand cut is "unphysical" This set of four equations is reduced to two independent equations

by imposing the $\Delta I = \frac{1}{2}$ rule. The above amplitudes are related by $A_1 = 2A_4$ and $A_2 = A_3 + A_4$ with coupling constant $\lambda' = \frac{\lambda}{2}$. Including $\Delta I = \frac{3}{2}$ transitions does not modify these relations. Next, the remaining amplitudes are then combined to form states of definite isospin: $B_0^0 = 3A_3 + 2A_4$ and $B_0^2 = 2A_4$ where B_L^I is the $K\pi \to \pi\pi$ scattering amplitude for isospin I and angular momentum L. Integral equations for these amplitudes follow by using equations (2.26) and (2.25).

$$B_0^0(\nu) = \frac{5}{2}\lambda + R(B_0^0 t_0^{0\dagger}, \nu) + \overline{L}(\frac{2}{3}B_0^0 t_0^{0\dagger} + \frac{10}{3}B_0^2 t_0^{2\dagger}, \nu) \tag{2.27}$$

$$B_0^2(\nu) = \lambda + R(B_0^2 t_0^{2\dagger}, \nu) + \overline{L}(\frac{2}{3}B_0^0 t_0^{0\dagger} + \frac{1}{3}B_0^2 t_0^{2\dagger}, \nu) \tag{2.28}$$

The critical observation is the similarity between these integral equations and the $\pi\pi$ scattering equations

$$t_0^0(\nu) = -5\lambda_\pi + R(t_0^{0\dagger} t_0^0; \nu) + L(\frac{2}{3}t_0^{0\dagger} t_0^0 + \frac{10}{3}t_0^{2\dagger} t_0^2; \nu) \tag{2.16}$$

$$t_0^2(\nu) = -2\lambda_\pi + R(t_0^{2\dagger} t_0^2; \nu) + L(\frac{2}{3}t_0^{0\dagger} t_0^0 + \frac{1}{3}t_0^{2\dagger} t_0^2; \nu) \tag{2.17}$$

The integrals $L(a, \nu)$ and $\overline{L}(a, \nu)$ are in principle different, however, they are approximately the same. This leads to a solution $B_0^0 = -\frac{\lambda}{2\lambda_\pi} t_0^0$ and $B_0^2 = -\frac{\lambda}{2\lambda_\pi} t_0^2$.

This solution, again using the unitarity condition (2.25), can be substituted into (2.22) to yield

$$-\frac{2\lambda_\pi}{\lambda}A^{\tau'} = -\lambda_\pi + R(\frac{1}{6}t_0^2 t_0^{2\dagger} + \frac{1}{3}t_0^0 t_0^{0\dagger}, \nu_1) + R(\frac{1}{6}t_0^2 t^{2\dagger} + \frac{1}{3}t_0^0 t_0^{0\dagger}, \nu_2) + R(t_0^2 t_0^{2\dagger}, \nu_3) \tag{2.29}$$

where $R(a, \nu)$ are the same integrals as (2.16) and (2.17). Thus these integrals can be replaced by the subtraction constant, the scattering amplitude and the left handed integrals. The decay amplitude is written as

$$-\frac{2\lambda_\pi}{\lambda}A^{\tau'} = 2\lambda_\pi + \frac{1}{2}[t_0^2(s_1) + t_0^2(s_2)] + \frac{1}{3}[t_0^0(s_3) - t_0^2(s_3)] \qquad (2.30)$$
$$+\frac{1}{3}[E^0(s_1) + E^0(s_2)] + \frac{1}{6}[E^2(s_1) + E^2(s_2)] + E^2(s_3)$$

Where $E^I(s)$ are integrals over $t_0^I t_0^{I\dagger}$. See [2] for details.

Two approximations can be made. Since stopped $K_{\pi 3}$ decay produces pions only near threshold, the threshold approximation

$$\delta_0^I(q) \approx a_0^I q \qquad (2.31)$$

and since both a_0^I and q are small $\sin\delta \approx \delta$ can also be used. Furthermore, under these conditions, the integrals $E^I(s)$ are both small and gradually varying and thus can be neglected. Thus the matrix element is finally written as

$$A^{\tau'} = -\frac{\lambda}{2\lambda_\pi}\left\{2\lambda_\pi + \frac{a_0^0}{6}[\sqrt{s_3}] \right. \qquad (2.32)$$
$$\left. +\frac{a_0^2}{2}\left[\frac{\sqrt{s_1}+\sqrt{s_2}}{2} - \frac{\sqrt{s_3}}{3}\right] + \cdots\right\}$$

Chapter 3

Experiment E246

The goal of E246 is to measure the time reversal (T) violating transverse muon polarization (P_T) in stopped $K^{+} \rightarrow \mu^{+}\pi^{0}\nu$ decay (BR=3.2%). The interest in this decay channel comes from the observation of CP violation in K^{0} decay, which implies T violation, and Sakurai's observation[33] that the muon polarization transverse to the decay plane is T odd and thus zero by T-invariance. Therefore a measurement of non-zero P_T would be a clear indication of T-violation.

This experiment is performed at the High Energy Accelerator Research Organization (KEK) in Japan. The 12 GeV proton beam from the Proton Synchrotron is used to produce secondary beams of kaons. The accelerator was run in two different modes during the experiment. The short-pulse mode uses a 0.5 s pulse with a repetition rate of 2.6 s and long-pulse mode uses a 2.0 s pulse with repetition rate of 4.0 s. In each case there are usually 3.0 to 4.0 $\times$ 10^{12} protons per pulse. The experiment uses the K5 beam line (see Fig. 3.1) which yields a 660 MeV/c kaon beam with a momentum bite

Table 3.1: Summary of kaon decay channels

Channel	Branching Ratio (%)
$\pi^+\pi^0$	21.17
$\mu^+\nu$	63.51
$e^+\nu$	1.55
$\pi^+\pi^+\pi^-$	5.59
$\pi^+\pi^0\pi^0$	1.73
$\pi^0\mu^+\nu$	3.18
$\pi^0 e^+\nu$	4.82

of $\pm 3\%$ and on the order of 10^4 kaons per spill. Figure 3.2 shows both the side and end views of the detector setup. A Fitch type differential Čerenkov counter is used to reject the large pion beam background ($\pi/K \approx 6$). After being slowed down in a BeO degrader, the kaons are stopped in the active target before decaying. Table 3.1 shows some of the available decay channels. The charged particles are tracked in the target, by the ring counters (scintillating rings) and C1 (drift chamber) surrounding the target and the C2, C3, and C4 chambers (multi-wire proportional chambers or MWPC) placed in each sector of the spectrometer.

At the exit of each sector of the spectrometer, there is a muon stopper and a pair of positron counters to measure the muon polarization. Also surrounding the target is an array of CsI(Tl) crystals to detect photons, primarily those from $\pi^0 \rightarrow 2\gamma$ decay (BR$\approx$99%).

More details of the target and photon detector are described in sections 3.1 and 3.2, respectively. Details of the rest of the setup, which were not used in the $K_{\pi 3}$ study, are given in section 3.3. The trigger used for $K_{\pi 3}$ study was $C_K * Fid^{\sim} * n\gamma$

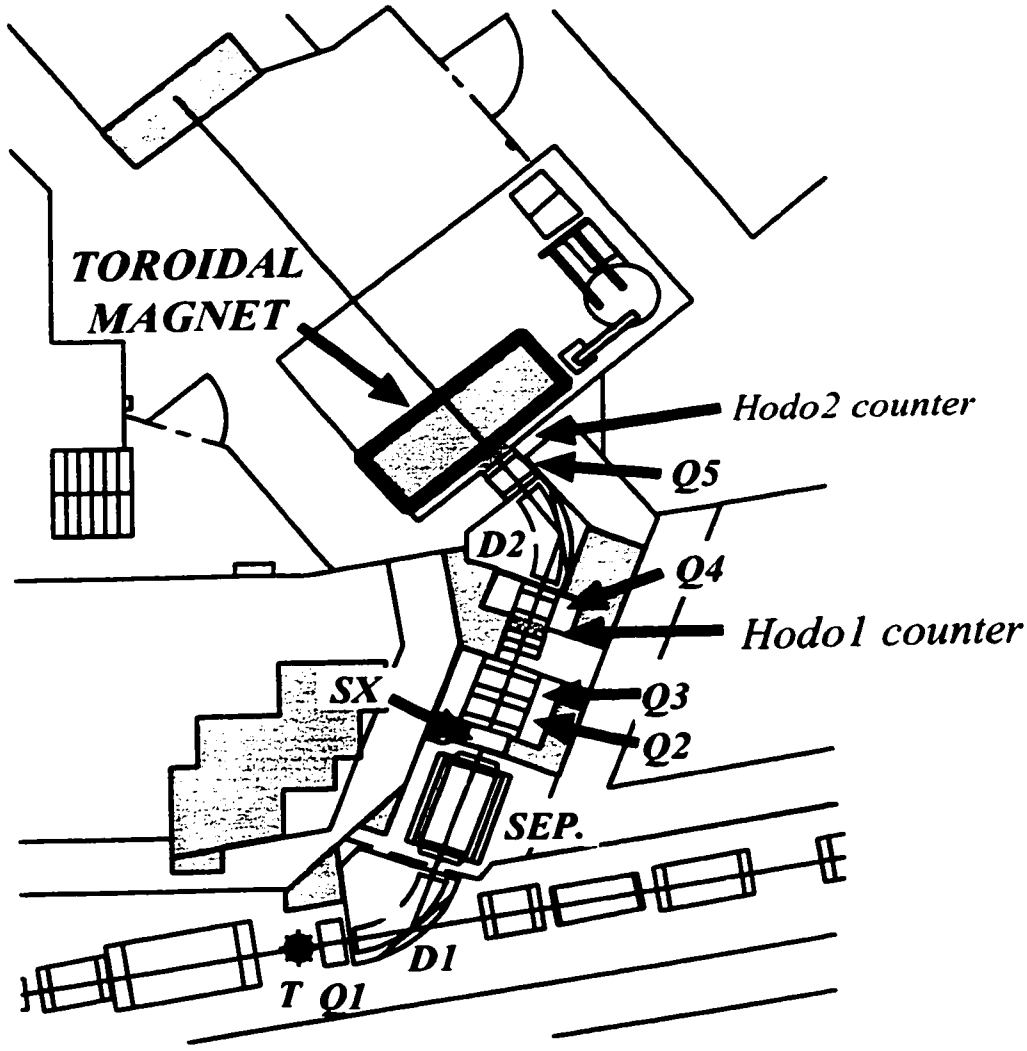

Figure 3.1: Schematic of K5 beamline

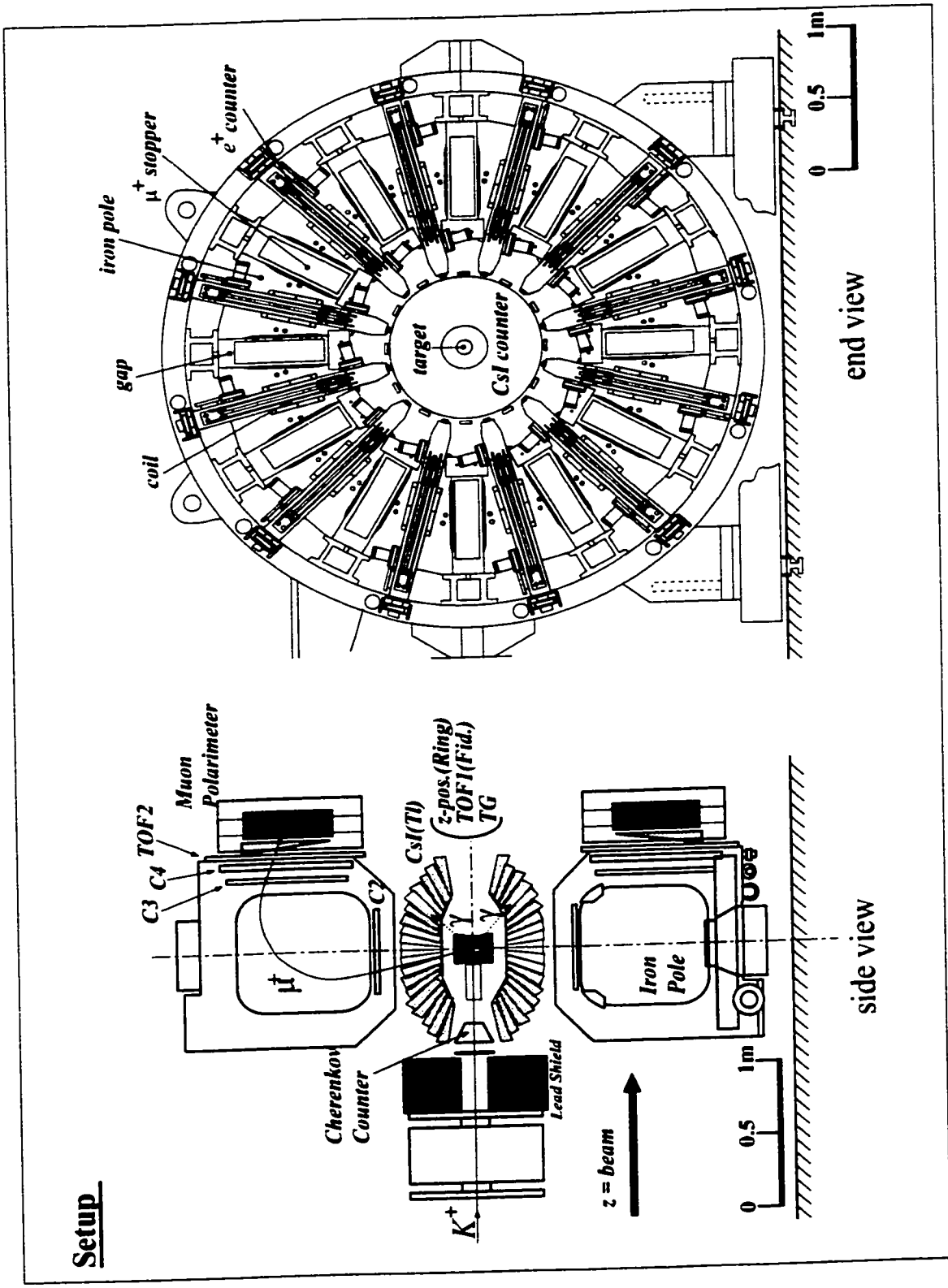

Figure 3.2: Side and end views of E246 setup

Table 3.2: Summary of runs used in the analysis. The length of data taking for each cycle is shown as well as the number of events from this cycle.

Cycle	Time (hrs)	Good Events
May. 96	4	359
Jun. 96	4	436
Oct. 96	6	580
Dec. 97	18	1834
Jun. 98	1	110

where C_K denotes the Čerenkov with K trigger, $Fid^{\sim}$ is the delayed fiducial counters (part of the active target), and $n\gamma$ requires n clusters in the CsI(Tl) crystals. This trigger condition allowed nearly all of the $K_{\pi 3}$ phase space to be probed. The data was collected over several different run cycles over about a two year period. Table 3.2 shows the cycles used, the amount of data taking for this trigger and the number of events from each cycle.

3.1 Active Target

The heart of the setup is the active target as shown in Fig. 3.3. In this figure, the squares show the numbering of the scintillating fibres. The 12 irregular shaped counters surrounding the target are the fiducial counters. The purpose of the target is to stop the kaons and to help determine the position of the kaon decay vertex. The active target consists of 256 scintillating fibres each about 5x5 mm square in cross section and 2 meters long. The fibres are coupled to Hamamatsu H3164 photomultiplier tube at the downstream end. Although active along the entire length, only

the first 20 cm are used. This region is determined by the 20 cm long fiducial counters. As mentioned above, the fiducial counters are part of the trigger, serving two purposes. The first is to help ensure that the kaon has stopped before decaying and the second is as the start pulse for all timing information (time-to-digital converter or TDC) information. Also, using additional dead material of matching refractive index, the fiducial counters give the target the same 12-fold rotational symmetry as the spectrometer.

The target analysis can only determine two of the coordinates of the decay vertex. Since the beam defines the z-axis, the target determines the (x, y) coordinates only. The third coordinate is fixed by charged particle tracking for the analysis of $K_{\mu 3}$ or by kinematics for the $K_{\pi 3}$ analysis. The latter method of our interest is described in section 4.1. The stopping fibre is determined to be the fibre with the largest energy deposit with a timing of (-10,150) ns with a minimum threshold of 5 MeV. As the start counter, the fiducial time window is set to (-10,10) ns.

3.2 CsI Calorimeter

The primary purpose of this detector is to measure photons in order to reconstruct the parent π^0's. The calorimeter consists of 768 CsI(Tl) crystals each about 13.5 radiation lengths deep. The calorimeter, as shown in Fig. 3.4, covers 75% of 4π sr. There are 12 gaps in the CsI for the passage of charged particles to the detector for momentum analysis, and 2 holes (one up stream and one down stream) serve as the

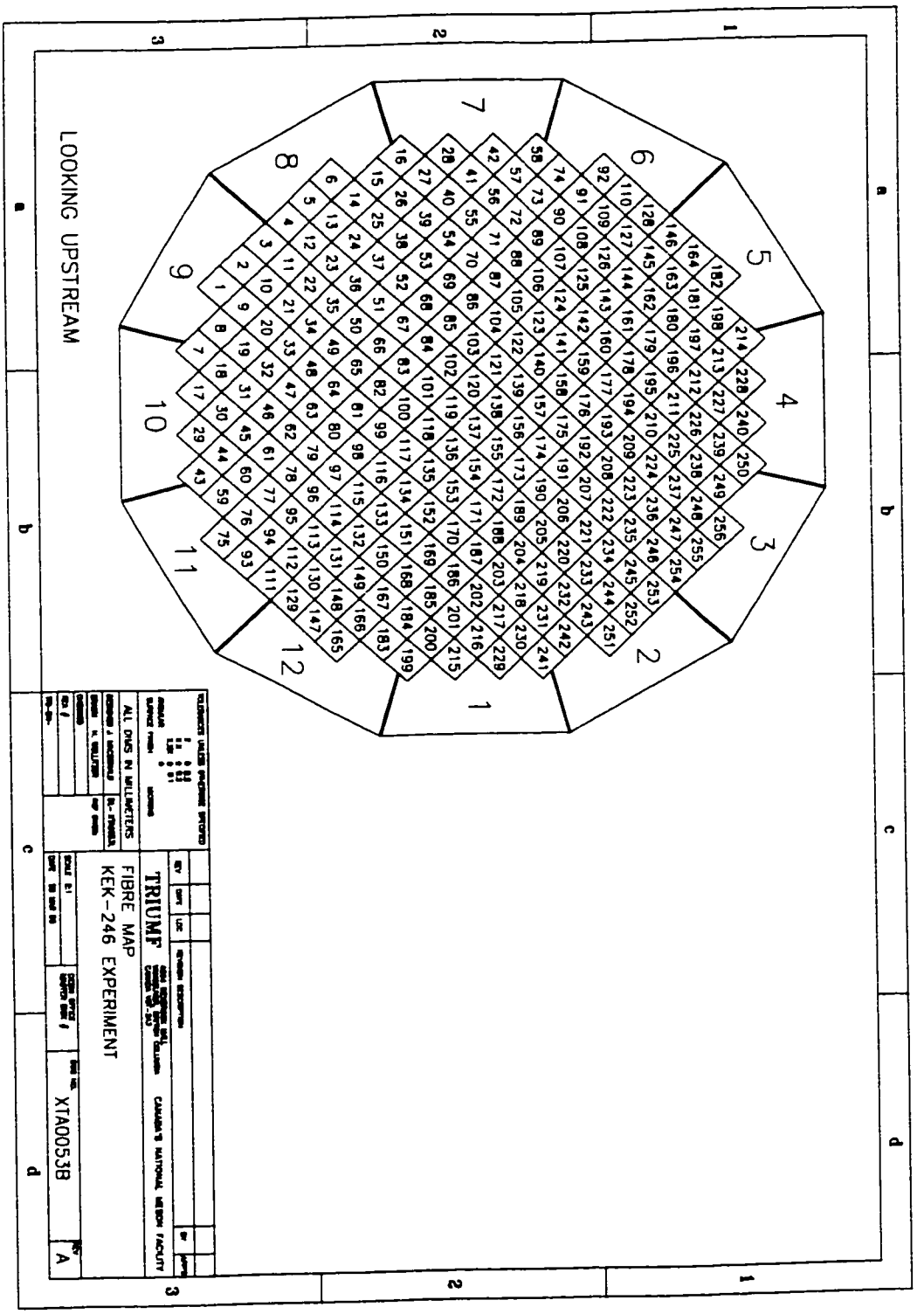

Figure 3.3: End view of target bundle and fiducial counters. The numbers 1-256 in the middle squares are the 5x5 mm scintillating fibres. The outer envelope numbered 1-12 are the fiducial counters.

entrance and exit of beam particles. The segmentation allows the measurement of photon position in addition to the energy. Once the kaon decay vertex is known, the four momentum of the photons and hence π^0 is completely determined.

Because of the properties of electromagnetic showers, several neighbouring crystals fire from a single photon. A flexible clustering algorithm, developed by C. Mindas[34], is used to reconstruct the photon. The start of a cluster is a crystal with more than 10 MeV within a time window (-30,30) ns. The eight neighbours of this crystal are then added to the cluster. If any of these surrounding crystals has an energy deposit of more than 0.75 MeV the neighbours of that crystal are also added. The algorithm ensures that crystals are not double counted in the cluster. This progresses up to a maximum crystal size of 5×5 cluster. The energy of the photon is simply the energy sum of the crystals and the hit position is an energy weighted average of the crystal position. In order to reject accidental photons, various backgrounds, and electronic noise, clusters with less than 20 MeV total energy are disregarded.

3.3 Charged Particle Tracking and Polarimeter

3.3.1 Charged Particle Tracking

Surrounding the target are the ring counters and the C1 chamber. Each of the 32 ring counters are scintillating rings about 6 mm wide and 10 mm thick encasing the target. Outside of this is the C1 chamber which is a drift chamber with both anode and cathode readouts. The function of both of these detectors is to provide

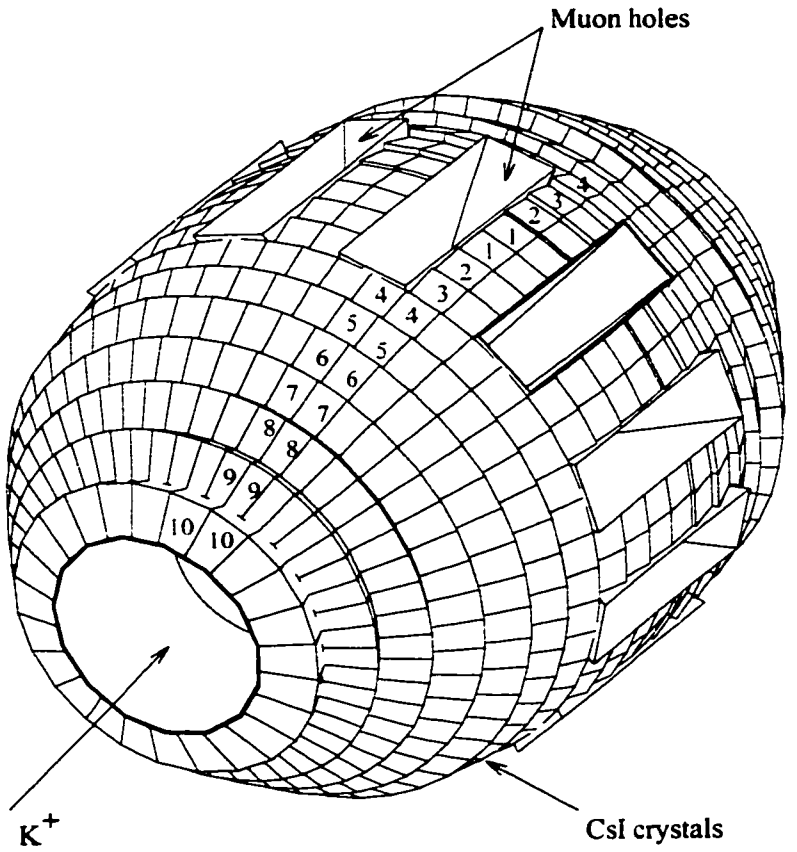

Figure 3.4: Schematic of CsI barrel

information on the exit point of the charged particle from the target. The toroidal superconducting spectrometer has 12 fold rotational symmetry. Precision machining and a single power source ensure the magnetic fields in each gap are identical. A set of three MWPC (C2, C3, and C4) are used for each magnet gap, one at the entrance and two at the exit. This yields the momentum of the charged particle and through extrapolating to the target, the kaon decay vertex. After these chambers a scintillator counter with double ended readout is used to determine the time of flight and therefore identifying the charged particle.

3.3.2 Polarimeter

This detector is designed to measure the average muon polarization. The muon is stopped in a series of Al plates in the fringing field of the magnet. This magnetic field preserves the muon polarization as it is stopped. The muon then decays $\mu^+ \rightarrow e^+\nu\overline{\nu}$ (BR$\approx$100%) with a lifetime of 2.2μs. By selecting decays where the π^0 direction is along beam axis, P_T is parallel to the magnetic field and pointing in the direction of either of the positrons counters sourrounding the muon stopper. Since the distribution of decay positrons is skewed in the direction of polarization, a non-zero P_T appears as an asymmetrical counting rate in the two counters. Since each positron counter does double duty (CW counter for one gap and CCW counter for neighbouring gap) a sum over the 12 gaps, in addition to forward vs. backward going pions ratio, cancels many spurious sources of asymmetrical counting rate. Such sources include detector misalignment and non-uniformity in stopping distribution and detection efficiency.

Chapter 4

Event Selection

The data analysis relies on the fact that we can identify the two π^0s and measure their four momentum for the $K_{\pi 3}$ decays. The π^+ can be treated as missing particles. whose kinematics can be determined using the four momentum of the π^0s.

The first step of the analysis was to select candidate $K^+ \rightarrow \pi^+\pi^0\pi^0$ events for reconstruction. The preliminary data selection required a single fiducial hit (or two neighbouring hits), the stopping fibre is found (see section 3.1) and four or more photon clusters in the CsI. The selection criteria of the detectors is shown in Table 4.1.

Additional clusters are allowed due to accidentals and the small probability that the π^+ from $K_{\pi 3}$ decay reaching the CsI. The reconstruction algorithm described in this chapter followed identically for each possible 4 photon subset. With the majority of these events, only one combination passes the above analysis. In some cases (for example two photons have the same energies) a second combination also passes. In these cases the combination with the lowest Q value, as defined above, is selected.

Table 4.1: Selection criteria for detectors

Detector	Timing (ns)	Energy (MeV)
Target	(-10,150)	5
Fiducial	(-10,10)	n/a
CsI(Tl)	(-30,30)	20

Note specifically that a selected event may not have the smallest $\Delta\theta$.

The next step is to determine the z coordinate of the decay vertex, which also checks that the missing energy and momentum are consistent with a missing π^+. This selection algorithm is described in section 4.1. After passing the above reconstruction, each of the four photons must be associated with one of the two parent π^0's. This aspect is discussed in section 4.2.

4.1 Vertex Determination

Since the $K_{\pi 3}$ event with 4 photons is kinematically complete, this can be used to determine the z coordinate of the decay vertex. The reconstruction starts with simple momentum and energy conservation laws.

$$\vec{p}_{\pi^+} + \sum_{i=1}^{4} \vec{p}_{\gamma_i} = \vec{p}_K = 0 \tag{4.1}$$

$$E_{\pi^+} + \sum_{i=1}^{4} E_{\gamma_i} = E_K = M_K \tag{4.2}$$

where $\vec{p}$ and E are the momentum and energy of the subscripted particle. At this stage of the reconstruction, determining the separate π^0 four momenta is not relevant.

Equation (4.2) can be used to define the missing energy, E_{miss}, and momentum,

p_{miss}.

$$E_{miss} = M_K - \sum E_\gamma \tag{4.3}$$

$$p_{miss} = \sqrt{E_{miss}^2 - M_{\pi^+}^2} \tag{4.4}$$

This definition of missing momentum is independent of the decay vertex, although it assumes that the missing particle is a charged pion. Another definition of missing momentum is simply

$$\vec{p}_{\gamma miss} = -\sum \vec{p}_\gamma \tag{4.5}$$

which relies on knowing the decay vertex but is independent of the nature of the missing particle or particles. The principle of the algorithm is to find a z such that both definitions of missing momentum are equivalent.

In the standard way, a momentum vector can be decomposed (using spherical coordinates)

$$p_x = |\vec{p}| \cos\phi \sin\theta \tag{4.6a}$$

$$p_y = |\vec{p}| \sin\phi \sin\theta \tag{4.6b}$$

$$p_z = |\vec{p}| \cos\theta \tag{4.6c}$$

$$p_\perp = |\vec{p}| \sin\theta \tag{4.6d}$$

where the z axis defined as the beam axis, θ is the angle between $\vec{p}$ and the z axis, and ϕ is the angle in the $x - y$ plane. Starting with a test value of z_{target}, which denotes the z coordinate of the decay vertex, we can determine the momentum of each photon, for example:

$$p_{\gamma,z} = E_\gamma \frac{z_{CsI} - z_{target}}{r_{CsI,target}} \tag{4.7}$$

where z_{CsI} is the z coordinate at the calorimeter and $r_{CsI,target}$ is the total distance from the decay vertex to the calorimeter. Once the momentum of each photon is determined, it is trivial to find the missing momentum using equation (4.5). Inverting equation 4.6, the angle θ can be determined.

$$\theta_\perp = \arcsin \frac{p_{\gamma miss,\perp}}{p_{miss}} \tag{4.8}$$

$$\theta_{||} = \arccos \frac{p_{\gamma miss,z}}{p_{miss}} \tag{4.9}$$

$$\tag{4.10}$$

where the denominator is the p_{miss} defined in equation (4.4). These two angles will agree only for z coordinate equal to the decay vertex for $K_{\pi 3}$ decay, or equivalently

$$\Delta\theta = \theta_\perp - \theta_{||} \tag{4.11}$$

should be zero.

As discussed in section 3.1, the trigger region is 20 cm long, which is given by $-10 < z < 10$ cm in our coordinate system. A subset of this is determined on an event by event basis on the criterion that at each end point at least one of $p_{\gamma miss,z}$ or $p_{\gamma miss,\perp}$ is less than p_{miss}. This is a simple geometrical requirement, namely the components of a vector cannot be larger than vector itself, allowing for finite resolution. The end points of this region are found by starting at $z = \pm 10$ cm and scanning in 0.5 cm steps until a point satisfying this criteria is found. The next step is to find the point where $\Delta\theta = 0$ by the method of bisection. The bisection is terminated when the

interval over which $\Delta\theta$ changes sign is constricted to less than or equal to 1 cm. This limits the z resolution to 0.5 cm. as shown later the actual resolution is much larger.

The resulting spectrum of $\Delta\theta$ is shown in Fig 4.1. A sharp peak at $\Delta\theta = 0$ is seen along with wide flat background with the peak/background ≈ 30. This background is due to $K_{\pi 3}$ events that do not reconstruct well and background events such as $K_{\pi 2}$ and $K_{\mu 3}$. The narrow region $|\Delta\theta| \leq 0.02$ is selected for further analysis. As shown in Fig. 4.2. this selects events with a missing mass within 1 MeV of $m_{\pi^+} = 139.6$ MeV.

4.2 π^0 Identification

Now that the decay vertex is known, the next step is to find how the photons are related to the two π^0's. The four photons can be paired in three distinct ways to form π^0's, namely

$$\pi^0 \rightarrow \gamma_1\gamma_2 \ \& \ \pi^0 \rightarrow \gamma_3\gamma_4 \qquad (4.12)$$

$$\pi^0 \rightarrow \gamma_1\gamma_3 \ \& \ \pi^0 \rightarrow \gamma_2\gamma_4$$

$$\pi^0 \rightarrow \gamma_1\gamma_4 \ \& \ \pi^0 \rightarrow \gamma_2\gamma_3$$

In the analysis. a particular photon pair will not be considered if the energy sum of those two photons is less than 100 MeV. This constraint may rule out one or more of the above combinations for an event. The invariant mass of a photon pair is given by

$$M_{ab}^2 = 2E_aE_b(1 - \cos\theta_{ab}) \ (a, b = 1, 2, 3, 4) \qquad (4.13)$$

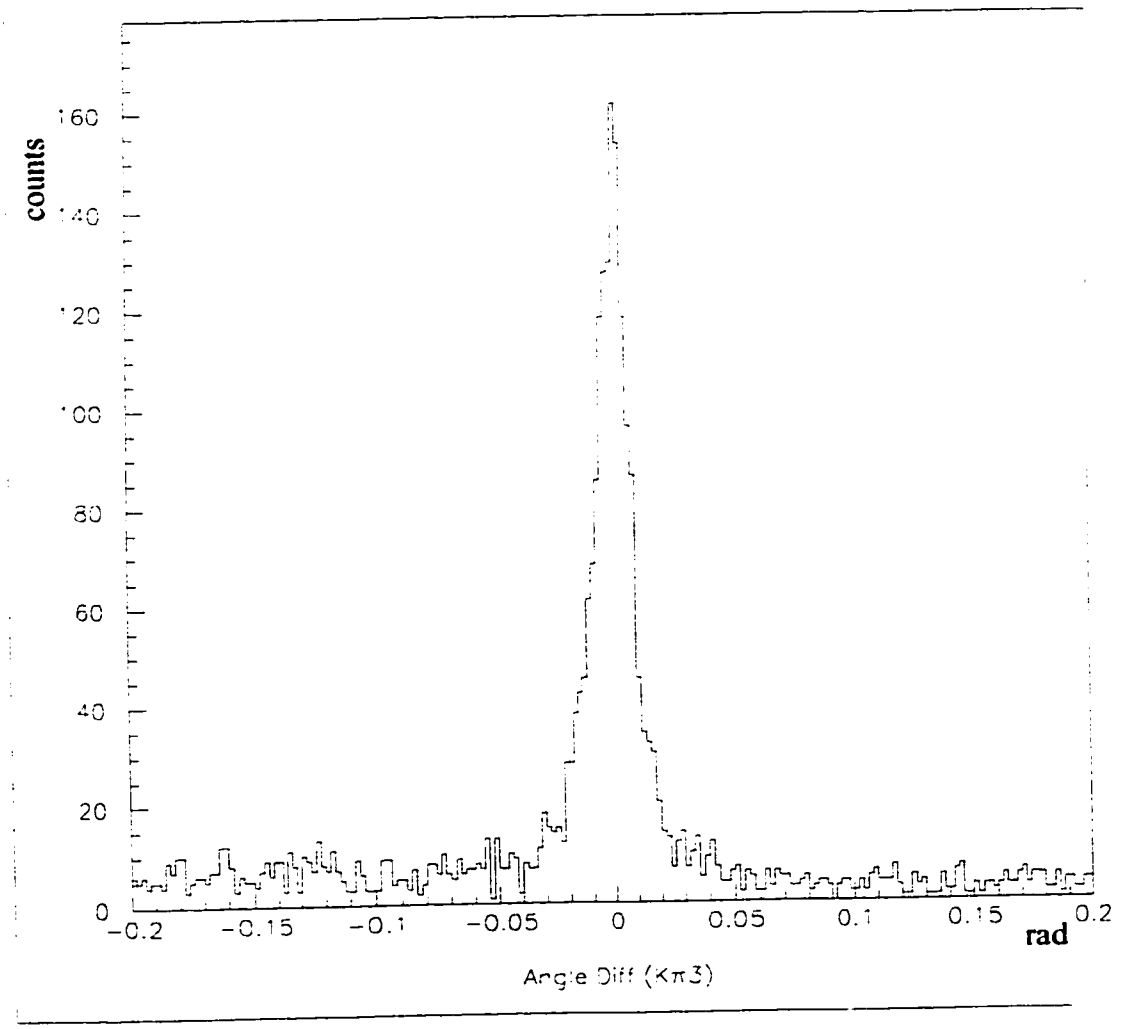

Figure 4.1: Distribution of $\Delta\theta$. A sharp peak near $\Delta\theta = 0$ is clearly evident.

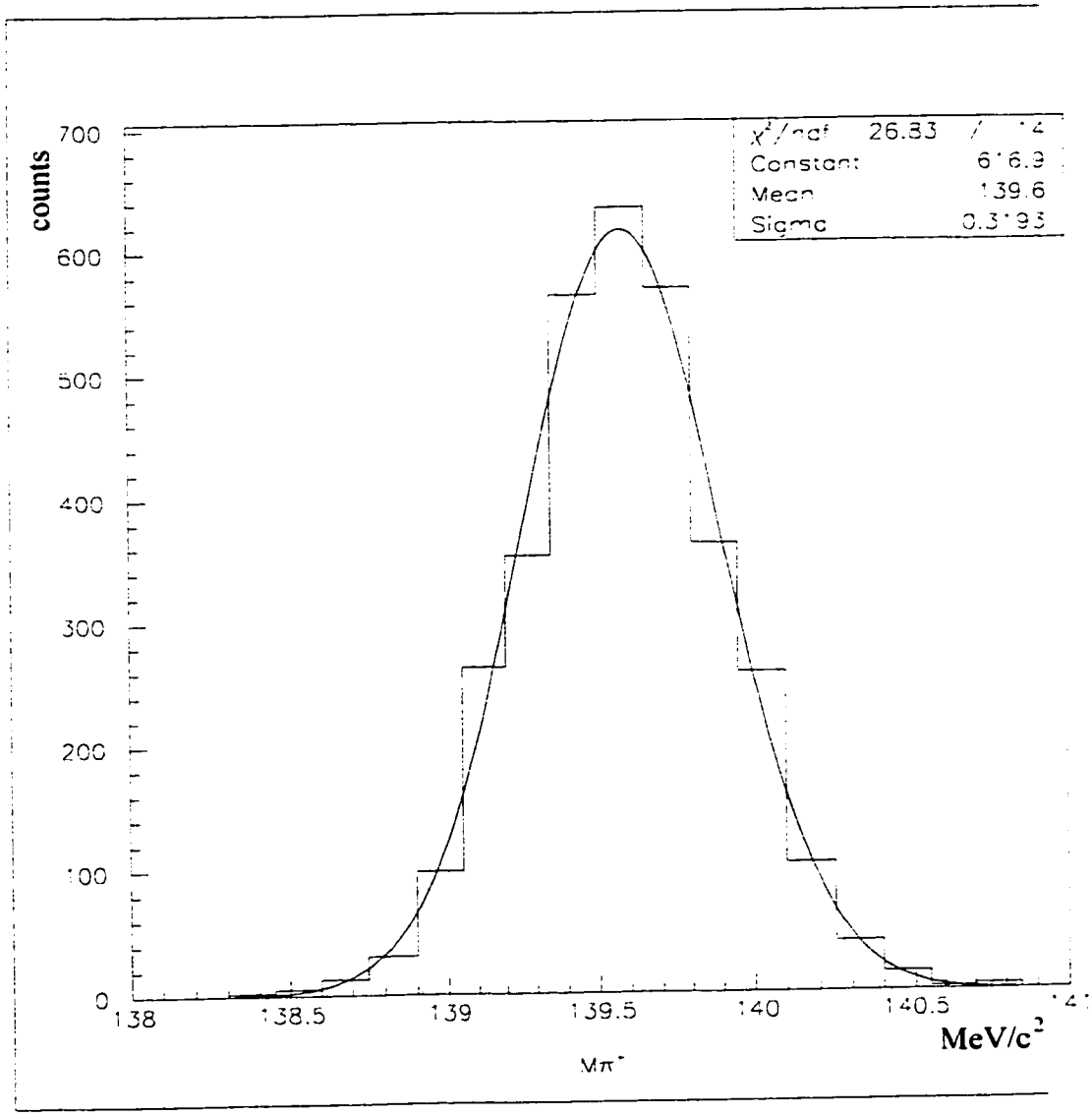

Figure 4.2: Reconstructed π^+ mass. The peak is near the expected mass $m_\pi^+ = 139.6$ MeV with very small resolution $\sigma = 0.3$ MeV.

where E is the energy of the subscripted photon and θ_{ab} is the angle between the two photons. If the pair considered is truly from π^0 decay, then this mass should be near m_{π^0} =135.0 MeV. Any other pairing should produce a random mass. Since each combination has two such pairs, a quality factor, Q, is defined.

$$Q = (M_{ab} - m_{\pi^0})^2 + (M_{cd} - m_{\pi^0})^2 \tag{4.14}$$

The combination which minimizes Q is selected as the correct pairing. Shown in Fig. 4.3 is the invariant mass distribution for the selected combination (a and b) as well as all other combinations (c and d). It is remarkable that for both the high energy and low energy π^0, a peak near the expected mass is seen yet the corresponding distributions for the wrong combinations shows no such structure. Also shown in Fig. 4.3 is the result of Monte Carlo (MC) simulations of $K_{\pi 3}$ decay using only a three body phase. The MC simulations are described in Ch. 5. The result of the MC simulation is nearly identical distribution for all four categories. This confirms that our selection criteria is correct and completes our knowledge of the kinematics for the event. The slight discrepancy that one may find in Fig. 4.3c is due to the fact the MC uses simply a three body phase space. This statement is justified in Ch. 5.

The number of events passing the above conditions are 7553 for all cycles. The background cuts discussed in Ch. 6 reduce this to 3319 good events. Table 3.2 shows the contribution from each cycle.

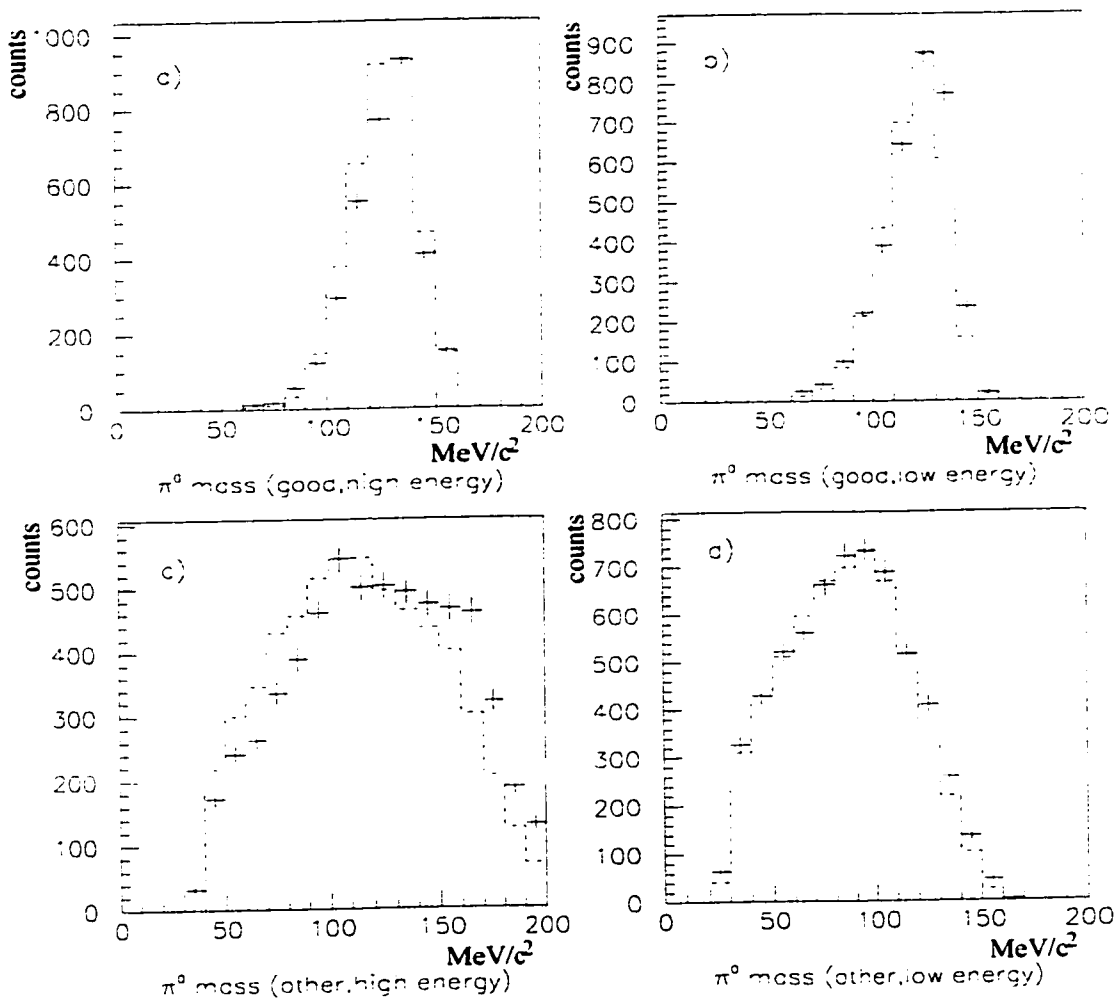

Figure 4.3: Invariant mass distributions from photon pairing. a) shows the selected pair for the higher energy of the two pairs and b) shows the lower energy selected pair. c) and d) are the same distributions for all other attempted parings. In each figure the solid crosses are data and the dotted histogram is MC simulations.

Chapter 5

Monte Carlo Simulations

The essence of the measurement is to search for s_1 and s_3 dependencies in the $K_{\pi 3}$ decay distribution caused by $\pi\pi$ final state interactions. However s_1 and s_3 dependencies also come from phase space, detector resolution, and non-uniform detection efficiencies. Monte Carlo (MC) simulations were used to isolate these effects from $\pi\pi$ scattering.

Monte Carlo simulations were done using GMC, a GEANT[1] Monte Carlo code developed for the E246 detector setup. Four different types of simulations were used. The first type simulated $K_{\pi 3}$ decay using only the three body phase space [MC(3bps)]. This was used in the analysis to extract the scattering lengths. Another three simulations were used to determine the background levels and in selecting cuts. Two of these simulated the background channels $K^+ \to \pi^+\pi^0$ (BR=21.1%) and $K^+ \to \mu^+\pi^0\nu$ (BR=3.18%). The last of these was for $K_{\pi 3}$ decay using a matrix element given by

[1]GEANT is Monte Carlo simulation package which is part of CERNLIB physics programs.

Weinberg's polynomial expansion

$$\mathfrak{M} = 1 + g\frac{s_3 - s_0}{m_\pi^2} + h\frac{(s_3 - s_0)^2}{m_\pi^4} \tag{5.1}$$

using the PDG values[35] $g = 0.594$ and $h = 0.035$. This simulation (MC(poly)) is close to what is observed and therefore gives a better estimate of background levels.

There are several features of the MC analysis which ensure that MC simulations are as close as possible to experimental data. The simulation generates the kaon at rest using a distribution coming from real data. This stopping distribution comes from data taken in Feb. 1996.

The second feature is in the simulation of the calorimeter. A resolution function derived from CsI(Tl) bench tests[36] is used to smear the energy deposits in the CsI(Tl) crystals. In addition, using hits from outside the time window, an accidental spectrum is also applied.

The third, and one of the most critical, features is the same analysis code is used for both MC generated events and data. This ensures that the MC has exactly the same reconstruction conditions and the same cuts as data thus guaranteeing that only $\pi\pi$ scattering can cause any differences between MC and data.

With any MC simulation it is important to confirm that the simulations are accurate. One method is to check the consistency between data and MC. Looking at three distributions: a) z-coordinate of the decay vertex (Fig. 5.1), b) $\Delta\theta$ distribution (Fig. 5.2) and c) the reconstructed π^+ mass (Fig. 5.3), good agreement is seen. One word of caution is necessary in our case, since the MC and data are intrinsically

different some distributions will not agree precisely. Trivially the distributions for s_1 (Fig. 5.4) and s_3 (Fig. 5.5) should, and in fact do, have different distributions. Similarly, disagreements can also occur in other distributions if there is a correlation with s_1 or s_3. One example of this are the rejected photon combination distributions shown in Fig. 4.3. Although the lower energy combination shows good agreement (Fig. 4.3d), discrepancies are seen in Fig. 4.3c. This effect is seen more dramatically in Fig. 5.6. For non-selected combinations, one sees a large shift in the invariant mass for the high energy pair between the lower s_3 ($0.067 < s_3 < 0.076$ GeV^2) and higher s_3 ($0.103 < s_3 < 0.112$ GeV^2) distributions which explains the differences. However the low energy pair shown in Fig. 5.6 has a much smaller shift and therefore almost no difference is seen. As a second check, the MC(poly) distribution used for the background study, can also be compared to data. The excellent agreement between the distributions seen in Fig. 5.7 clearly demonstrates that the differences are indeed caused by MC having only a three body phase space. It should be stressed that MC(3bps) includes trivial kinematical dependencies and thus the departures from it are evidence of extra dynamics.

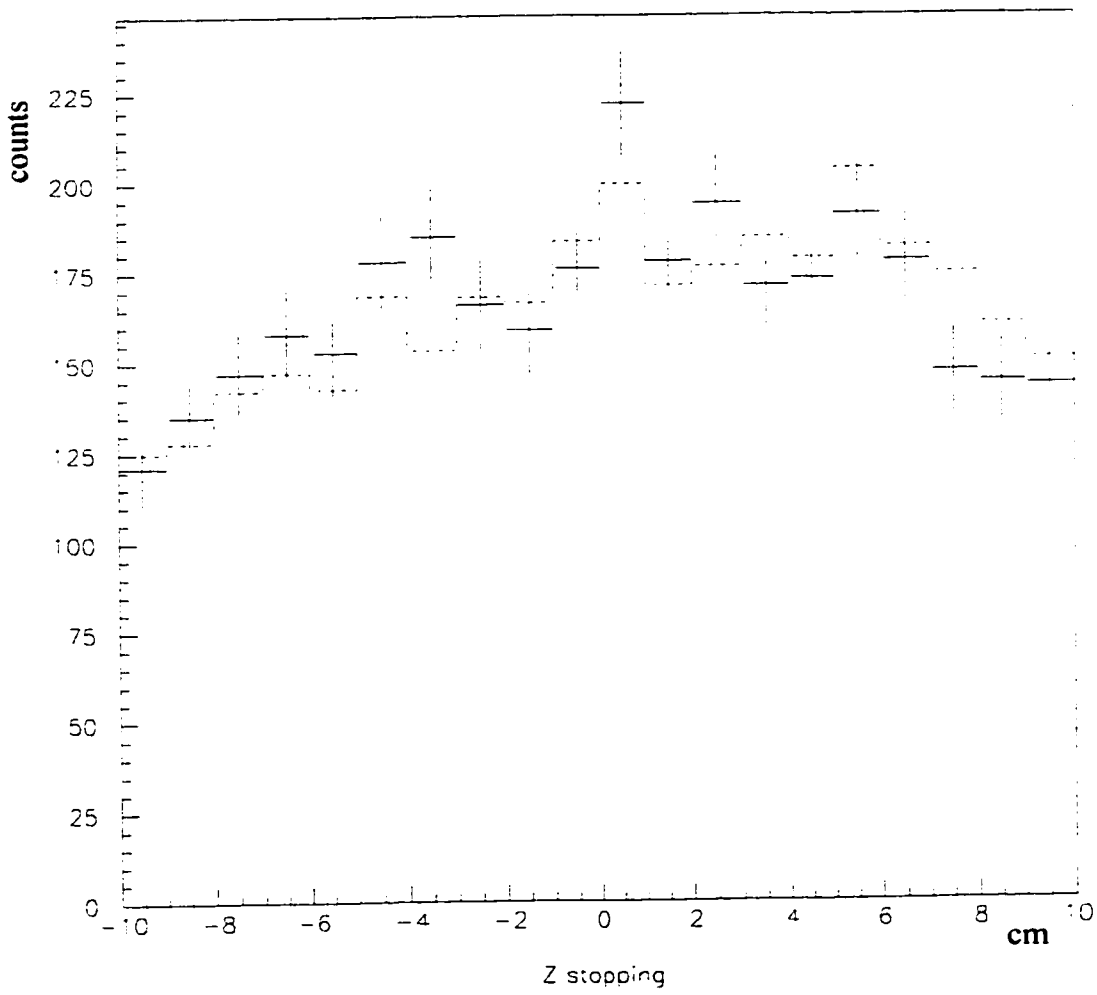

Figure 5.1: The reconstructed stopping position for data (solid cross) and MC (dotted histogram)

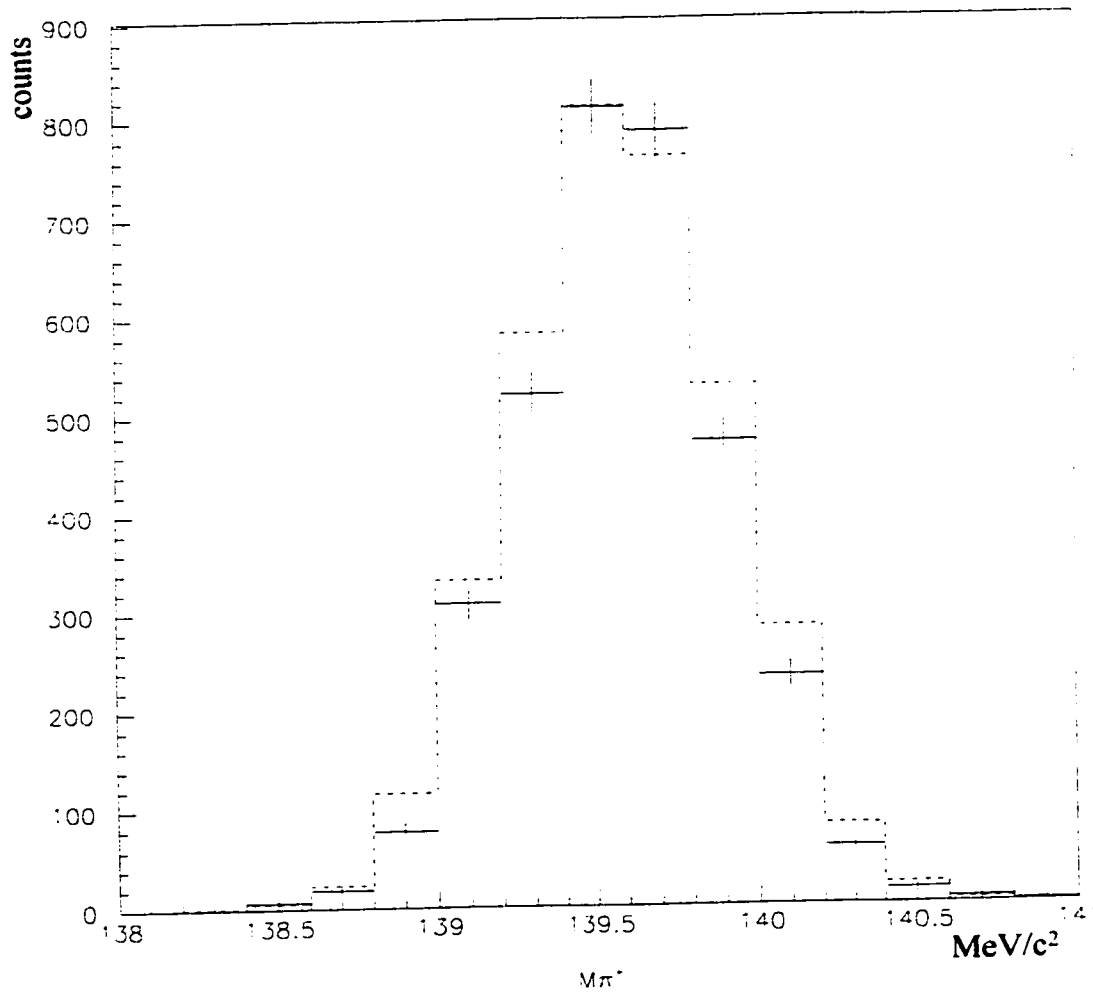

Figure 5.2: The $\Delta\theta$ distribution for data (solid cross) and MC (dotted histogram)

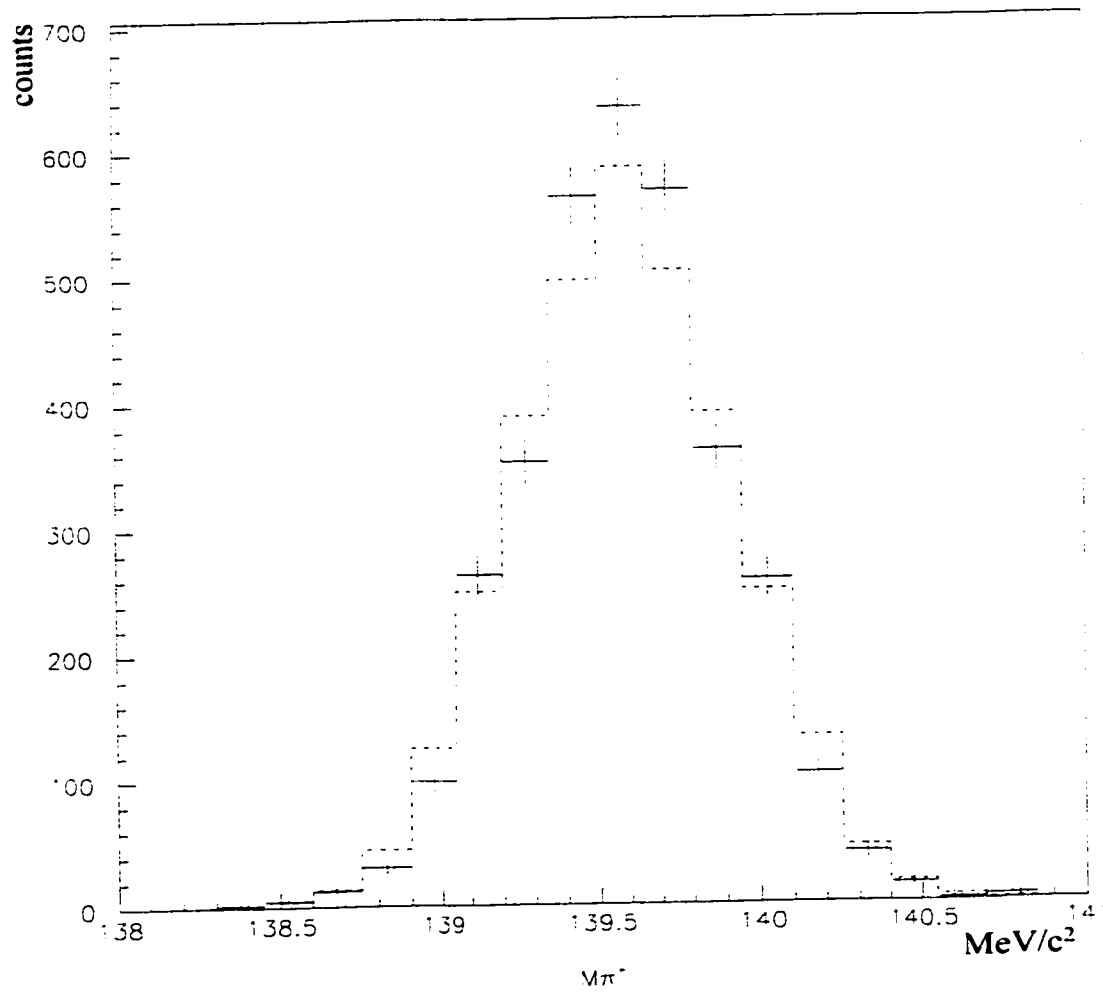

Figure 5.3: The pion mass distribution for data (solid cross) and MC (dotted histogram)

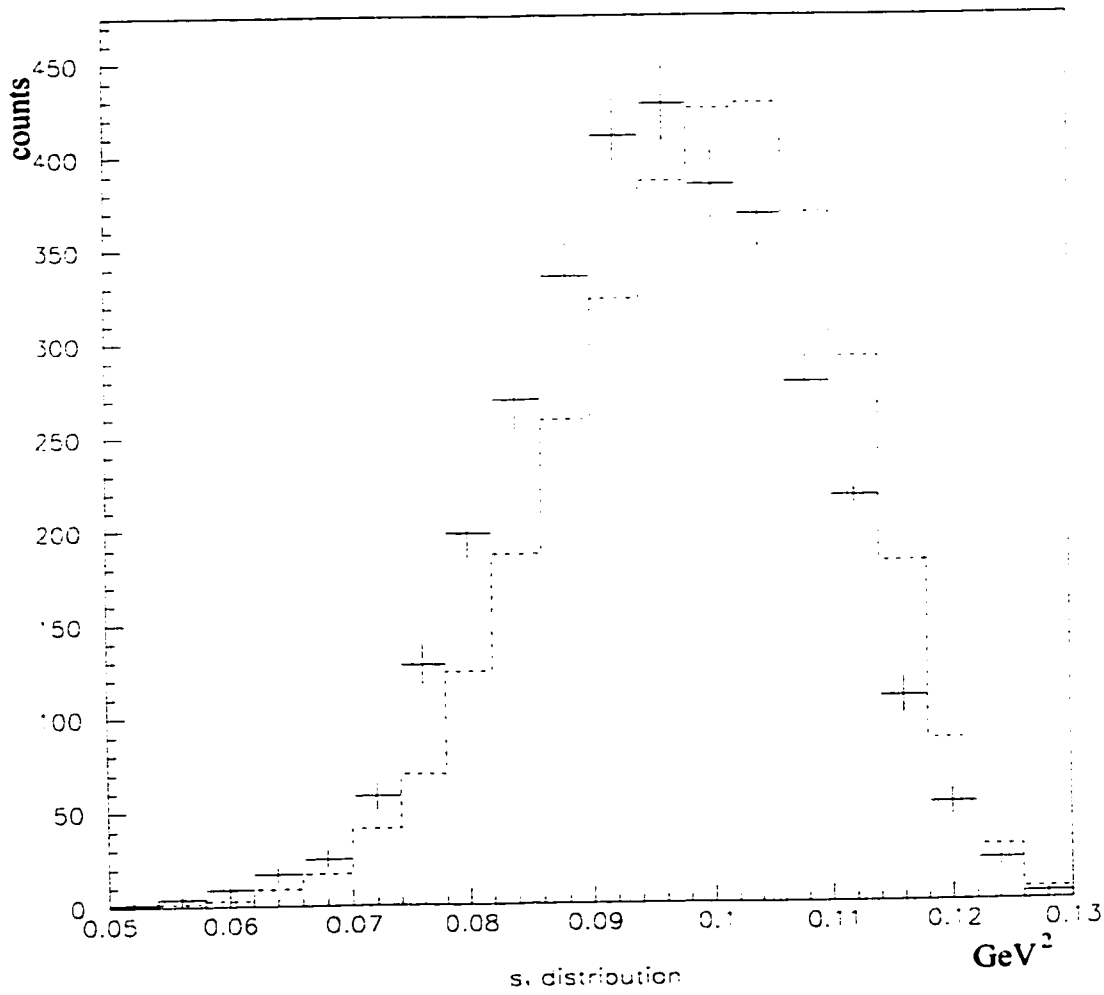

Figure 5.4: The s_1 distribution showing the difference between MC (dotted histogram and data (solid cross)

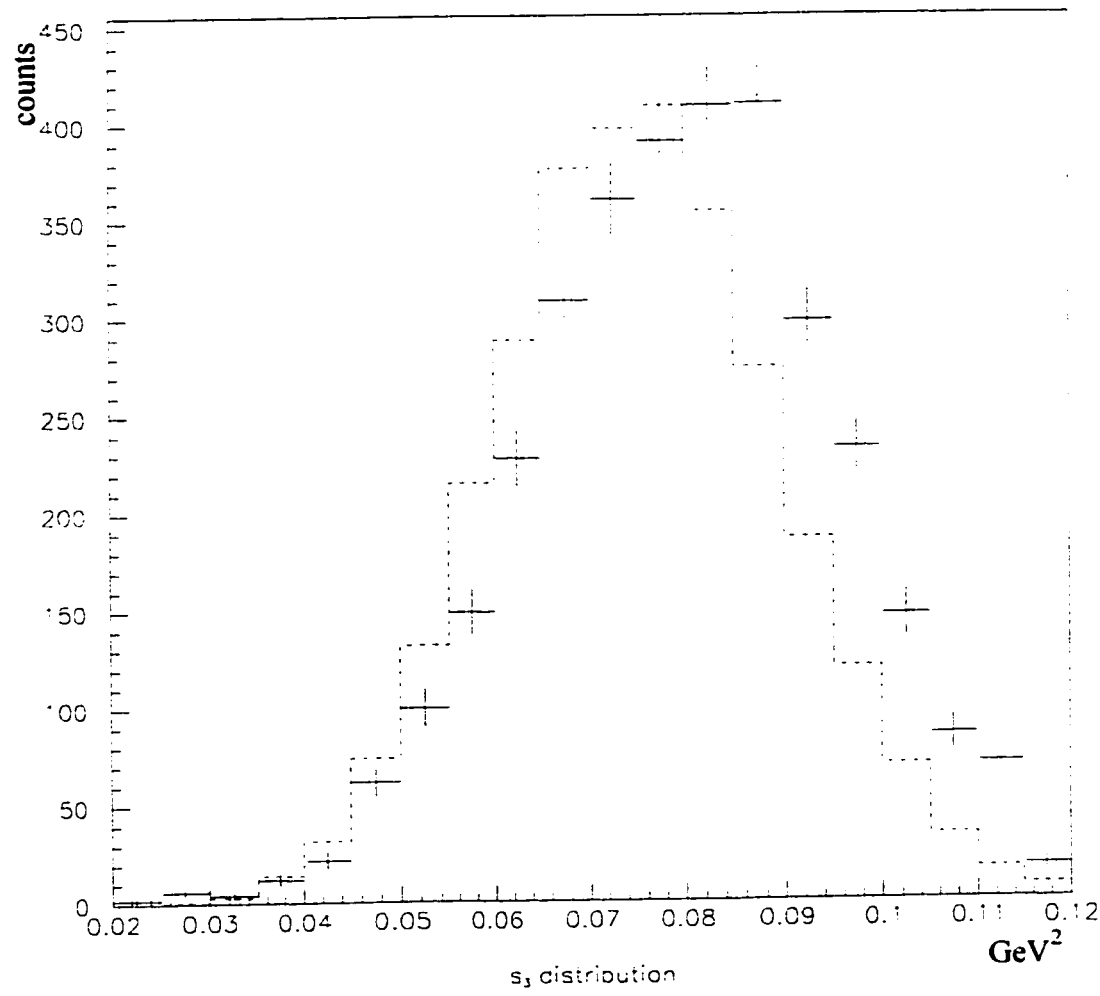

Figure 5.5: The s_3 distribution showing the difference between MC (dotted histogram) and data (solid cross)

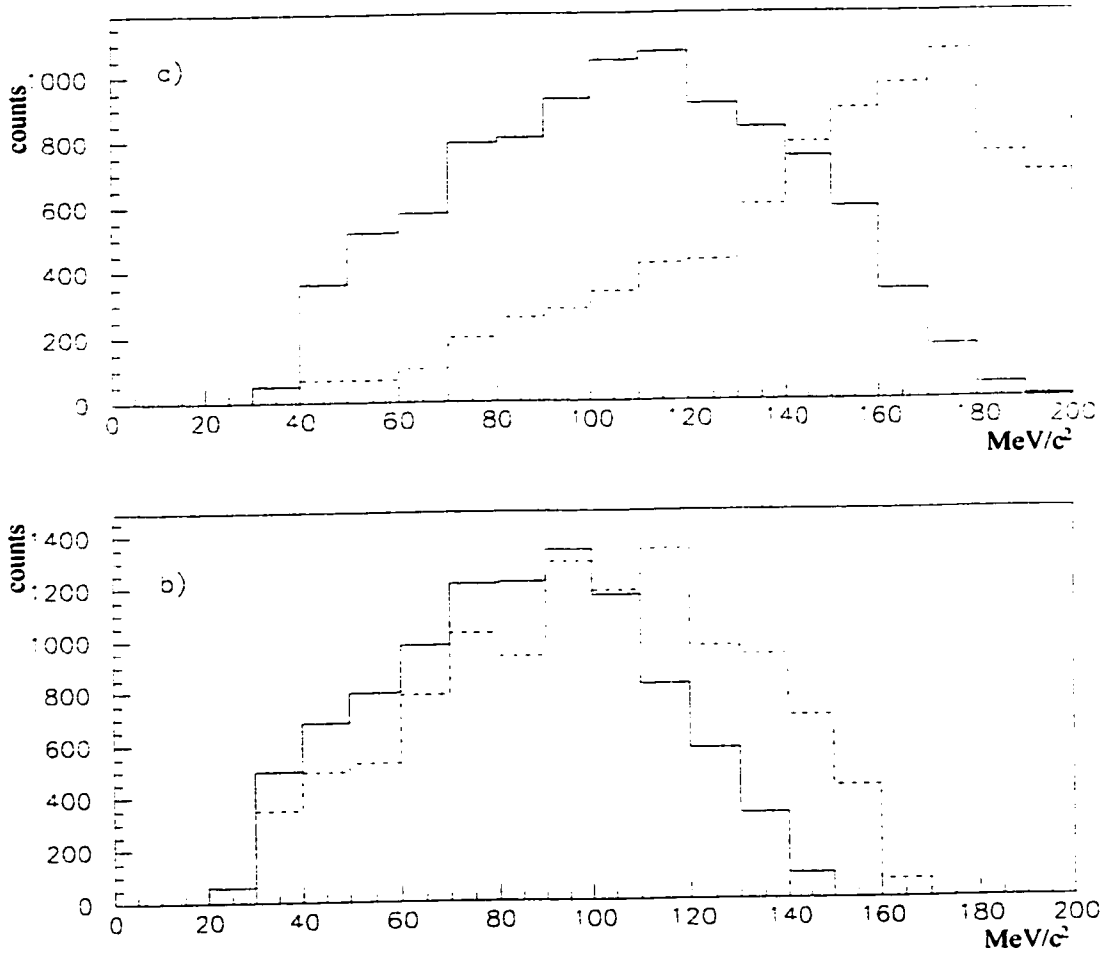

Figure 5.6: The invariant mass distributions of non selected pairings. a) higher energy pair and b) lower energy pair. Shown is the distribution in the range $0.067 < s_3 < 0.076$ (solid histogram) and $0.103 < s_3 < 0.112$ (dashed histogram). This explains why a discrepancy is seen in Fig. 4.3c but not in Fig. 4.3d.

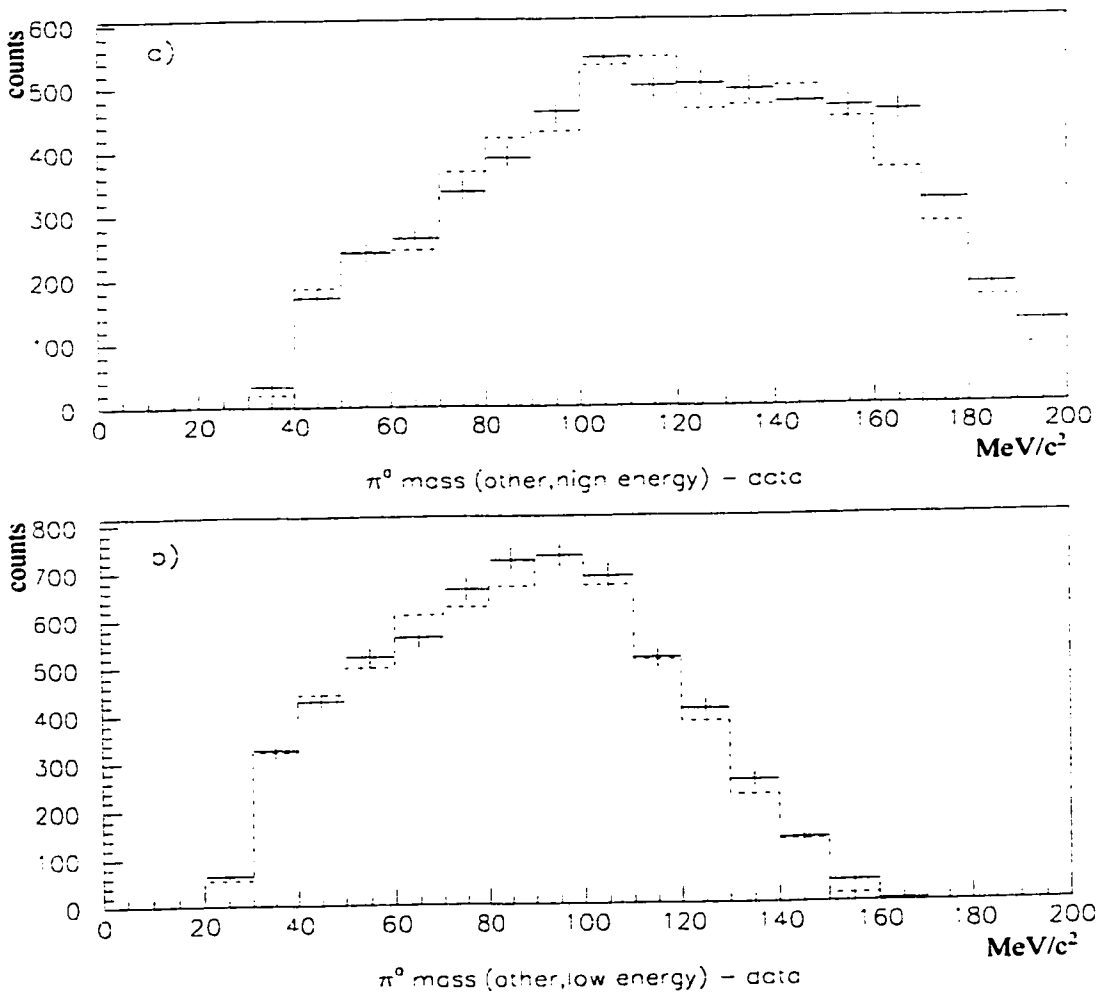

Figure 5.7: The invariant mass distributions of non selected pairings showing the good agreement between data (solid cross) and MC(poly) (dotted histogram)

Chapter 6

Background Rejection

Although comparing the peak in the $\Delta\theta$ distribution (Fig. 4.1) to the flat background gives a small background estimate of 5%, the MC simulations show that the background is actually 25% from $K^-_{\pi 2}$. Again returning to the pairing of the π^0's, Fig. 4.3 already uses several background cuts as discussed below. Fig. 6.1 shows the same distributions without any of these background cuts. The corresponding MC distributions (pure $K^-_{\pi 3}$) shows little change, yet the data shows a much broader distribution. This is evidence that the background is significant.

The background contributions from $K_{\pi 2}$ fulfill several conditions in order to mimic a $K^-_{\pi 3}$ event. Since $K^-_{\pi 2}$ decay produces only two photons at least two extra clusters must be present in the CsI. There are three distinct sources of extra clusters.

1. The π^+ hits the calorimeter

2. A single photon creates two clusters

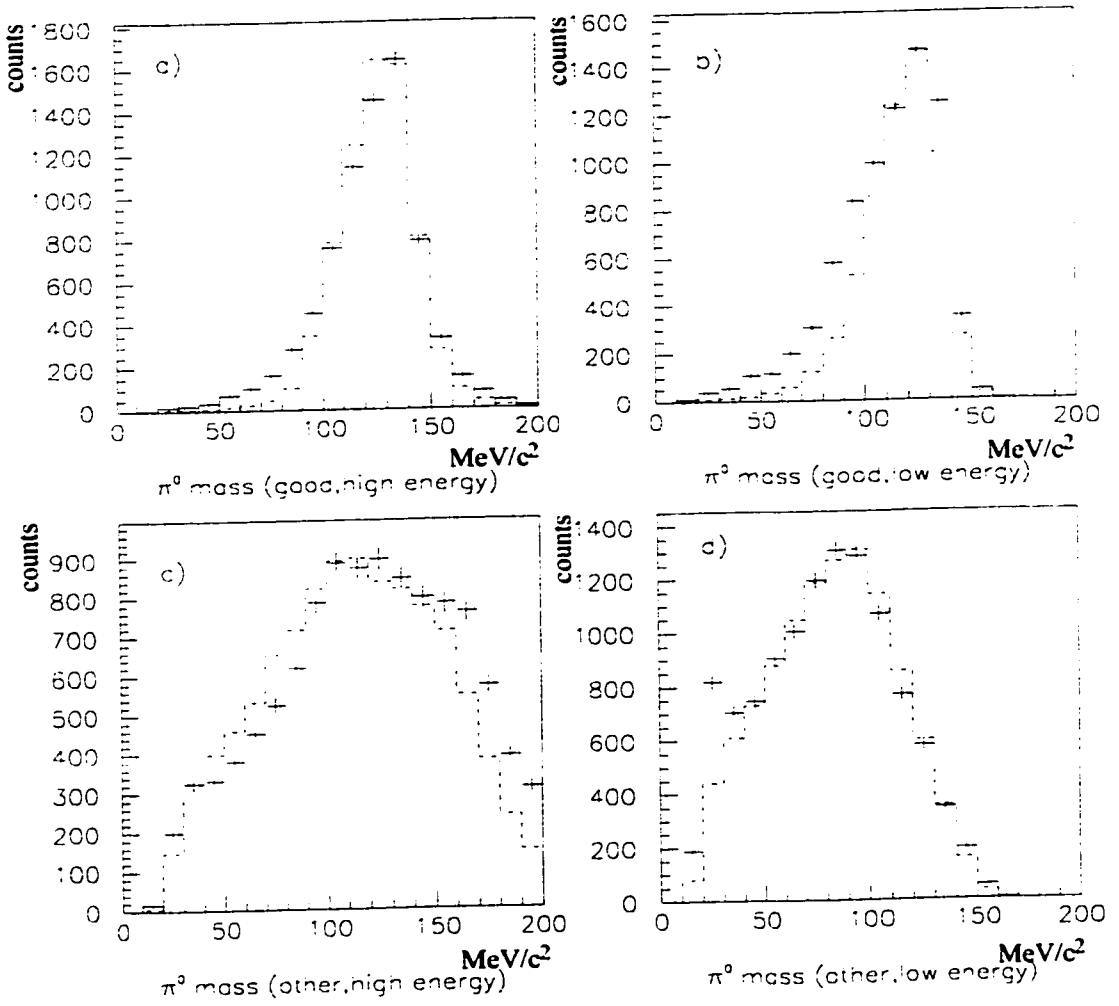

Figure 6.1: Photon pair distributions with large background

3. An accidental photon

The second source comes partially from conversion in the target and partially from secondary photons skipping over a crystal. Unlike the first two sources, the third source adds additional energy to the system. For these events, a large portion of the energy at least one of the other photons must escape (shower leakage). Otherwise these events will be easily cut by energy conservation. The acceptance of $K_{\pi 2}$ events is a factor of 70 lower than $K_{\pi 3}$ however because the branching ratio is about 12 times larger, the $K_{\pi 2}$ event rate is not negligible.

To reduce the background contamination, several different cuts were considered, to reject the background. The effort was devoted to discovering cuts that eliminate the background without substantial loss of useful events. The cuts considered were:

1. opening angle of π^0 decay: θ_{12}
2. χ^2 cut
3. low energy photon cuts: $E_{\gamma 4}$ or $\min(E_{\gamma 2}, E_{\gamma 4})$
4. high energy cut on the two highest energy photons: $E_{\gamma 1} + \max(E_{\gamma 2}, E_{\gamma 3})$
5. minimum angle cuts for all photon pairs
6. range of m_{π^0}

In the above list the photons are numbered so that $\gamma 1$ and $\gamma 2$ come from the high energy pion with $E_{\gamma 1} > E_{\gamma 2}$ and $\gamma 3$ and $\gamma 4$ come from the low energy pion with

$E_{\gamma 3} > E_{\gamma 4}$. Each of the cuts listed above are discussed in turn in the following paragraphs. There are several key considerations, coming from the kinematics of two body decay, common to all cuts. One feature is the high energy π^0 which tends to produce either two photons at small angles or one low and one high energy photon. Secondly, when one photon creates two clusters tend to produce lower energy photons with a small opening angle.

The first cut considers the opening angle between the photons of the high energy π^0. The distribution of this angle, denoted θ_{12}, is shown in Fig. 6.2. The $K_{\pi 2}$ MC spectrum has two peaks, one near $\cos\theta_{12} = -1$ and the second near 0.4. However the $K_{\pi 3}$ MC and data have a peak near -0.2 with the data having a flatter distribution because of the background. In order to achieve significant background rejection, $\cos\theta_{12} > -0.5$ is required. Thus the background has mostly photons being produced in opposite directions. Not only is this contrary to our expectation but this cut kills about 30% of the $K_{\pi 3}$ events and only reduces the background to 22%. This cut is not used although, as will be shown later, a more effective cut (5) also based on the angles was found.

Another cut that was considered started by defining

$$\chi^2 = \frac{(M_{12} - m_{\pi^0})^2}{\sigma_h^2} + \frac{(M_{34} - m_{\pi^0})^2}{\sigma_l^2} \tag{6.1}$$

which is the same as the quality factor (4.14) except for the division by σ^2 where σ_h and σ_l are the widths of the mass distributions. From the MC simulations, $\sigma_h = 15.7$ MeV and $\sigma_l = 14.1$ MeV. The resulting distributions are shown in Fig. 6.3. $K_{\pi 3}$

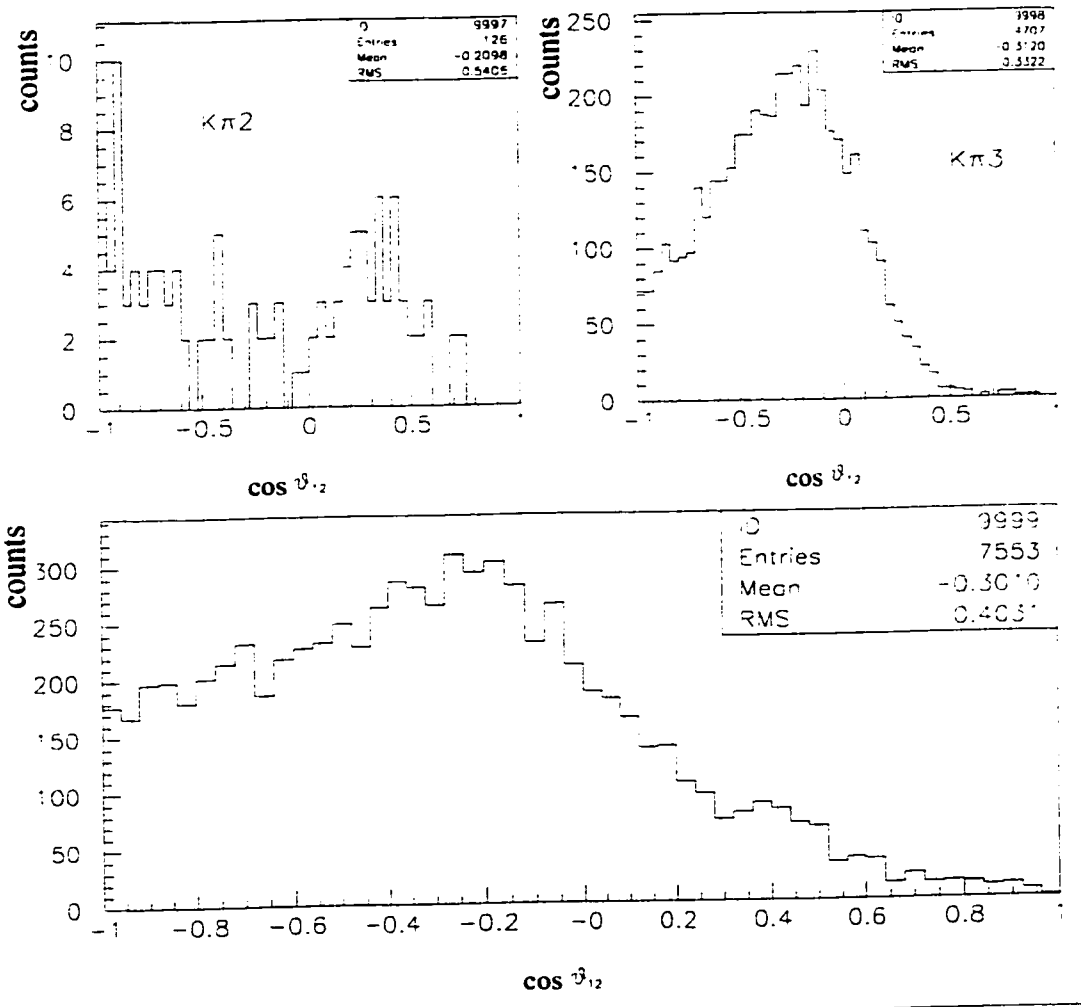

Figure 6.2: Comparing MC with data: $\cos\theta_{12}$. The upper figures ($K_{\pi 2}$ and $K_{\pi 3}$) come from MC and lower (unlabeled) figure is real data.

(MC) has χ^2 extending up to 20 with a peak near 0. In contrast, the $K_{\pi 2}$ (MC) has peak 10 with very few events above 20. Accepting events with $\chi^2 < 20$ retains about 97% of $K_{\pi 3}$ events, the background remains 20%. This is not a very effective cut and therefore was not used.

The third cut to be considered was placing a cut on the lower energy photon associated with the lower energy pion. Requiring $E_{\gamma 4} > 40$ MeV reduces the background to 12% and retains 81% of $K_{\pi 3}$ events. This distribution is shown in Fig. 6.4. As to be expected, the $K_{\pi 2}$ contamination is concentrated at energies below 40 MeV, whereas $K_{\pi 3}$ (MC) peaks around 60 MeV. However it was found that placing a cut on the lowest energy photon $\min(E_{\gamma 2}, E_{\gamma 4}) > 35$ MeV had a slightly lower background of 11% yet still retained 80% of $K_{\pi 3}$. The distributions, shown in Fig. 6.5, are very similar to those of Fig. 6.4. This cut was adopted and is applied to the following discussion.

The next cut looks at the sum of the two highest energy photons which is shown in Fig. 6.6. The $K_{\pi 2}$ peaks around 210 MeV, and $K_{\pi 3}$ peaks 190 MeV and extends up to 250 MeV. In this case we reject events with $E_{\gamma 1} + \max(E_{\gamma 2}, E_{\gamma 3}) > 220$ MeV. This further reduces the background to 7.8% while rejecting only 7.8% of the remaining events. This cut is also selected for further analysis.

As promised, we look again at placing a photon angle cut. In this case we look at the smallest angle between the photons instead of the opening angle of the higher energy π^0. The $K_{\pi 3}$ MC distribution is nearly flat in the region from 0.5 to 1 rad but drops sharply below 0.5 rad. The $K_{\pi 2}$ still shows a double peak. However, the

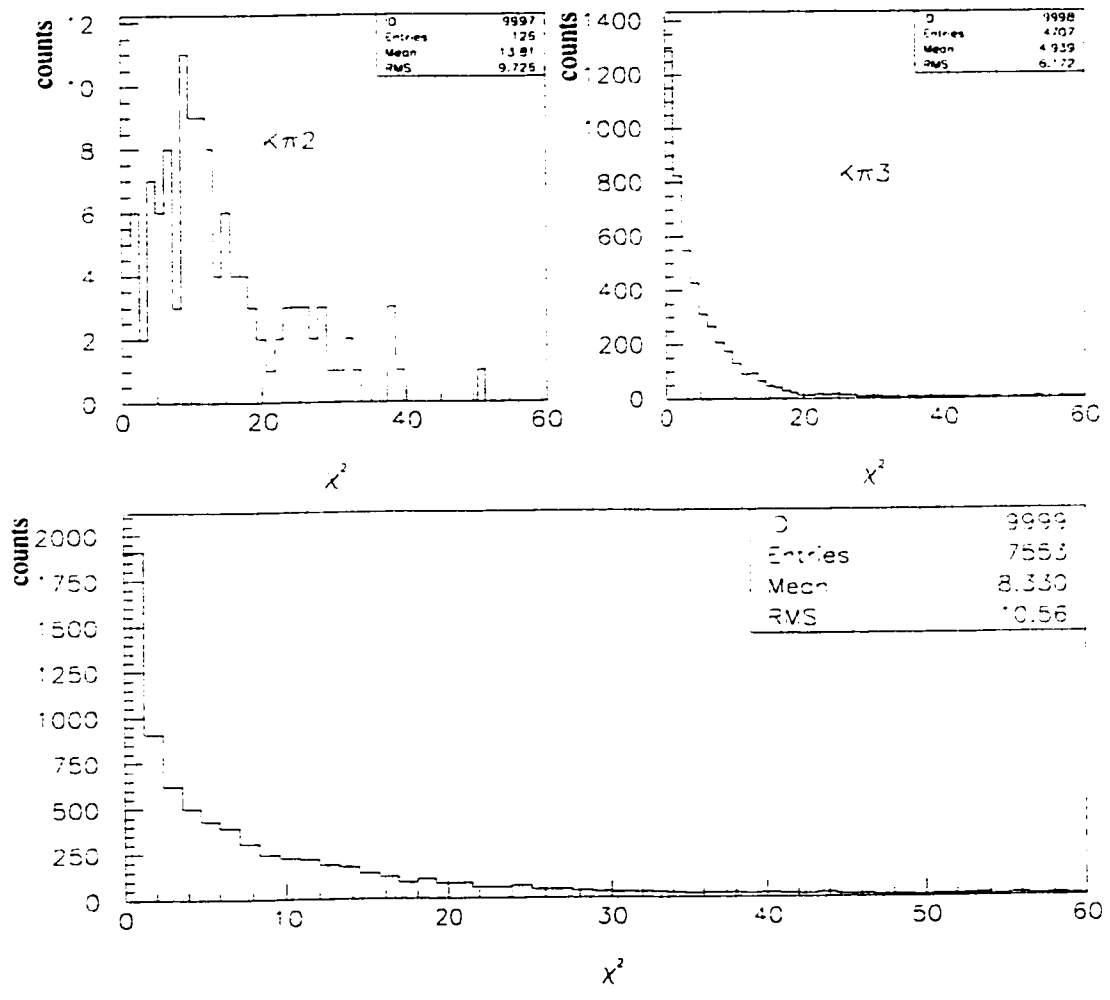

Figure 6.3: Comparing MC with data: χ^2. The upper figures ($K_{\pi 2}$ and $K_{\pi 3}$) come from MC and lower (unlabeled) figure is real data.

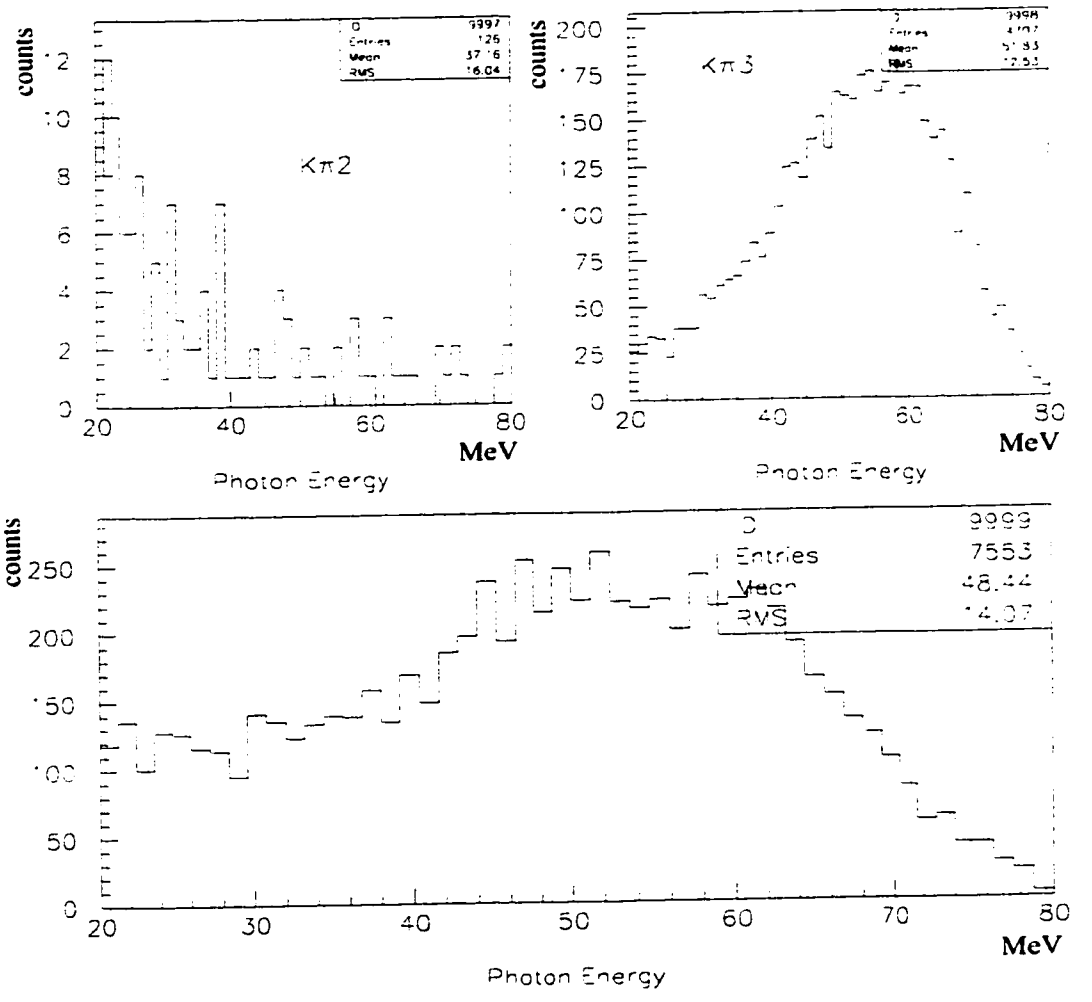

Figure 6.4: Comparing MC with data: $E_{\gamma 4}$. The upper figures ($K_{\pi 2}$ and $K_{\pi 3}$) come from MC and lower (unlabeled) figure is real data.

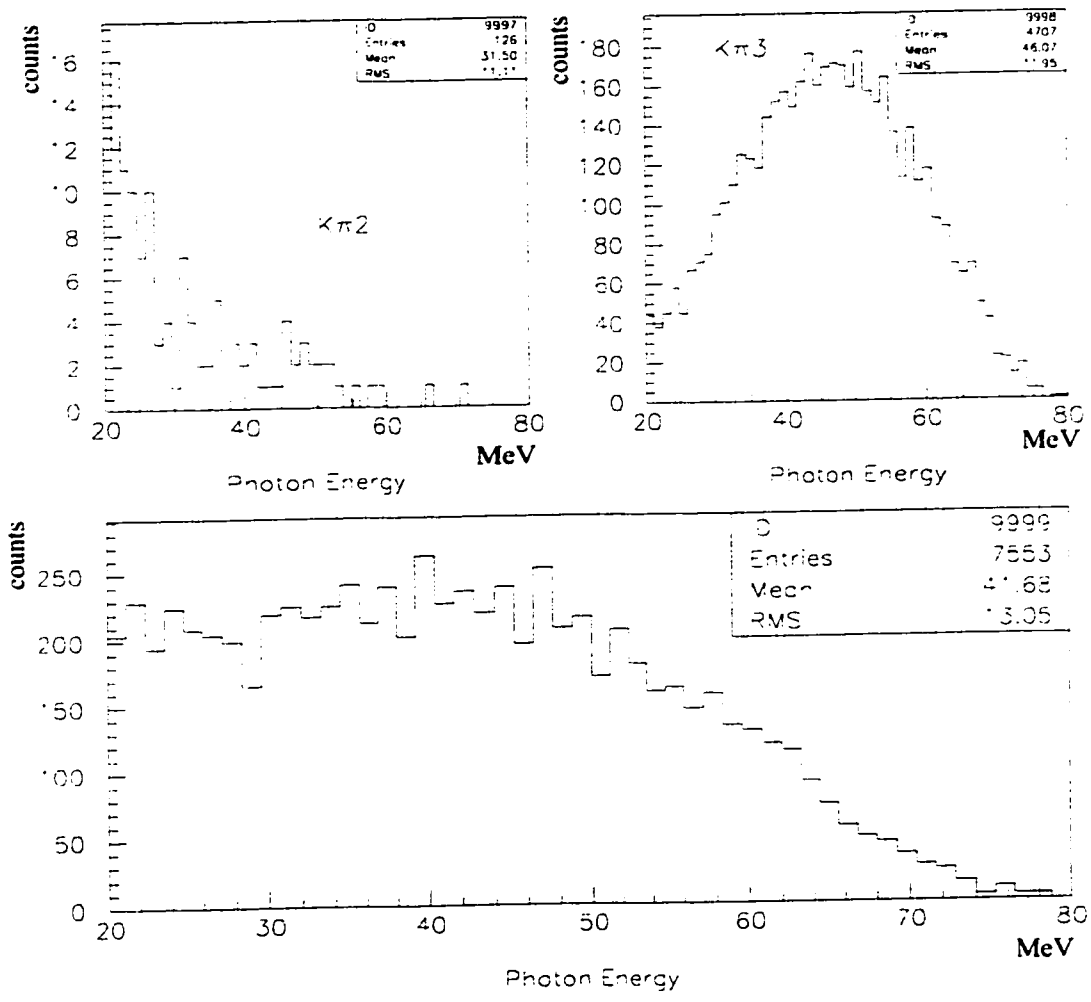

Figure 6.5: Comparing MC with data: $\min(E_{\gamma 2}, E_{\gamma 4})$. The upper figures ($K_{\pi 2}$ and $K_{\pi 3}$) come from MC and lower (unlabeled) figure is real data.

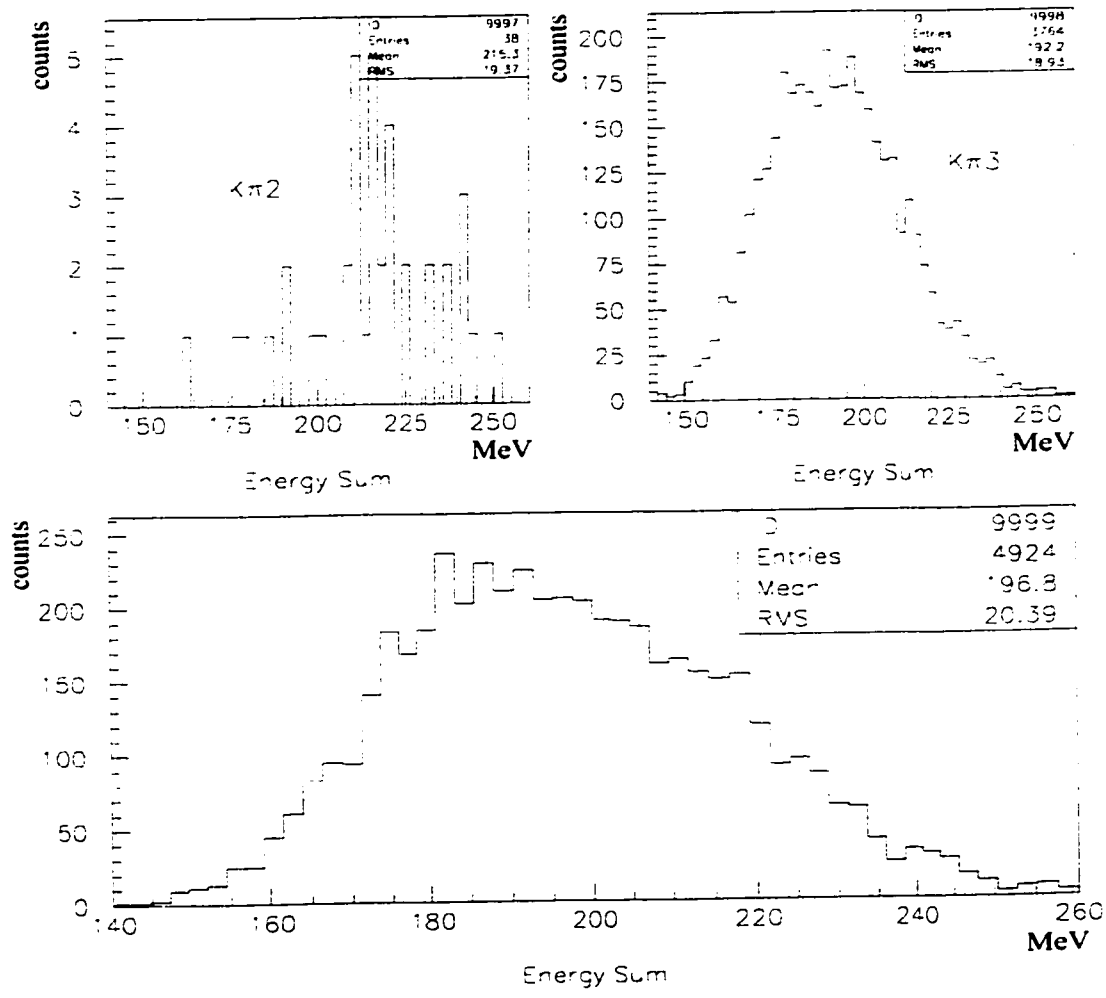

Figure 6.6: Comparing MC with data: $E_{\gamma 1} + \max(E_{\gamma 2}, E_{\gamma 3})$. The upper figures ($K_{\pi 2}$ and $K_{\pi 3}$) come from MC and lower (unlabeled) figure is real data.

energy cuts have greatly reduced anti-parallel peak. as shown in Fig. 6.7. Rejecting events below 0.5 rad keeps 82% of $K_{\pi 3}$ events and reduces the background to 4.9%. This is very effective cut and is retained for further analysis.

The last cut to be considered is a restriction on m_{π^0}. The same mass selection. $60 < m_{\pi^0} < 160$. was used for both high and low energy photons. As shown in Figs. 6.8 and 6.9. this has very little effect on the low energy π^0 or the high energy. Adopting this cut reduces the final background level to 3.4%

Since this background level is quite small, we conclude that this contamination will have no impact on the determination of scattering lengths.

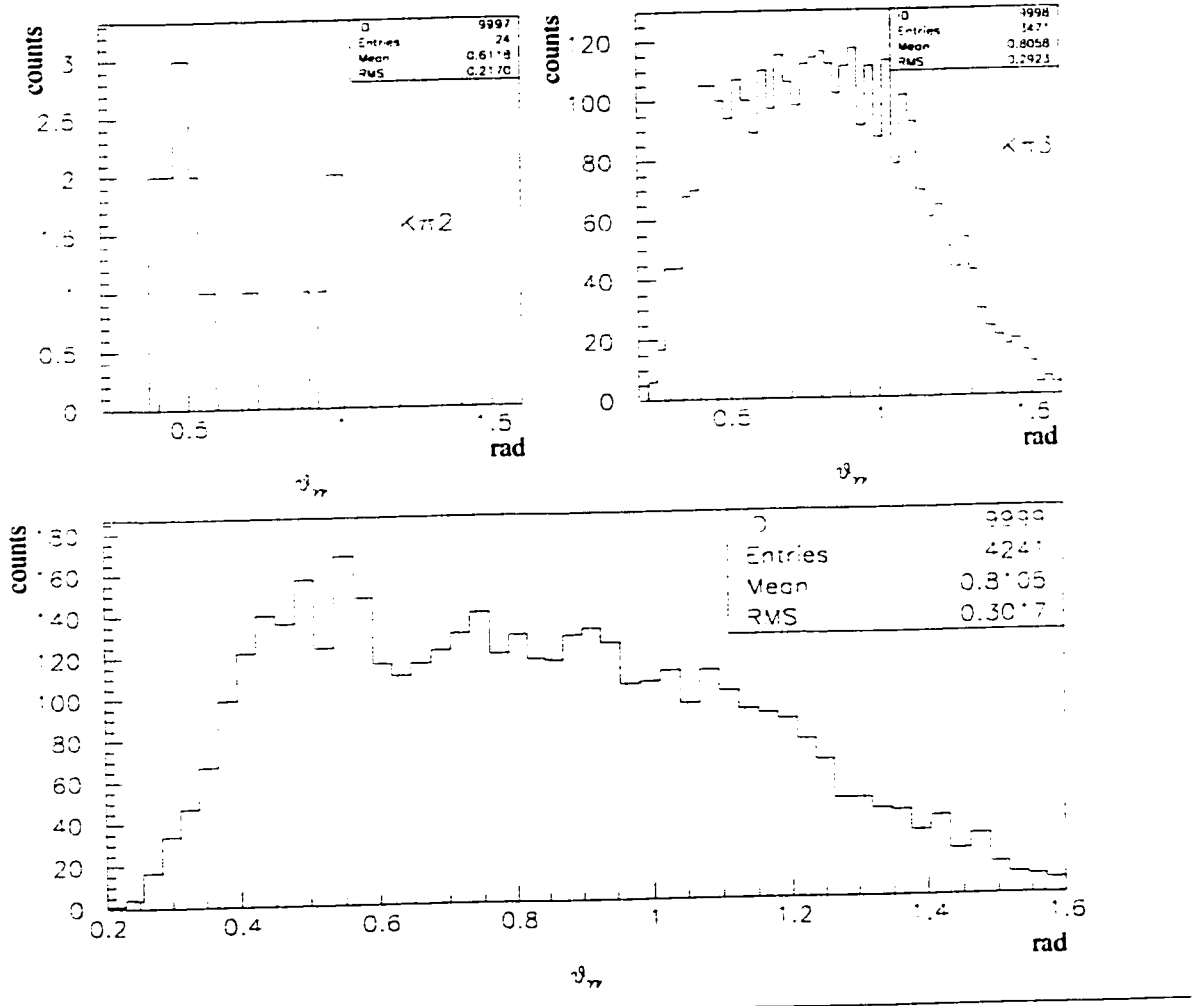

Figure 6.7: Comparing MC with data: minimum photon separation. The upper figures ($K_{\pi 2}$ and $K_{\pi 3}$) come from MC and lower (unlabeled) figure is real data.

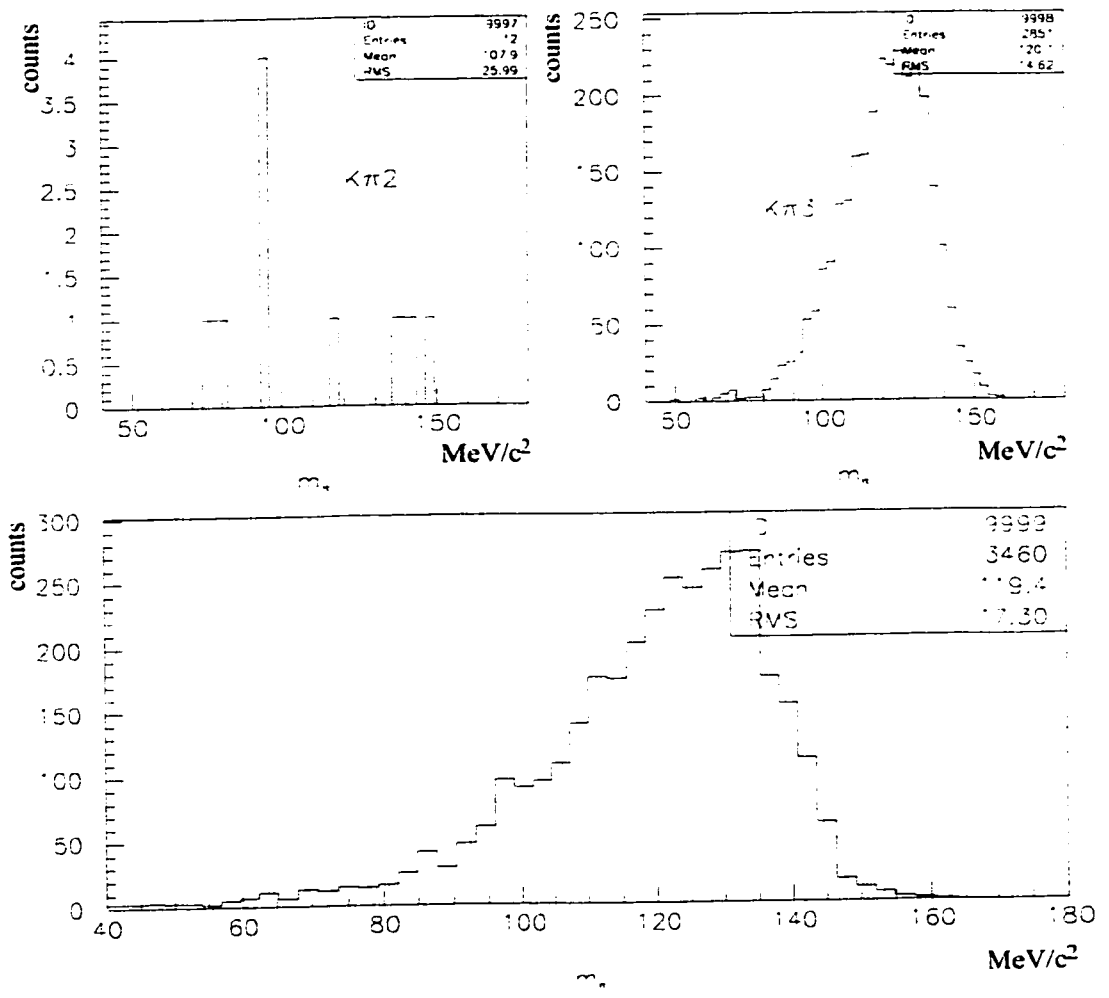

Figure 6.8: Comparing MC with data: m_{π^0} low energy. The upper figures ($K_{\pi 2}$ and $K_{\pi 3}$) come from MC and lower (unlabeled) figure is real data.

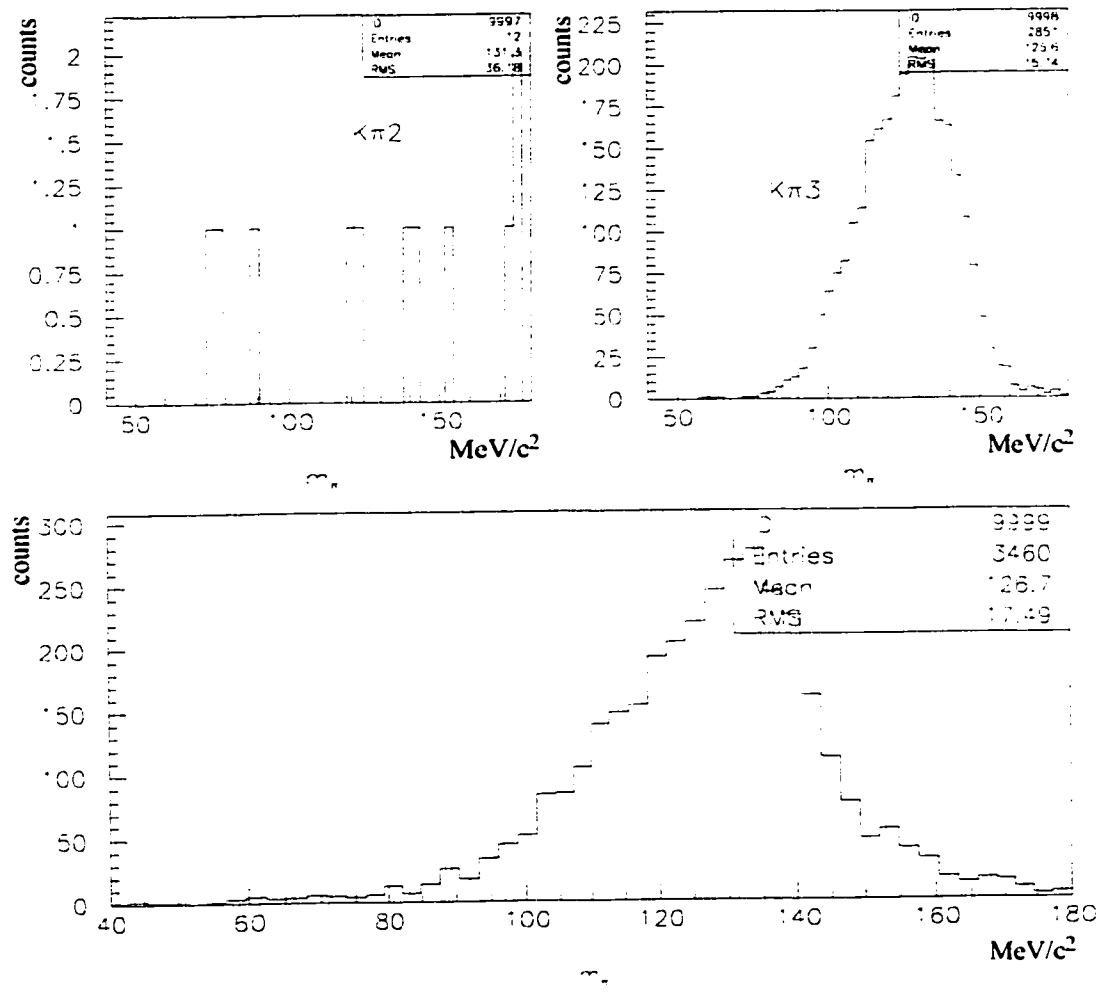

Figure 6.9: Comparing MC with data: m_{π^0} high energy. The upper figures ($K_{\pi 2}$ and $K_{\pi 3}$) come from MC and lower (unlabeled) figure is real data.

Chapter 7

Determination of Scattering Lengths

We tried many methods to deduce the scattering lengths. A common feature of all these methods was the comparison of data to MC spectra. Most of these methods failed due to two aspects. One problem is that many events have s_1 and s_3 values seemingly outside of the physical region. The fact that MC(3bps) has the same spread, as shown in Fig. 7.1, indicates that the events outside the kinematics limits are actually good events. The second problem was extremely high correlations between the two scattering lengths. This meant that almost any change in one parameter could be compensated for by an appropriate change in the second parameter.

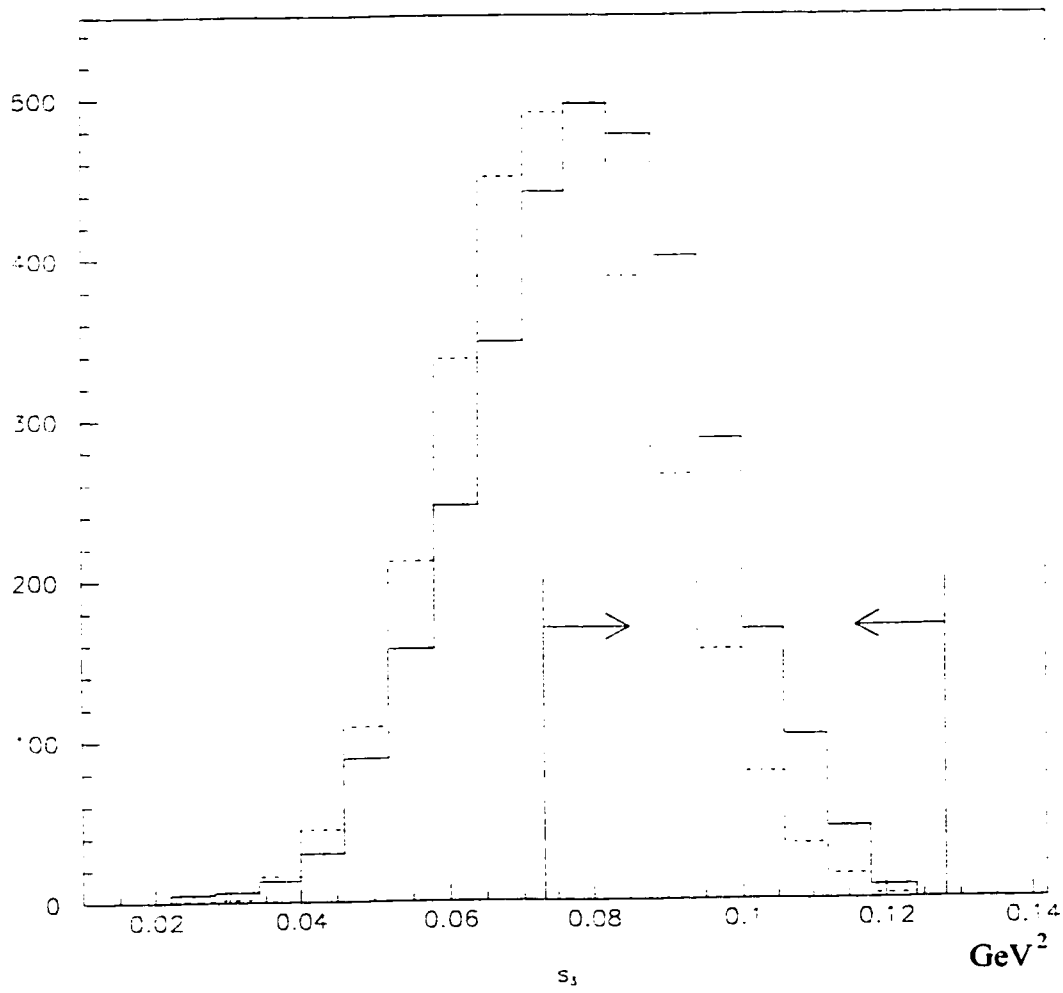

Figure 7.1: The s_3 distribution for both data (solid) and MC (dashed). Also shown is the kinematic limits for s_3. Although these two distributions are different because of different matrix elements, the observed range of s_3 is identical.

7.1 Decay width to Cross Section Conversion: Normalization

The first method was both highly convoluted and ignored most of the data. The first step of this method normalized the decay distribution to the partial width of $K_{\pi 3}$ decay. Secondly, the decay distribution was converted to scattering cross section by manipulating phase space factors. The conversion was found to be

$$\sigma(\varepsilon) = \frac{4M_K\pi^2}{p_a^2} \left.\frac{d\Gamma}{ds}\right|_{s=\varepsilon^2} \tag{7.1}$$

where ε is the center of mass energy, M_K is the kaon mass and p_a is center of mass momentum of the final pions, *i.e.* either $\pi^0\pi^0$ or $\pi^+\pi^0$. Although not shown explicitly, both the cross section σ and the decay width $\frac{d\Gamma}{ds}$ are proportional to $|\mathfrak{M}|^2$, where $\mathfrak{M}$ is the matrix element. This conversion was done for both data and MC. Finally, the data distribution was divided by MC to obtain the final distribution which is simply $|\mathfrak{M}|^2$. This distribution was then fit to the function shown in eqn.(7.2) to obtain the scattering lengths. As shown in Fig. 7.1, the decay distribution shows significant spread beyond the nominal physical region for both data and MC. However buried in the conversion is a factor of $s - 4m_\pi^2$ which is negative below the physical threshold. Thus the converted cross section outside this kinematic region became unphysical and were not used in the fit. This meant that a large fraction of otherwise acceptable events were ignored. This conversion was necessary simply because of the normalization requirement. Therefore the normalization was dropped in order to use

nearly all of the data.

7.2 Fitting with Monte Carlo Distributions

The second method attempted to fit the observed distribution using MC distributions for each term in the matrix element[2]. A total of six different Monte Carlo spectrums were generated.

1. constant (*i.e.* three body phase space)
2. $\frac{\sqrt{s_3}}{3}$
3. $\frac{\sqrt{s_1}+\sqrt{s_2}}{2} - \frac{\sqrt{s_3}}{3}$
4. $\frac{s_3}{9}$
5. $\frac{\sqrt{s_3}}{3}\left(\frac{\sqrt{s_1}+\sqrt{s_2}}{2} - \frac{\sqrt{s_3}}{3}\right)$
6. $\left(\frac{\sqrt{s_1}+\sqrt{s_2}}{2} - \frac{\sqrt{s_3}}{3}\right)^2$

Each of these terms is multiplied by some combination of a_0^0 and a_0^2 as shown in equation (7.2). In addition to the high correlation between the two scattering lengths, some of the distributions were nearly identical. The combination of these two factors made it impossible to uniquely determine the scattering lengths.

7.3 Polynomial Fit after Resolution Correction

Three fundamental changes in philosophy occurred at this point. The first was a shift from focusing on one dimensional distributions to two dimensional distributions, specifically s_1 vs. s_3. The second is that the MC was used to correct for the resolution[37]. The third change is that the scattering lengths were no longer directly used in the fitting.

The MC events are the key to the resolution correction. With these MC events, the exact (or "at birth") values of s_1 and s_3 are known in addition to the observed (or "measured") values. The observed values are split into several bins in s_1 and s_3. This distribution is shown in Fig. 7.2. For each of these bins, the distribution of the exact values is found. Examples of these distributions are shown in Fig. 7.3 for observed values in the physical region and Fig. 7.4 for unphysical region. These distributions, after dividing by number of entries, become the "deconvolution" matrices. The data is split into identical bins and then each bin is multiplied by the corresponding "deconvolution" matrix. This creates the corrected data distribution. The original distribution is shown in Fig. 7.5 and the corrected distribution is shown in Fig. 7.6

The corrected distribution is divided by the corresponding exact MC distribution. A narrow slice in s_1 was chosen for the fit. In this slice s_1 becomes a constant and s_2 becomes a simple function of s_3. The fit function is

$$|\mathfrak{M}|^2 = const. + \left(\frac{a_0^0}{2\lambda_\pi}\right)\frac{\sqrt{s_3}}{3} + \left(\frac{a_0^2}{2\lambda_\pi}\right)\left[\frac{\sqrt{s_1}+\sqrt{s_2}}{2} - \frac{\sqrt{s_3}}{3}\right] \tag{7.2}$$

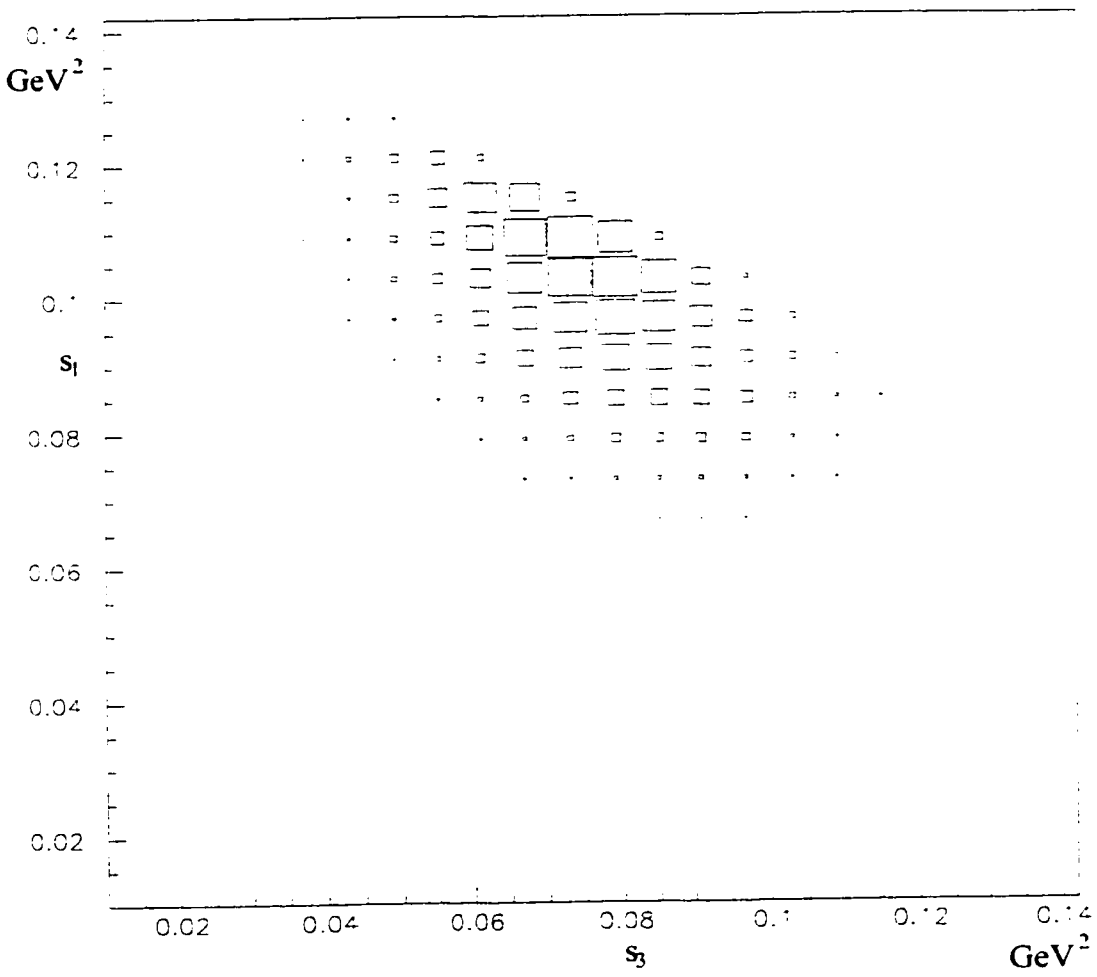

Figure 7.2: The observed s_1 vs. s_3 distribution from Monte Carlo simulation

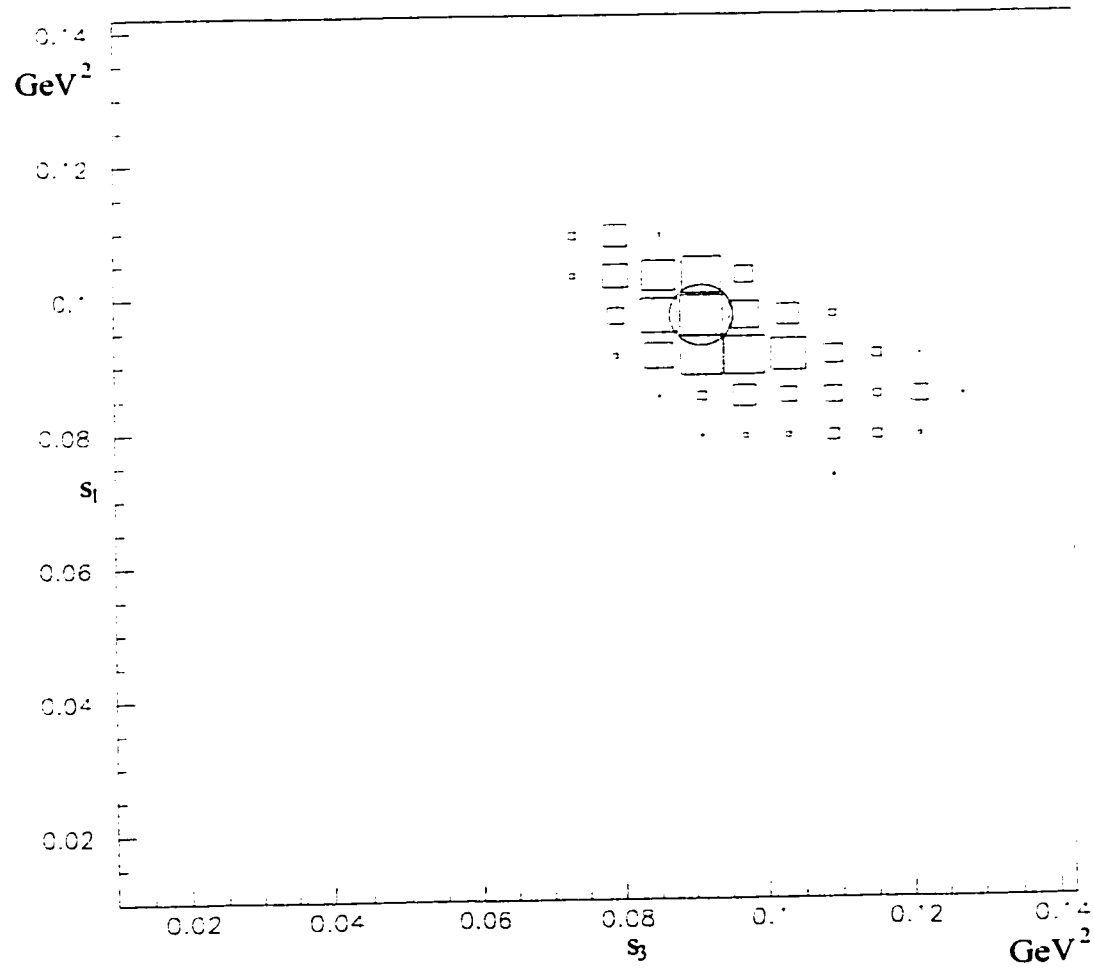

Figure 7.3: The exact s_1 vs. s_3 distribution for an observed s_1 and s_3 value in the physical region. The circle denotes the observed bin.

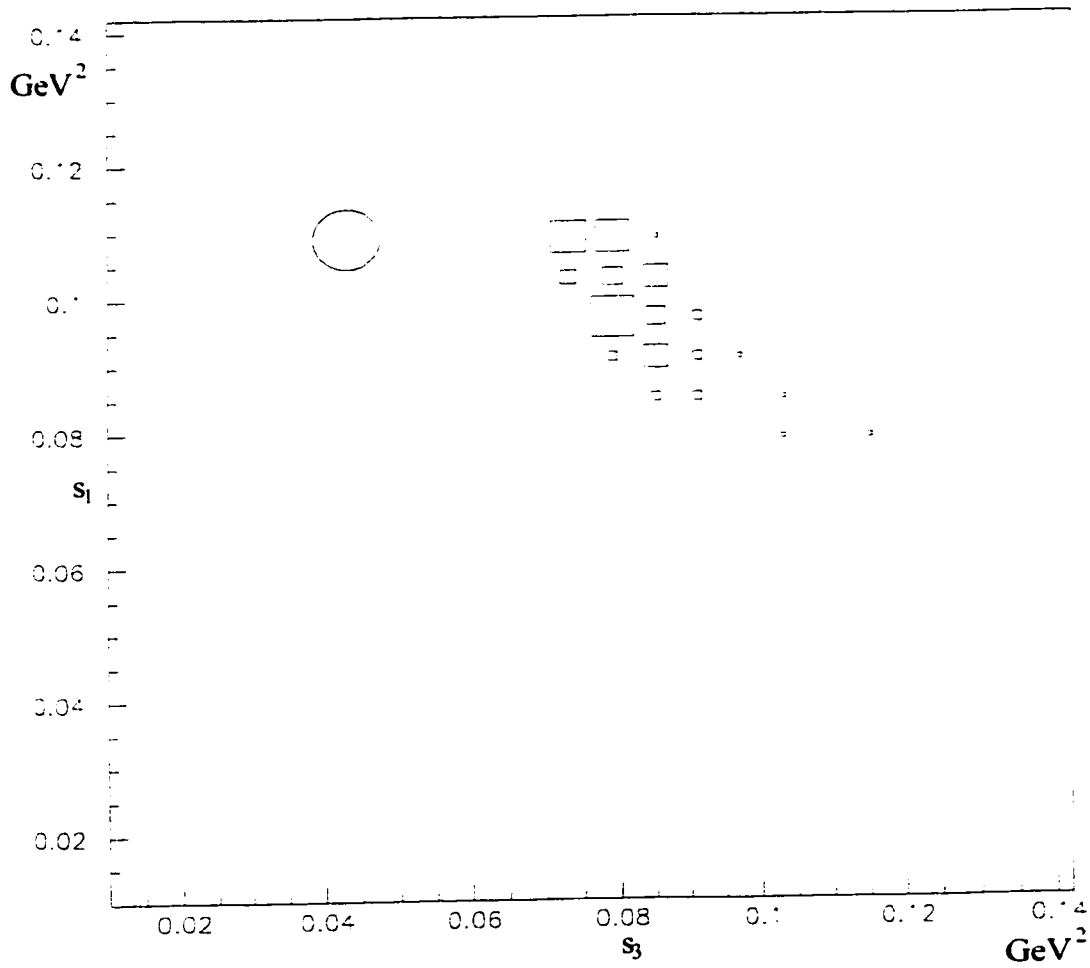

Figure 7.4: The exact s_1 vs. s_3 distribution for an observed s_1 and s_3 value in the unphysical region. The circle denotes the observed bin.

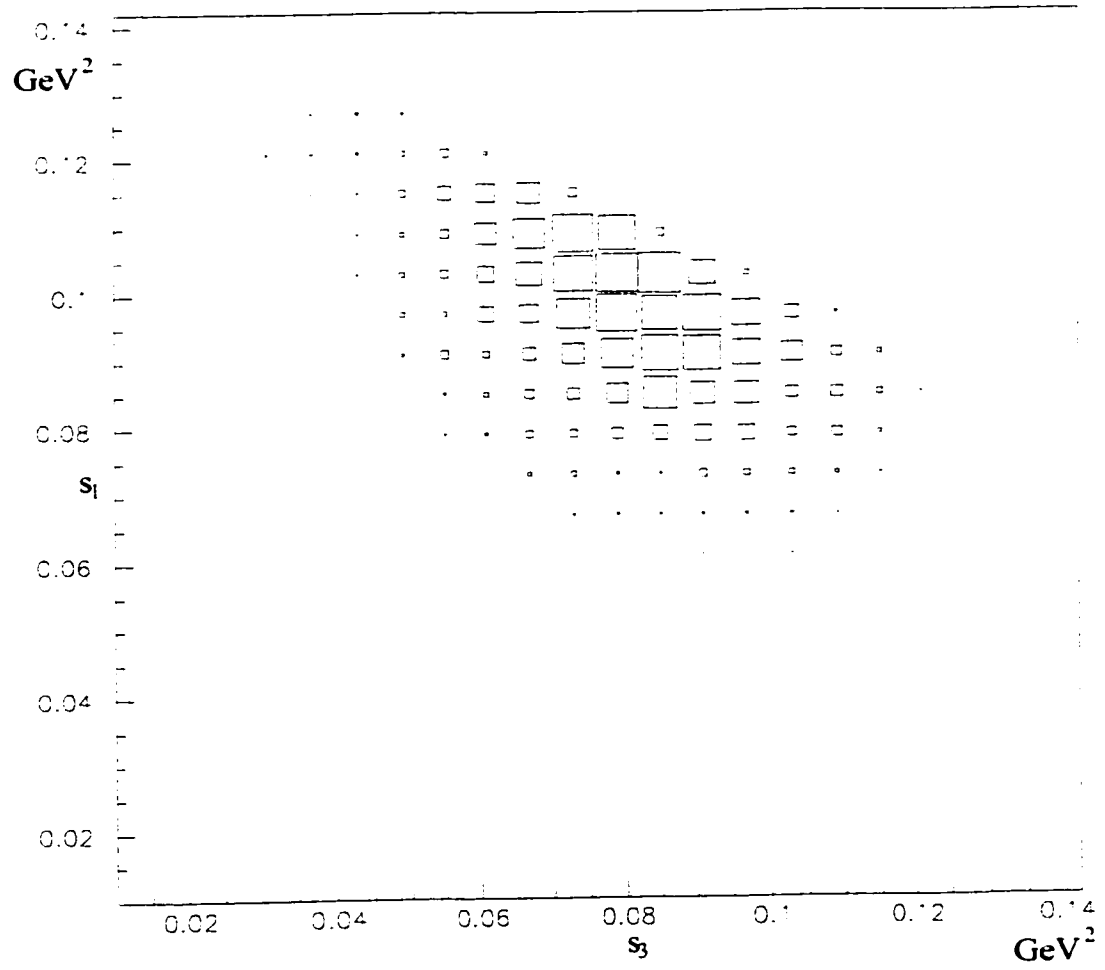

Figure 7.5: The s_1 vs. s_3 distribution of data before resolution correction.

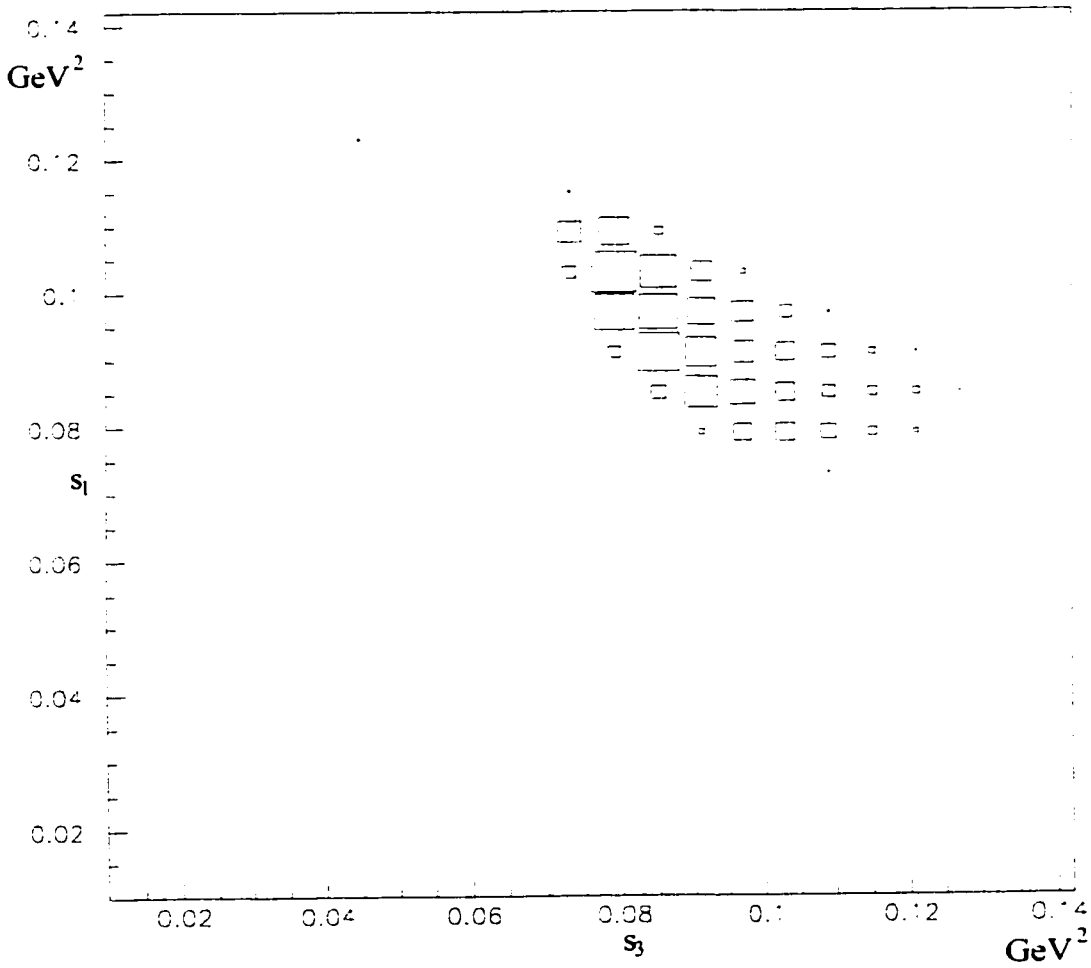

Figure 7.6: The s_1 vs. s_3 distribution of data after resolution correction.

$$+\frac{1}{4}\left(\frac{a_0^0}{2\lambda_\pi}\right)\left(\frac{a_0^0}{2\lambda_\pi}\right)\frac{s_3}{9}+\frac{1}{2}\left(\frac{a_0^0}{2\lambda_\pi}\right)\left(\frac{a_0^2}{2\lambda_\pi}\right)\frac{\sqrt{s_3}}{3}\left[\frac{\sqrt{s_1}+\sqrt{s_2}}{2}-\frac{\sqrt{s_3}}{3}\right]$$
$$+\frac{1}{4}\left(\frac{a_0^2}{2\lambda_\pi}\right)\left(\frac{a_0^2}{2\lambda_\pi}\right)\left[\frac{\sqrt{s_1}+\sqrt{s_2}}{2}-\frac{\sqrt{s_3}}{3}\right]^2+\cdots$$

By approximating $\sqrt{s_2}$ as a second order polynomial in $\sqrt{s_3}$ and treating s_1 as a constant, the above function simply becomes a second order polynomial. The approximation of $\sqrt{s_2}$ used the Lagrange multiplier method with three points chosen as $\frac{1}{6}, \frac{1}{2}, \frac{15}{16}$ of the fitting interval which optimizes the approximation. The fit for one slice ($0.094< s_1 <0.100$) is shown in Fig. 7.7. After fitting to the polynomial, the output was then entered into a MAPLE[1] script which extracted the scattering lengths. Note that what is actually determined are the ratios $a_0^0/2\lambda_\pi$ and $a_0^2/2\lambda_\pi$ and to extract the scattering lengths, λ_π must be fixed. The χPT prediction for λ_π is used.

$$\lambda_\pi = -\frac{m_\pi^2}{96\pi F_\pi^2} = -7.44\times 10^{-3} \tag{7.3}$$

where $F_\pi = 0.0935$ is the pseudoscalar decay constant. This fitting procedure is repeated for several different slices of s_1. The fit for the remaining slices is shown in Fig. 7.8.

The results of these fits are summarized in Table 7.1 for each of the slices. Also shown are the statistical and fitting errors. There are two sources for the fitting errors. The first comes from the finite width of s_1. This error was determined by running the MAPLE script for the extreme values instead of the midpoint. The second source of error is due to the approximation of $\sqrt{s_2}$. The error from this was estimated by

[1]MAPLE is symbolic algebra and numerical analysis program developed at Univ. of Waterloo, Canada

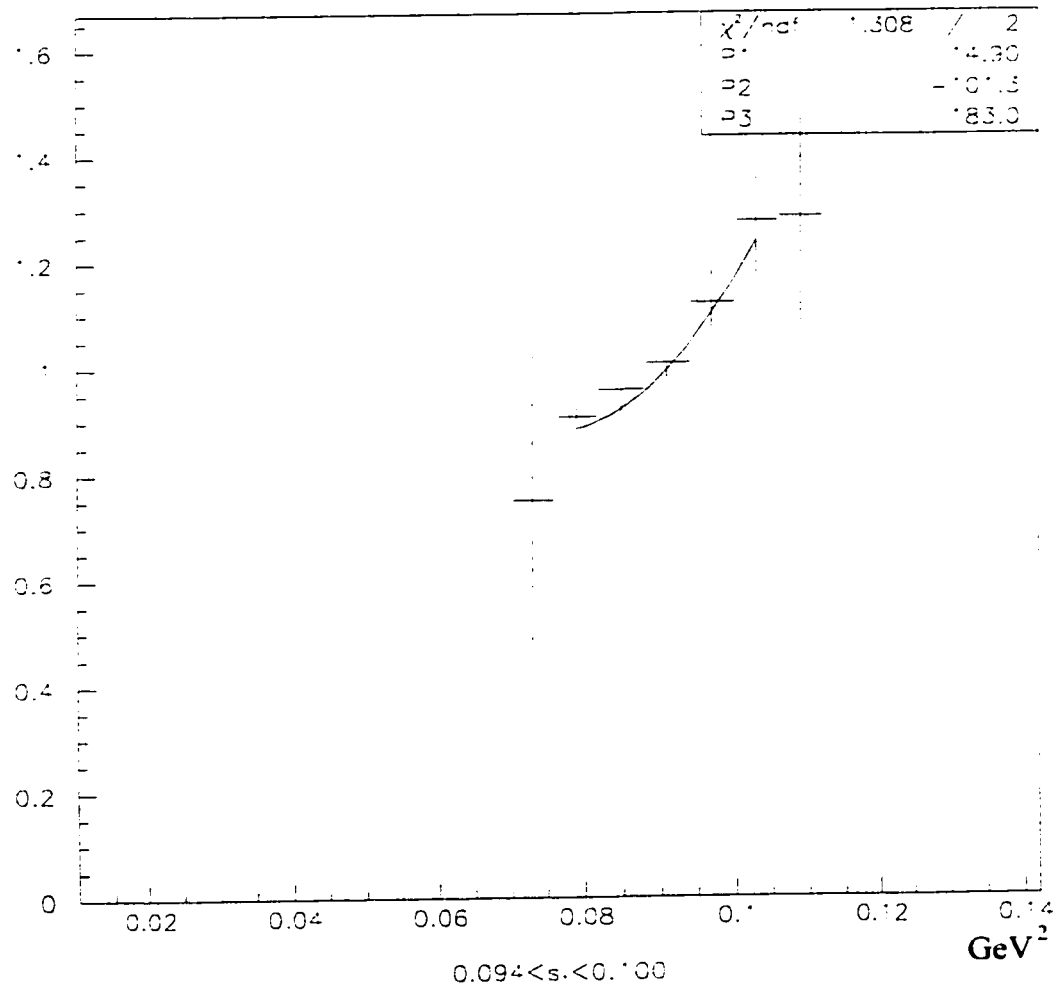

Figure 7.7: The divided distribution for 0.094< s_1 <0.100 GeV^2 showing polynomial fit.

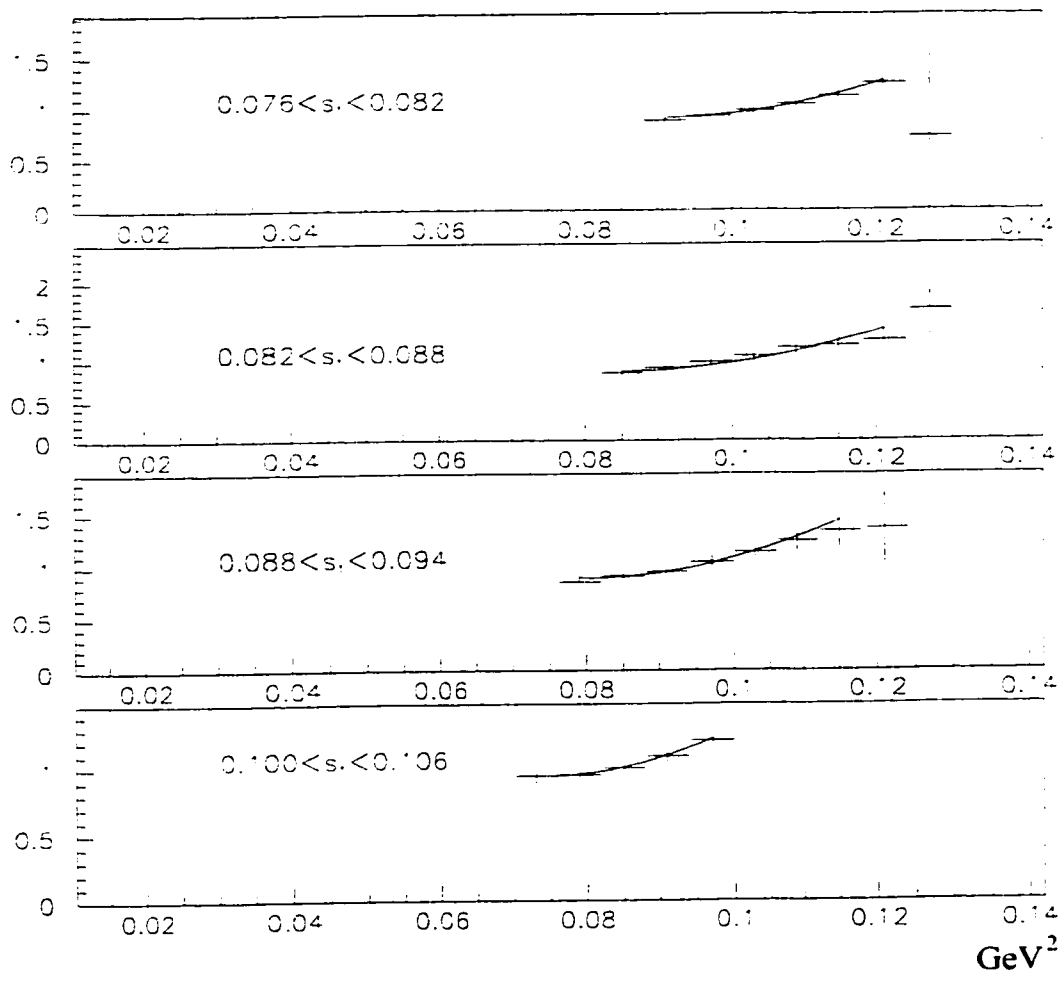

Figure 7.8: The divided distribution for various slices in s_1 showing the polynomial fit.

Table 7.1: The scattering lengths for various ranges of s_1. Note that there is a very slight dependence except for $0.076 < s_1 < 0.082$ which shows a larger shift. The errors shown are the statistical and fitting errors respectively. The last row is an extrapolation of these results to threshold.

Range	$a_0^0(m_\pi^{-1})$	$a_0^2(m_\pi^{-1})$
$0.076 < s_1 < 0.082$	0.202±0.005±0.004	-0.0301±0.0020±0.0003
$0.082 < s_1 < 0.088$	0.199±0.004±0.004	-0.0286±0.0017±0.0003
$0.088 < s_1 < 0.094$	0.198±0.004±0.004	-0.0281±0.0016±0.0002
$0.094 < s_1 < 0.100$	0.198±0.004±0.004	-0.0280±0.0017±0.0002
$0.100 < s_1 < 0.106$	0.198±0.004±0.003	-0.0281±0.0017±0.0002
Weighted Average	0.199± 0.003	-0.0285± 0.0008

varying the region over which the approximation was optimized. As seen in Fig. 7.9 and Fig. 7.10. there is a slight dependence on the s_1 range used with larger dependence near the s_1 threshold. This change is either due to the truncation of the expansion in the matrix element or due to changing dynamics such as higher partial waves or other final state interactions. Since this dependence is small, a weighted average of these values is appropriate. This average is also shown in Table. 7.1

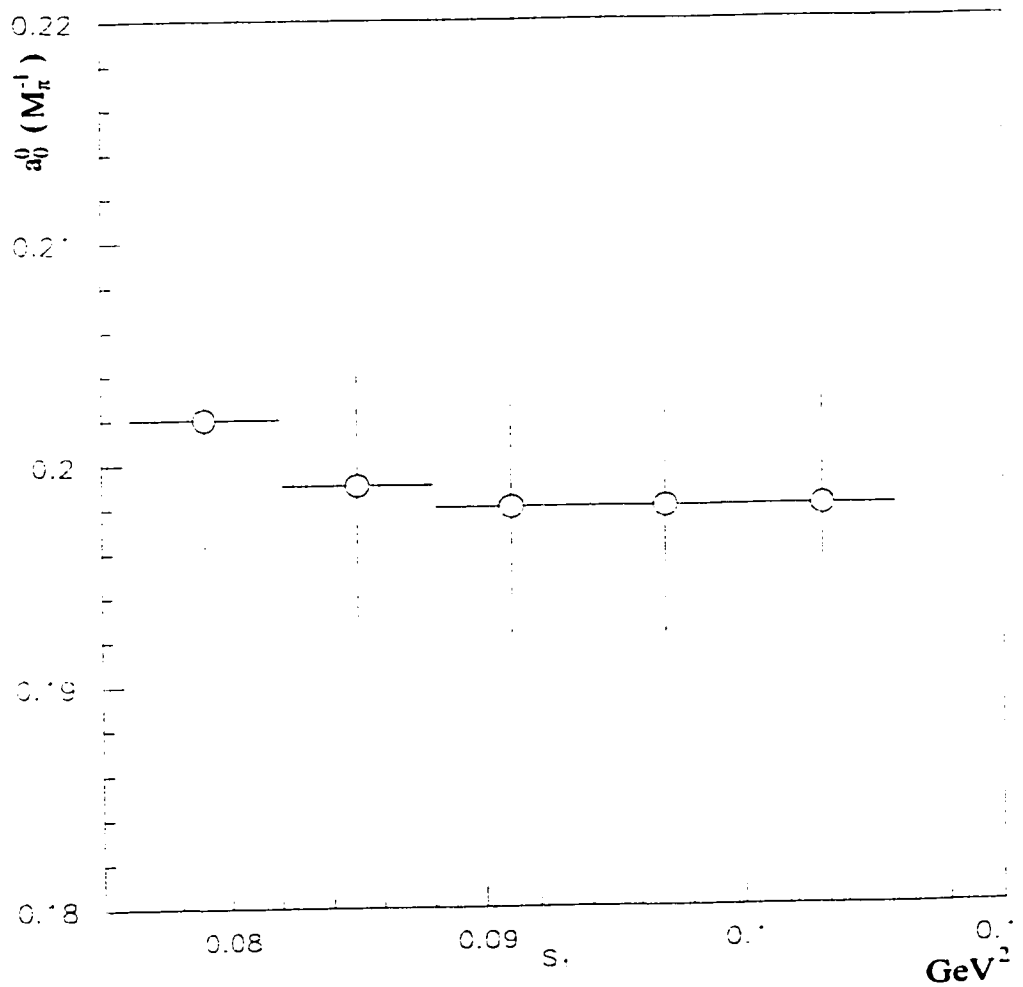

Figure 7.9: The scattering length a_0^0 as a function of s_1.

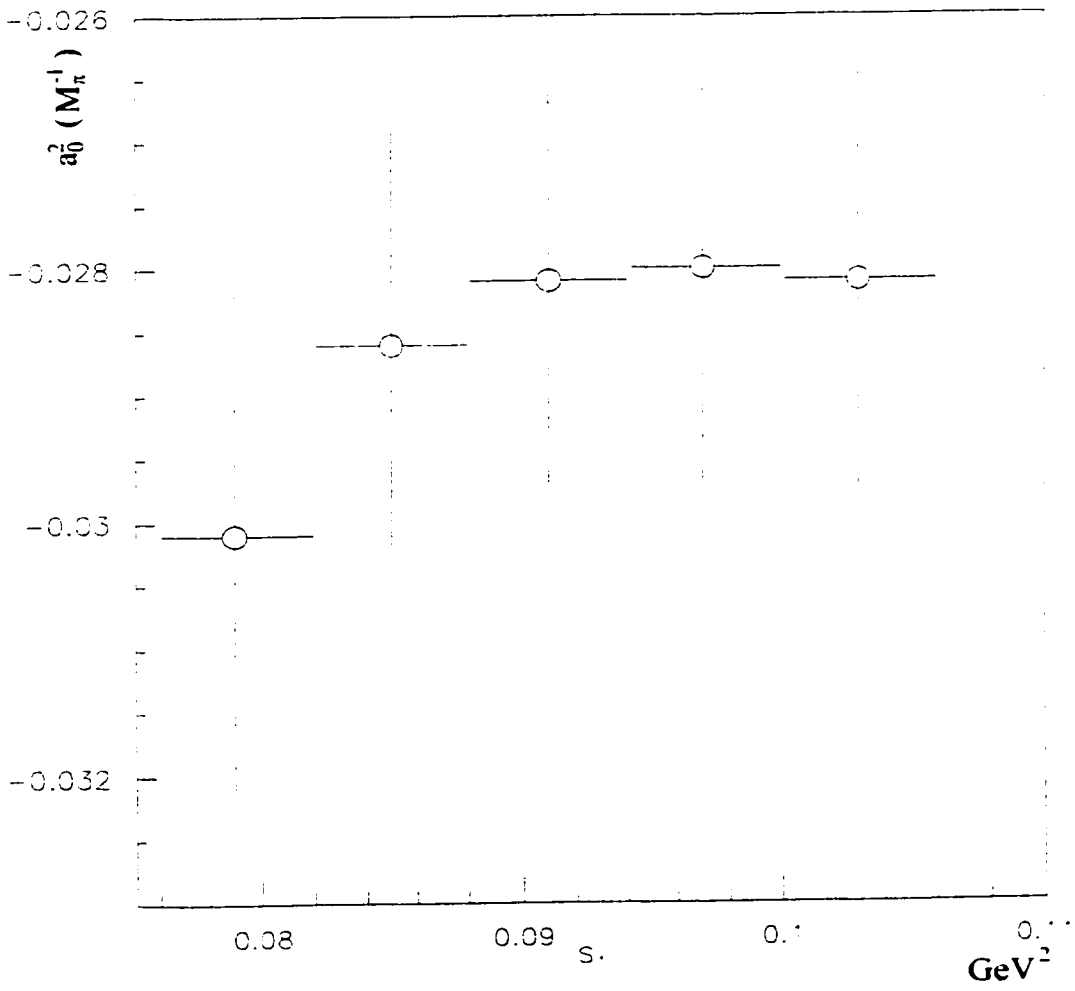

Figure 7.10: The scattering length a_0^2 as a function of s_1.

Chapter 8

Systematic errors

The main source of systematic error comes from the potential bias introduced by the various cuts. The contribution from positioning errors are negligible since the resolution and segmentation are much larger than the positioning accuracy. The segmentation for (x, y) coordinates of target is 0.5 cm and is about 7.5° for the calorimeter. As shown in Fig. 8.1, the resolution for z coordinate determination is about 8 cm.

Another potential source of systematic error comes from gain drift in CsI. However the runs used in the $K_{\pi 3}$ study are short and also used to calibrate this detector. In addition, each cycle was calibrated independently and showed very little drift, thus eliminating this as a source of error.

The following paragraphs discuss each of the background cuts in turn. These cut point dependencies are due, in part, to the change in the background. Therefore these estimates contain the systematics due to background. Note that the values shown in

the following figures are not the scattering lengths, rather they are raw fit parameters. However any variation in these values cause corresponding, and linear, change in the scattering lengths. The method of determining these systematic errors was to look at result for several different values of a cut. The systematic error was taken as the difference between the weighted average of the points and the extreme values.

The first cut that was applied was the cut $|\Delta\theta| < 0.02$. Fig. 8.2 shows the small variations in the parameters as the cut is varied from 0.005 up to 0.04. This leads to a systematic error of $^{+0.3}_{-1.0}$ for the linear coefficient and $^{+1.7}_{-0.3}$ for the quadratic coefficient.

The second cut applied was $\min(E_{\gamma 2}, E_{\gamma 4}) > 35$ MeV. As shown in Fig. 8.3, the variations as this cut is changed are more significant. The systematic error is estimated to be $^{+2.7}_{-1.6}$ for the linear coefficient and $^{+4.7}_{-3.3}$ for the quadratic.

The next cut was the on the sum $E_{\gamma 1} + \max(E_{\gamma 2}, E_{\gamma 3})$ <220 MeV. The fit parameters are not sensitive to this cut as shown in Fig. 8.4. The contribution from this cut is $^{+0.7}_{-0.8}$ for the linear and $^{+1.2}_{-1.8}$ for the quadratic.

The opening angle between photons was required to be more than 0.5 rad for each pair of photons. Moving this cut point has little effect on the parameters. The systematic error is found to be $^{+0.4}_{-0.3}$ and $^{+1.3}_{-0.7}$ for the linear and quadratic, respectively. Fig. 8.5 shows the variation of this cut.

The last cut restricted the reconstructed π^0 mass to the region (60,160) MeV. The variation of the lower and upper limits are shown in Fig. 8.6 and 8.7 respectively. The contribution from these two limits are $^{+2.4}_{-1.0}$ and $^{+3.5}_{-1.6}$.

A summary of the above cuts and the resulting error is shown in Table. 8.1.

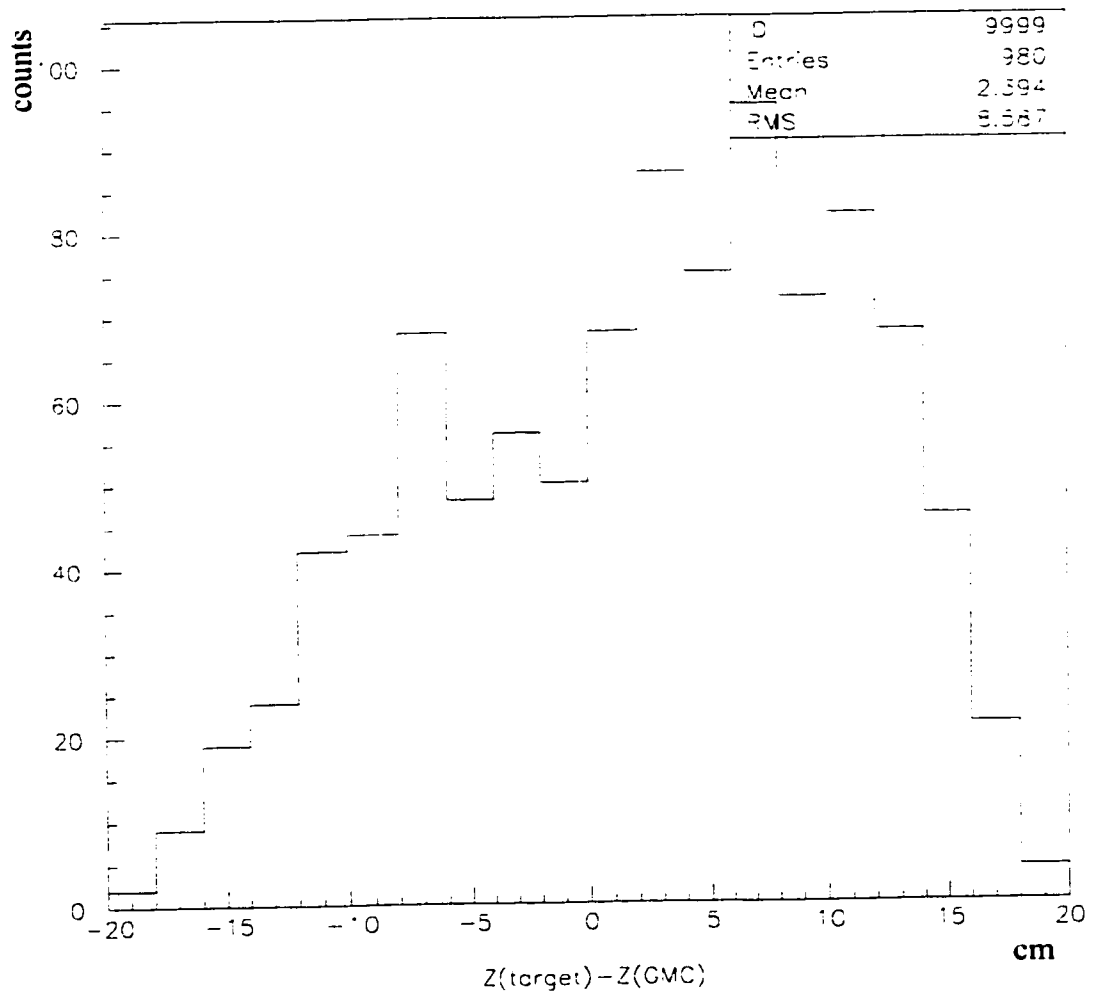

Figure 8.1: The difference between the z coordinate found by the method of section 4.1 and the actual z coordinate from MC simulation.

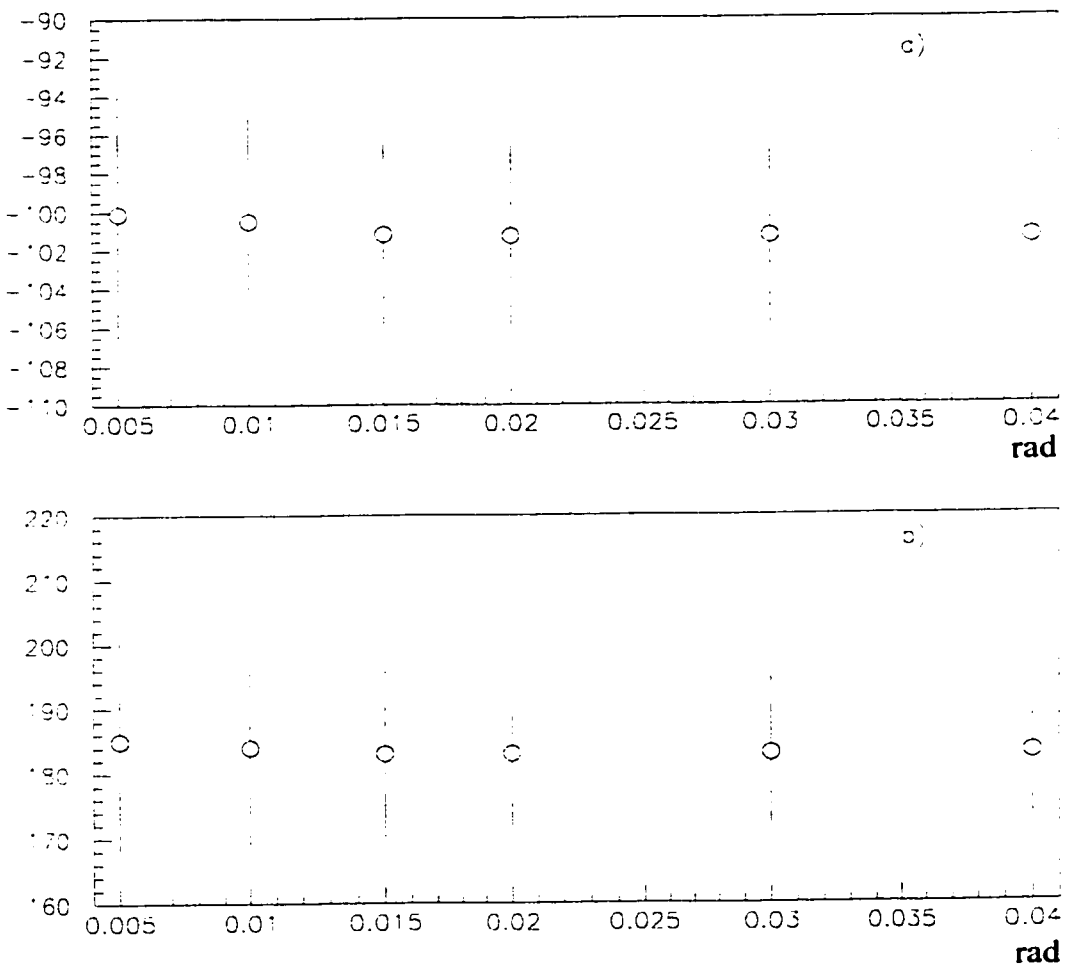

Figure 8.2: The variation of the parameters, a) linear and b) quadratic, as $\Delta\theta$ cut is varied.

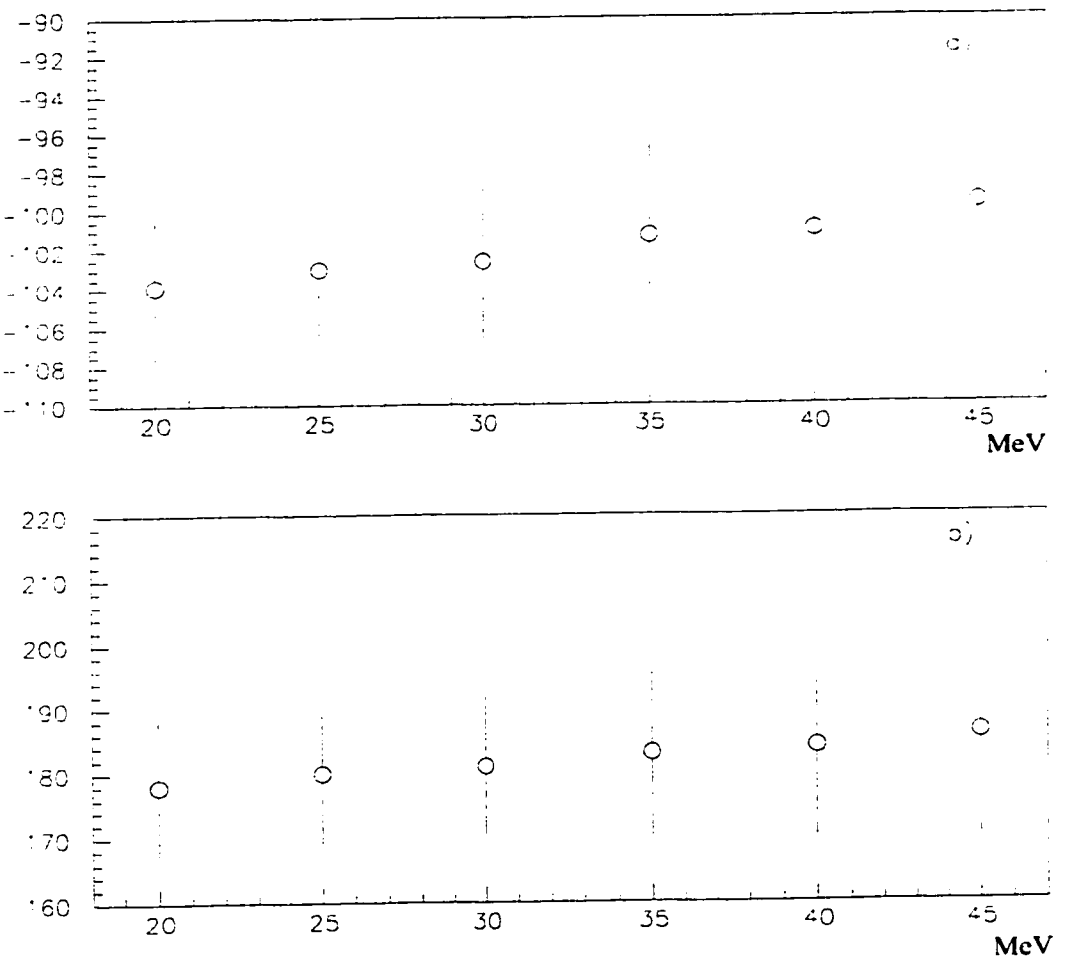

Figure 8.3: The variation of the parameters, a) linear and b) quadratic, as $\min(E_{\gamma 2}, E_{\gamma 4})$ cut is varied.

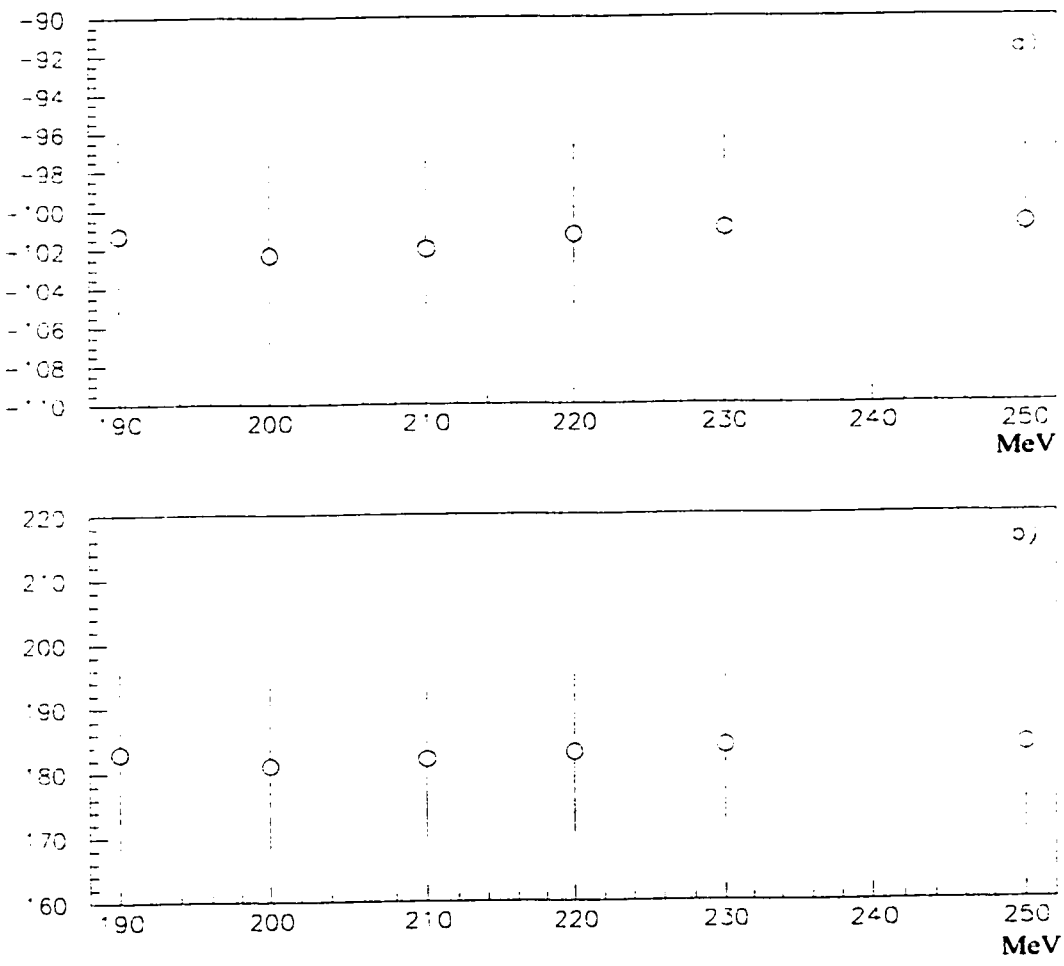

Figure 8.4: The variation of the parameters, a) linear and b) quadratic, as $E_{\gamma 1}$ + max($E_{\gamma 2}$, $E_{\gamma 3}$) cut is varied.

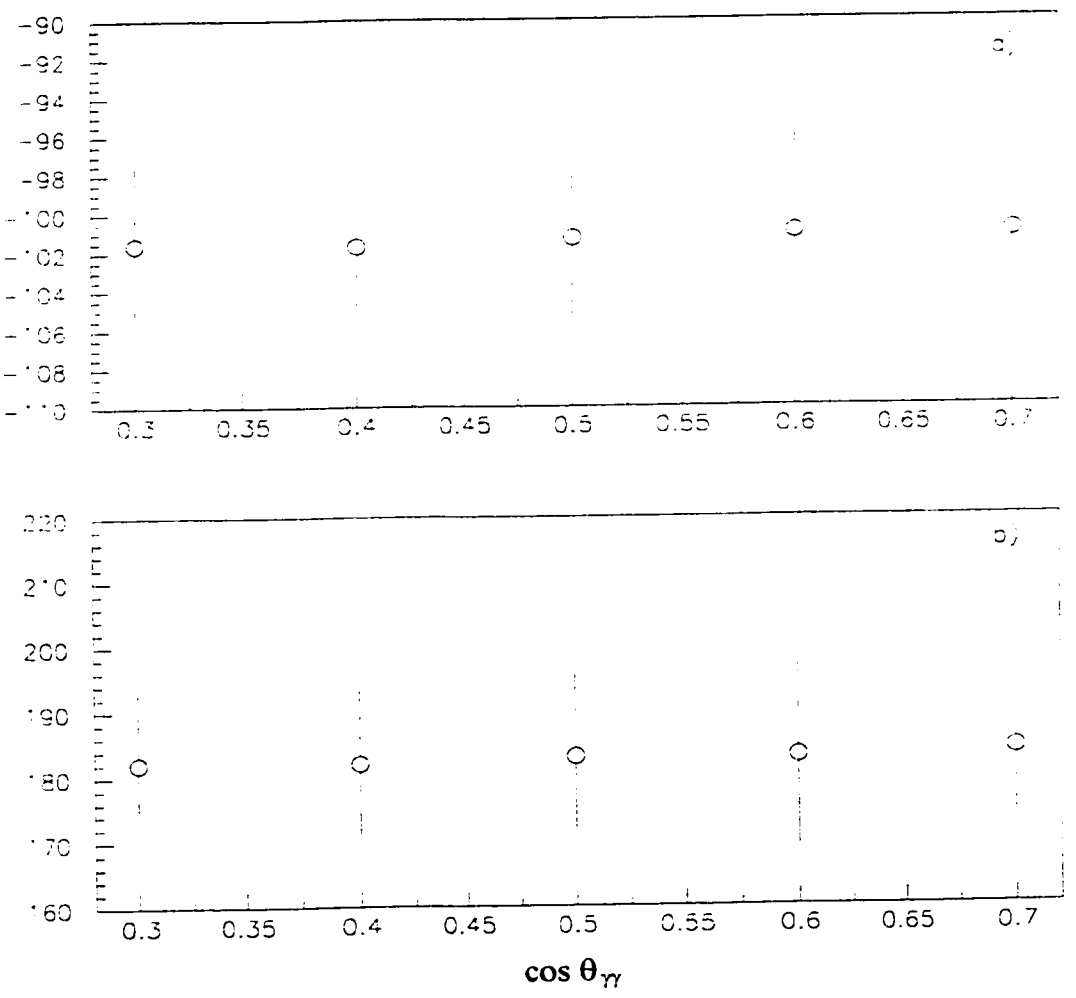

Figure 8.5: The variation of the parameters. a) linear and b) quadratic, as minimum angle is changed.

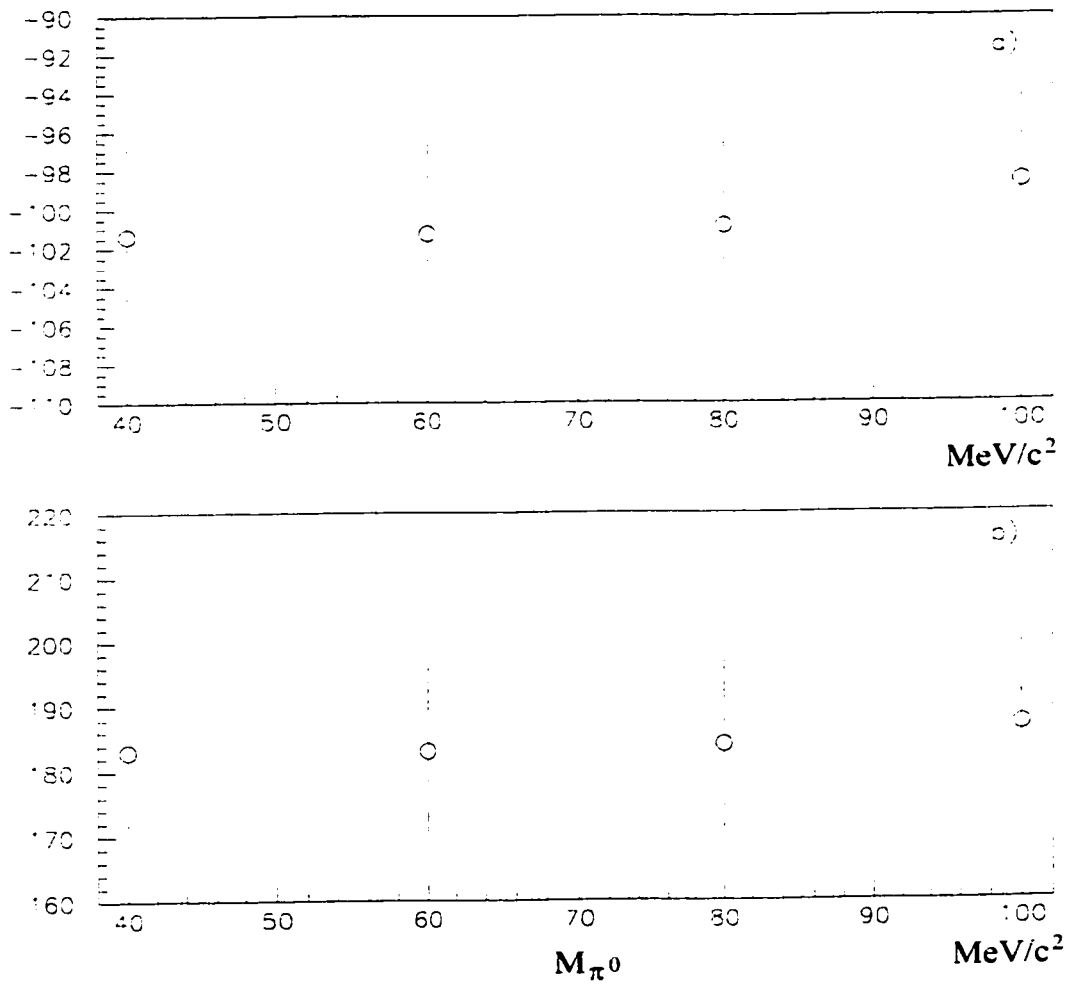

Figure 8.6: The variation of the parameters, a) linear and b) quadratic, as lower limit of the m_{π^0} is changed.

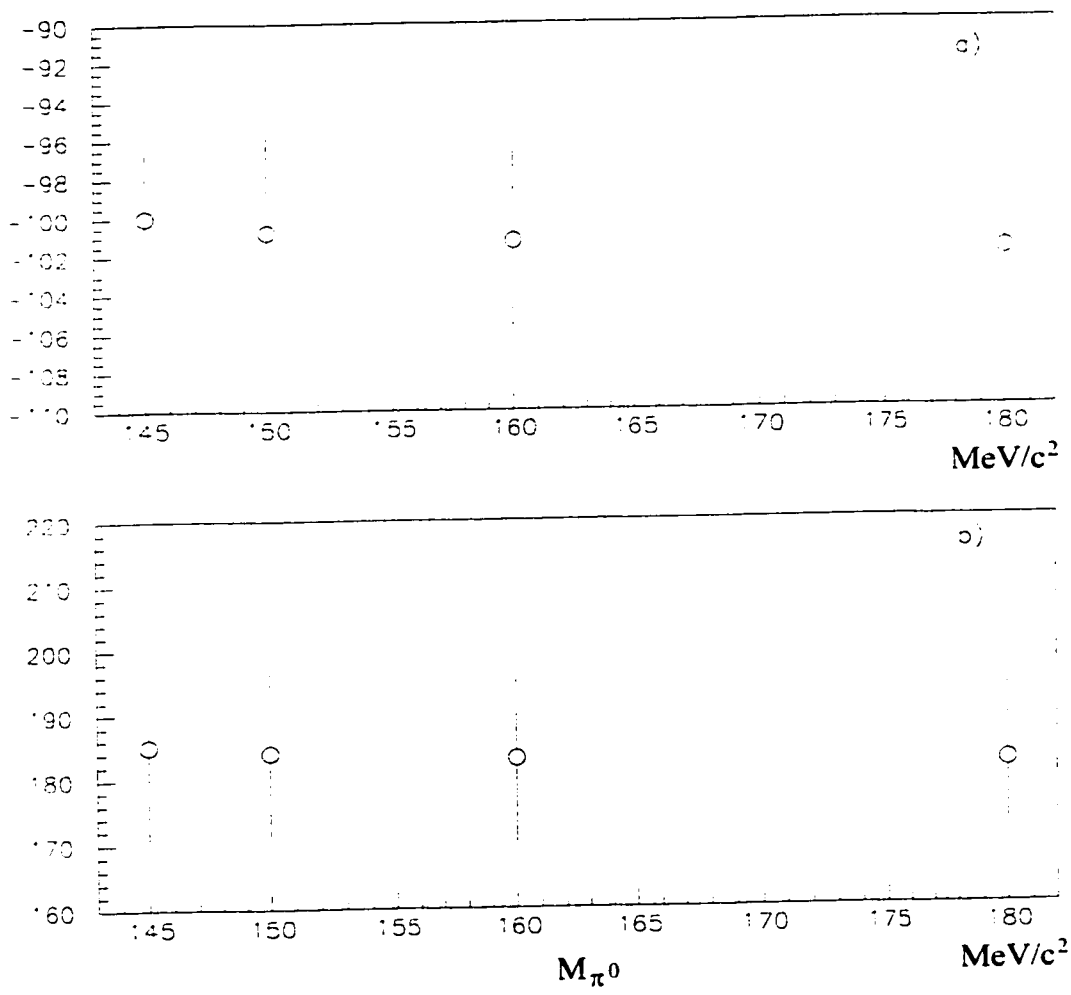

Figure 8.7: The variation of the parameters, a) linear and b) quadratic, as upper limit of the m_{π^0} is changed.

Table 8.1: Summary of the contributions to systematic error to the linear and quadratic fitting parameters.

Cut	Linear		Quadratic	
	upper	lower	upper	lower
$\Delta\theta$	+0.3	-1.0	+1.7	-0.3
$\min(E_{\gamma 2}, E_{\gamma 4})$	+2.7	-1.6	+4.7	-3.3
$E_{\gamma 1} + \max(E_{\gamma 2}, E_{\gamma 3})$	+0.7	-0.8	+1.2	-1.8
Opening Angle	+0.4	-0.3	+1.3	-0.7
m_{π^0}	+2.4	-1.0	+3.5	-1.6

Adding the errors in quadrature yield a total systematic error of $^{+3.8}_{-2.3}$ for the linear term and $^{+6.4}_{-4.1}$ for the quadratic term. These values translate to corresponding errors of ± 0.002 for a_0^0 and $^{+0.0012}_{-0.0007}$ for a_0^2.

Chapter 9

Conclusion

In the present work, the $\pi\pi$ s-wave scattering lengths are determined to be $a_0^0 = 0.199 \pm 0.003(stat) \pm 0.002(syst)$ and $a_0^2 = -0.0285 \pm 0.0008(stat)^{+0.0012}_{-0.0007}(syst)$. from a kinematically complete measurement of the $K_{\pi 3}$ decay spectrum of stopped kaons. A salient feature of this channel is that it is free from hadronic interactions involving baryons, unlike the commonly employed $\pi N \rightarrow \pi\pi N$ channels. Also, the final state was devoid of Coulomb interactions, since there is a single chargd pion in the outgoing channel.

The present measurement constituted a nearly model independent determination of the scattering lengths. since we did not have to use Weinberg's universal curve ($\mathfrak{W} = 2a_0^0 - 5a_0^2$) for deducing a_0^0 and a_0^2 separately. It is quite heartening that $\mathfrak{W} = 0.540 \pm 0.007(stat)^{+0.005}_{-0.007}(syst)$ deduced from our results is in near perfect agreement with the predictioon $\mathfrak{W} = 0.56$.

The Figure 9.1 shows the updated a_0^0 vs. a_0^2 plot, originally presented by Pocanic[15].

In this plot, the experimental results are shown as the ellipses and theoretical results are indicated by points (triangles, squares, stars etc.). We updated the figure of Pocanic to include our result (Kπ3) and also that of the $\pi N \to \pi\pi N$ of Kermani *et. al.*[19].

From the figure, it becomes clear that the experimental results are converging onto the universal curve with $a_0^0 = 0.2$. In fact, the overlap between soft-pion, Kermani and our result is very good.

From the theoretical side, it seems models inspired by chiral perturbation theory, and the Jacob-Scadron model seem to predict the scattering lengths extremely well. More exotic models such as quark loop anomalies (QLAD) are not warranted by the present scattering lengths.

It is perhaps safe to conclude that the present work determined the $\pi\pi$ scattering lengths to a precision high enough to rule out many candidate models and also it is reliable to be useful to hadron phenomenologists.

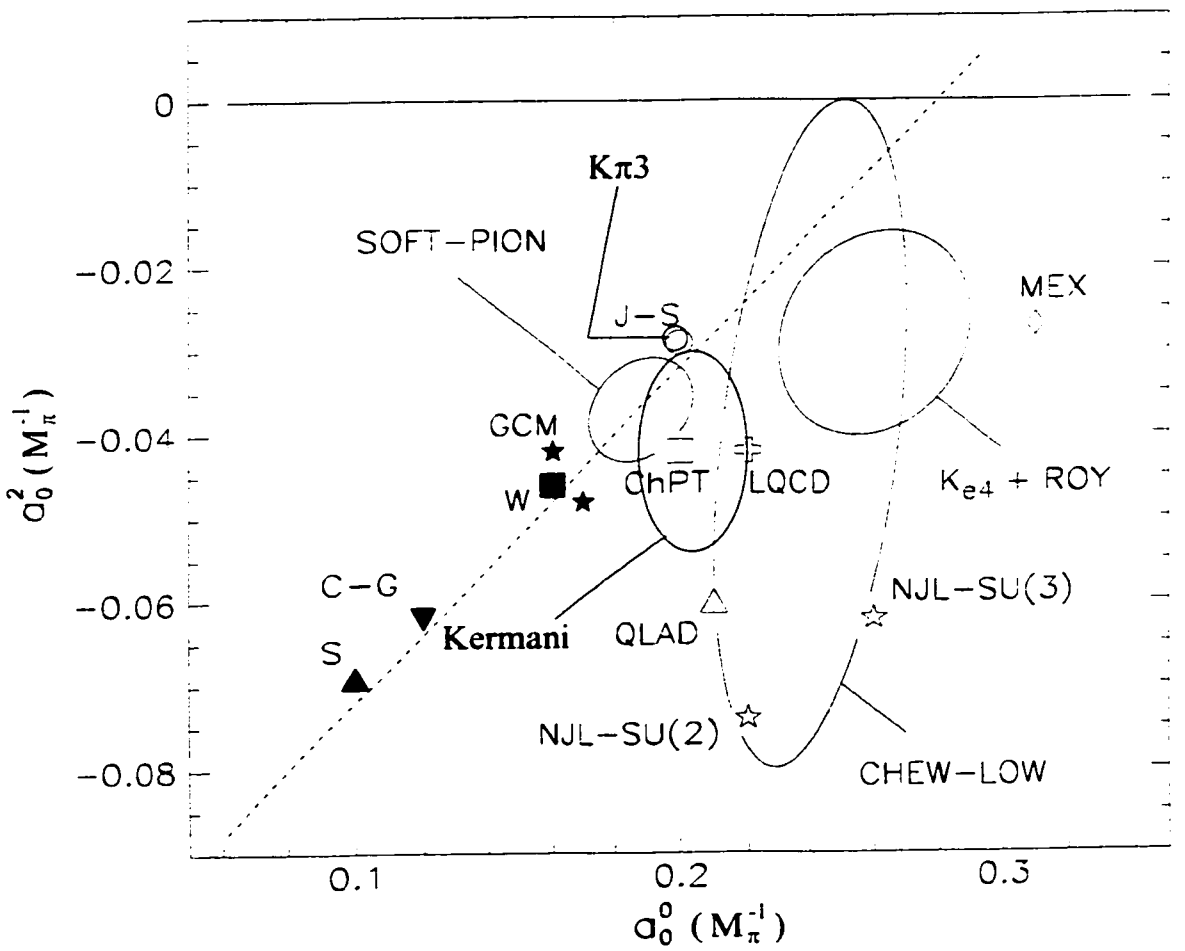

Figure 9.1: Comparison of theoretical predictions (points) and experimental results (ellipses). The models shown are Weinberg (W)[5], Schwinger (S)[6], Chang and Gursey (C-G)[7], Jacob and Scadron (J-S)[8], chiral perturbation theory (ChPT)[9], quark loop anomalies (QLAD)[10], meson exchange (MEX)[11], Nambu-Jona-Lasinio (NJL)[12, 13], global color symmetry (GCM)[14]. Also shown is $\mathfrak{W} = 0.56$ (dotted line). (Adapted from Počanić[15].)

Appendix A

Sample Maple Script

```
> restart;
> s1:= 0.097:  sqrt(s1)/2:  beta:= 0.3-s1; sl:= 0.076:
> low:= sqrt(sl):  sh:= 0.106:  high:= sqrt(sh):
```

$$\beta := .203$$

Setup initial parameters: $s1$ is the midpoint of s_1 slice used. sl and sh give the s_3 range that is being fit.

```
> f:= x -> sqrt(beta-x^2)/2:
```

This function is $\frac{\sqrt{s_2}}{2}$.

```
> alpha1:= (low+high)/2:
> alpha2:= (2*low+alpha1)/3:  alpha3:= (alpha1+7*high)/8:
> L1:= (x-alpha2)*(x-alpha3)/(alpha1-alpha2)/(alpha1-alpha3):
> L2:= (x-alpha1)*(x-alpha3)/(alpha2-alpha1)/(alpha2-alpha3):
> L3:= (x-alpha2)*(x-alpha1)/(alpha3-alpha2)/(alpha3-alpha1):
> po2:= f(alpha1)*L1+f(alpha2)*L2+f(alpha3)*L3:
> po2a:= simplify(po2);
```

$$po2a := -1.367546700\,x^2 + .3730005149\,x + .1792572433$$

Determines an approximation to $\frac{\sqrt{s_2}}{2}$ using Lagrange multipliers.

```
> c1:= coeff(po2,x,0):  c2:= coeff(po2,x,1):  c3:= coeff(po2,x,2):
```

```
> d1:= c1+sqrt(s1)/2; d2:= c2-0.333; d3:= c3;
```

$$d1 := .3349813650$$

$$d2 := .0400005$$

$$d3 := -1.3675467$$

Determine the coefficients of $\frac{\sqrt{s_1}+\sqrt{s_2}}{2} - \frac{\sqrt{s_3}}{3}$.

```
> p1:= 14.9:  er1:= 1.1:  p2:= -101.3:  er2:= 4.7:
```

```
> p3:= 183.:  er3:= 13.:
```

Paremeter results and errors from MINUIT.

```
> eqn1:= c+d1*b+d1**2*b*b/4=p1;
```

$$eqn1 := c + .3349813650\,b + .02805312873\,b^2 = 14.9$$

```
> eqn2:= a/3+d2*b+d1*a*b/6+d1*d2*b*b/2=p2;
```

$$eqn2 := \frac{1}{3}\,a + .0400005\,b + .05583022750\,a\,b + .006699711045\,b^2 = -101.3$$

```
> eqn3:= d3*b+a*a/36+d2*a*b/6+(d2**2+2*d1*d3)*b*b/4=p3;
```

$$eqn3 := -1.3675467\,b + \frac{1}{36}\,a^2 + .006666750000\,a\,b - .2286513202\,b^2 = 183.$$

Three equations relating the fit parameters to the scattering lengths. Note a represents $\frac{a_0^0}{2\lambda_\pi}$ and b is $\frac{a_0^2}{2\lambda_\pi}$.

```
> ans:= [solve({eqn1,eqn2,eqn3},{a,b,c})];
```

$$ans := [\{b = -23.98075344,\ a = 103.6218618,\ c = 6.800409435\},\ \{$$

$$a = -3.188939829 - 49.51971757\,I,\ c = 47.64693976 + 4.323989020\,I,$$

$$b = -3.684814863 - 33.71789217\,I\},\ \{b = -3.684814863 + 33.71789217\,I,$$

$a = -3.188939829 + 49.51971757\,I,\ c = 47.64693976 - 4.323989020\,I\}$,

$\{a = -95.09458202,\ c = 5.331668213,\ b = 13.43893905\}]$

There are 4 solutions to the to these equations. Two of the solutions are complex and therefore ignored. The third solutions yields scattering lengths with the wrong sign.

```
> sol:= ans[4];
```

$$sol := \{a = -95.09458202,\ c = 5.331668213,\ b = 13.43893905\}$$

```
> a1:= subs(sol,a); b1:= subs(sol,b); c1:= subs(sol,c);
```

$$a1 := -95.09458202$$

$$b1 := 13.43893905$$

$$c1 := 5.331668213$$

This is the accepted solution.

```
> eqn2a:= a/3+d2*b+d1*a*b/6+d1*d2*b*b/2=p2+e2:
> eqn1a:= c+d1*b+d1**2*b*b/4=p1+e1:
> eqn3a:= d3*b+a*a/36+d2*a*b/6+(d2**2+2*d1*d3)*b*b/4=p3+e3:
```

These equations are used in determining the errors on a and b from the MINUIT errors.

```
> sola:= [solve({eqn1a,eqn2,eqn3})];
```

$sola := [\{e1 = e1,\ c = 6.800409435 + e1,\ b = -23.98075344,\ a = 103.6218618\},\ \{e1 = e1,$

$c = 47.64693976 + 4.323989020\,I + e1,\ a = -3.188939829 - 49.51971757\,I,$

$b = -3.684814863 - 33.71789217\,I\},\ \{e1 = e1,$

$c = 47.64693976 - 4.323989020\,I + e1,\ b = -3.684814863 + 33.71789217\,I,$

$a = -3.188939829 + 49.51971757\,I\}$,

$\{e1 = e1,\ c = 5.331668213 + e1,\ a = -95.09458202,\ b = 13.43893905\}]$

```
> sola[4];
```

$\{e1 = e1,\ c = 5.331668213 + e1,\ a = -95.09458202,\ b = 13.43893905\}$

As can be seen, the error from the constant does not affect the scattering lengths.

```
> solb:= solve({eqn1,eqn2a,eqn3},{a,b,c}):
> solb1:= subs(solb,a):  solb2:= {allvalues(solb1)}:
> evalf(subs(e2=0.0,solb2[1])); evalf(subs(e2=0.0,solb2[2]));
> evalf(subs(e2=0.0,solb2[3])); evalf(subs(e2=0.0,solb2[4]));
```

$$-3.18893976 + 49.51971453\,I$$

$$-3.18893976 - 49.51971453\,I$$

$$-95.09457804$$

$$103.6218575$$

```
> plot(solb2[3]-a1,e2=-er2..er2);
```

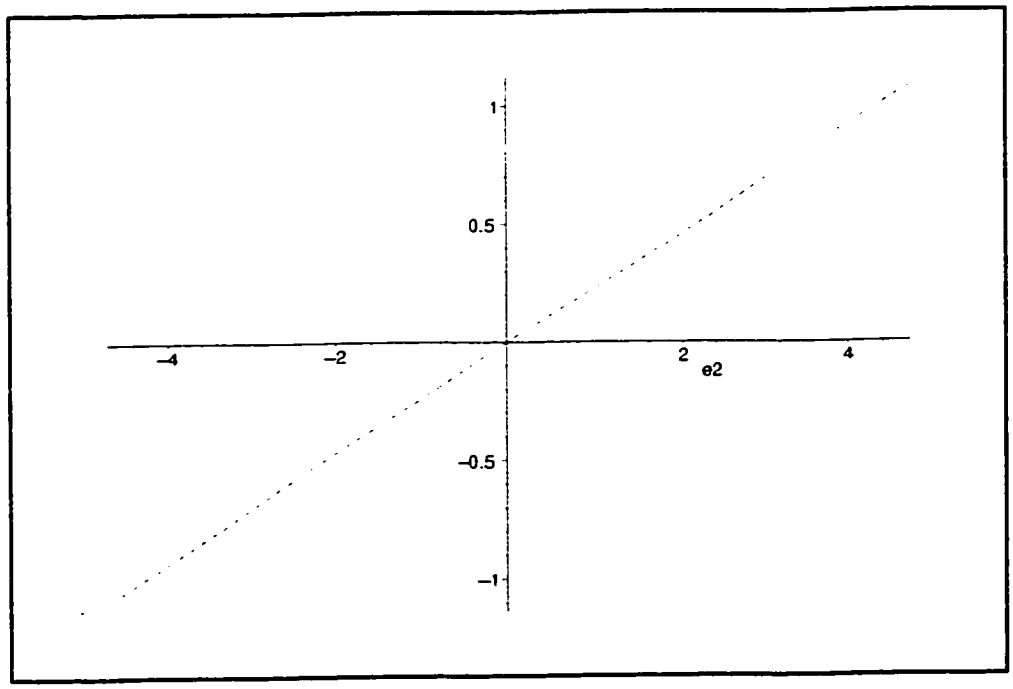

```
> evalf(subs(e2=er2,solb2[3])-a1); evalf(subs(e2=-er2,solb2[3])-a1);
```

$$1.082835263$$

$$-1.08856620$$

This is the error of a due to the error of the linear parameter.

```
> solb1:= subs(solb,b):  solb2:= {allvalues(solb1)}:
> evalf(subs(e2=0.0,solb2[1])); evalf(subs(e2=0.0,solb2[2]));
> evalf(subs(e2=0.0,solb2[3])); evalf(subs(e2=0.0,solb2[4]));
```

$$-3.684814844 + 33.71789191\ I$$

$$-3.684814844 - 33.71789191\ I$$

$$13.43893855$$

$$-23.98075297$$

```
> plot(solb2[3]-b1,e2=-er2..er2);
```

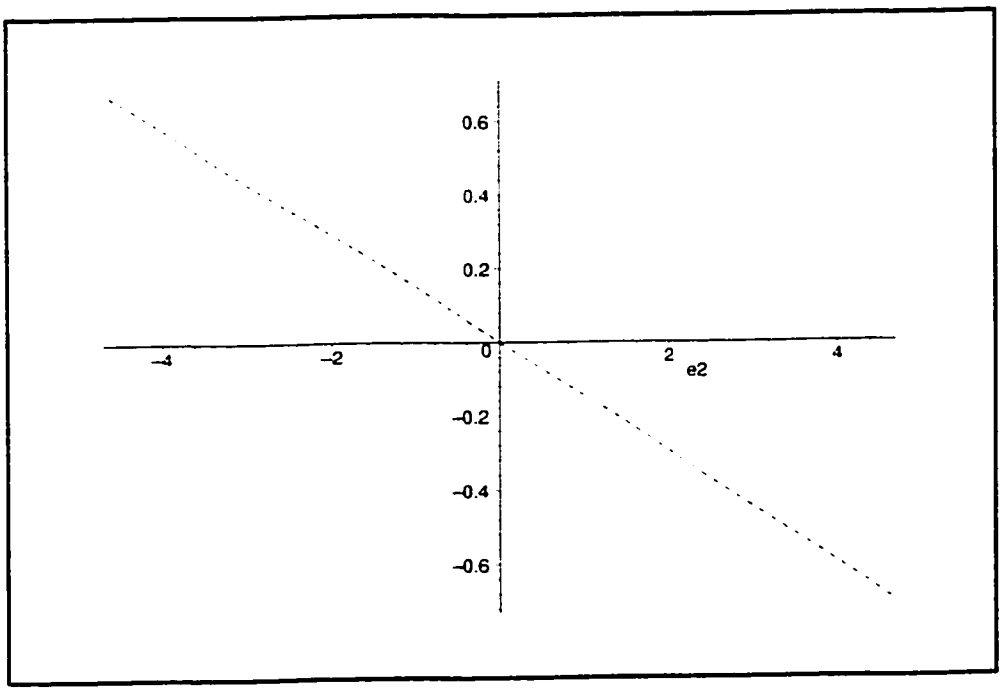

```
> evalf(subs(e2=er2,solb2[3])-b1); evalf(subs(e2=-er2,solb2[3])-b1);
```

$$-.70065387$$

$$.68420081$$

This is the error of b due to the error of the linear parameter

```
> solc:= solve({eqn1,eqn2,eqn3a},{a,b,c}):
> solc1:= subs(solc,a):  solc2:= {allvalues(solc1)}:
> evalf(subs(e3=0.0,solc2[1])); evalf(subs(e3=0.0,solc2[2]));
> evalf(subs(e3=0.0,solc2[3])); evalf(subs(e3=0.0,solc2[4]));
```

$$103.6218575$$

$$-95.09457806$$

$$-3.188939707 - 49.51971454\,I$$

$$-3.188939707 + 49.51971454\,I$$

```
> plot(solc2[2]-a1,e3=-er3..er3);
```

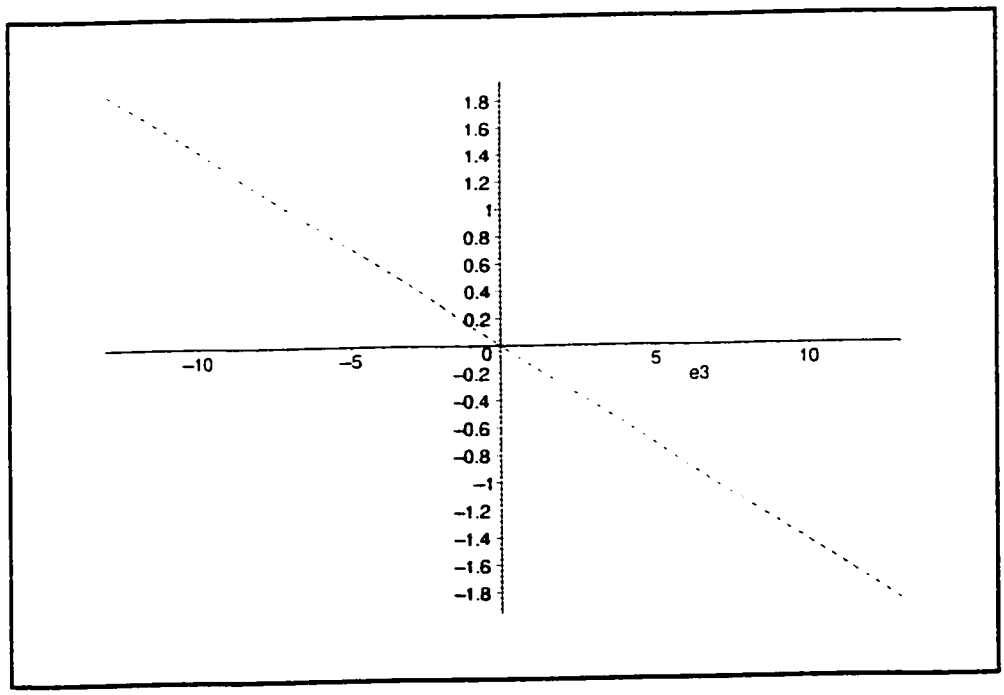

```
> evalf(subs(e3=er3,solc2[2])-a1); evalf(subs(e3=-er3,solc2[2])-a1);
```

$$-1.87631341$$

$$1.87560027$$

This is the error of a due to the error of the quadratic parameter.

```
> solc1:= subs(solc,b):  solc2:= {allvalues(solc1)}:
> evalf(subs(e3=0.0,solc2[1])); evalf(subs(e3=0.0,solc2[2]));
> evalf(subs(e3=0.0,solc2[3])); evalf(subs(e3=0.0,solc2[4]));
```

$$-3.684814844 + 33.71789191\,I$$

$$-23.98075297$$

$$-3.684814844 - 33.71789191\,I$$

$$13.43893855$$

```
> plot(solc2[4]-b1,e3=-er3..er3);
```

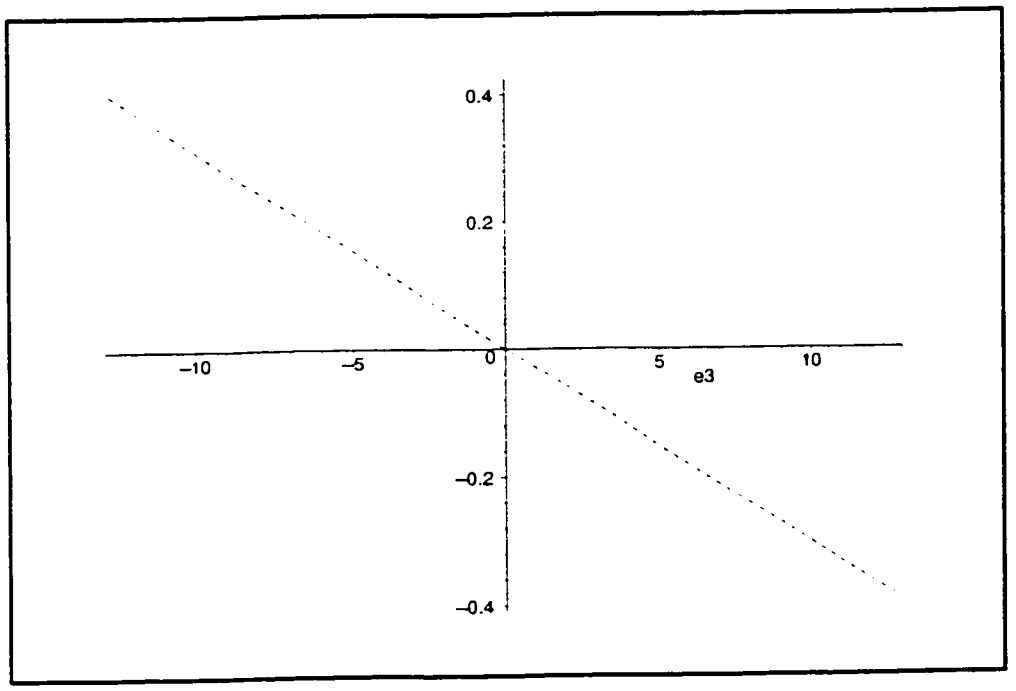

```
> evalf(subs(e3=er3,solc2[4])-b1); evalf(subs(e3=-er3,solc2[4])-b1);
```

$$-.39127454$$

$$.40798960$$

This is the error of b due to the error of the quadratic parameter.

The rest of this section shows additional sources of errors. First due to the finite width of the s1 slices.

```
> s1a:= s1+0.003; beta_a:= 0.3-s1a; fa:= x -> sqrt(beta_a-x^2)/2:
> po2:= fa(alpha1)*L1+fa(alpha2)*L2+fa(alpha3)*L3:
> po2a:= simplify(po2):  c1:= coeff(po2,x,0):  c2:= coeff(po2,x,1):
> c3:= coeff(po2,x,2):  d1:= c1+sqrt(s1)/2:  d2:= c2-0.333:  d3:= c3:
> eqn1:= c+d1*b+d1**2*b*b/4=p1:
> eqn2:= a/3+d2*b+d1*a*b/6+d1*d2*b*b/2=p2:
> eqn3:= d3*b+a*a/36+d2*a*b/6+(d2**2+2*d1*d3)*b*b/4=p3:
> ans:= [solve({eqn1,eqn2,eqn3},{a,b,c})]; sol:= ans[4];
> a1a:= subs(sol,a)-a1; b1a:= subs(sol,b)-b1; c1a:= subs(sol,c)-c1;
```

$$s1a := .100$$

$$beta\_a := .200$$

$$ans := [\{b = -24.15567169,\ c = 6.891614714,\ a = 105.2877189\},\ \{$$
$$c = 46.74412578 + 4.242090868\,I,\ a = -3.094898522 - 48.72354473\,I,$$
$$b = -3.736683675 - 33.60572987\,I\},\ \{a = -3.094898522 + 48.72354473\,I,$$
$$b = -3.736683675 + 33.60572987\,I,\ c = 46.74412578 - 4.242090868\,I\},$$
$$\{a = -96.07282119,\ c = 5.406522943,\ b = 13.51861134\}]$$

$$sol := \{a = -96.07282119,\ c = 5.406522943,\ b = 13.51861134\}$$

$$a1a := -.97823917$$

$$b1a := .07967229$$

$$c1a := 5.230946213$$

```
> s1a:= s1-0.003; beta_a:= 0.3-s1a; fa:= x -> sqrt(beta_a-x^2)/2:
> po2:= fa(alpha1)*L1+fa(alpha2)*L2+fa(alpha3)*L3:
> o2a:= simplify(po2):  c1:= coeff(po2,x,0):  c2:= coeff(po2,x,1):
> c3:= coeff(po2,x,2):  d1:= c1+sqrt(s1)/2:  d2:= c2-0.333:  d3:= c3:
> eqn1:= c+d1*b+d1**2*b*b/4=p1:
> eqn2:= a/3+d2*b+d1*a*b/6+d1*d2*b*b/2=p2:
> eqn3:= d3*b+a*a/36+d2*a*b/6+(d2**2+2*d1*d3)*b*b/4=p3:
> ans:= [solve({eqn1,eqn2,eqn3},{a,b,c})]; sol:= ans[4];
> a1a:= subs(sol,a)-a1; b1a:= subs(sol,b)-b1; c1a:= subs(sol,c)-c1;
```

$$s1a := .094$$

$$beta\_a := .206$$

$$ans := [\{a = 102.0754701,\ b = -23.81578089,\ c = 6.713094886\},\ \{$$
$$a = -3.271542570 - 50.25875781\,I,\ b = -3.636050936 - 33.83250932\,I,$$
$$c = 48.54368670 + 4.404426308\,I\},\ \{a = -3.271542570 + 50.25875781\,I,$$
$$b = -3.636050936 + 33.83250932\,I,\ c = 48.54368670 - 4.404426308\,I\},$$
$$\{a = -94.18440927,\ c = 5.260361383,\ b = 13.36337121\}]$$

$$sol := \{a = -94.18440927,\ c = 5.260361383,\ b = 13.36337121\}$$

$$a1a := .91017275$$

$$b1a := -.07556784$$

$$c1a := 5.077571233$$

Next is the error due to approximation of $\frac{\sqrt{s_2}}{2}$. Since the approximation is crudely optimized over the fitting range, the range is changed by a half a bin width.

```
> lowa:= sqrt(s1-0.003):  alpha1:= (lowa+high)/2:
> alpha2:= (2*lowa+alpha1)/3:  alpha3:= (alpha1+7*high)/8:
> L1:= (x-alpha2)*(x-alpha3)/(alpha1-alpha2)/(alpha1-alpha3):
> L2:= (x-alpha1)*(x-alpha3)/(alpha2-alpha1)/(alpha2-alpha3):
> L3:= (x-alpha2)*(x-alpha1)/(alpha3-alpha2)/(alpha3-alpha1):
> po2:= f(alpha1)*L1+f(alpha2)*L2+f(alpha3)*L3:
> po2a:= simplify(po2):  c1:= coeff(po2,x,0):  c2:= coeff(po2,x,1):
> c3:= coeff(po2,x,2):  d1:= c1+sqrt(s1)/2:  d2:= c2-0.333:  d3:= c3:
> eqn1:= c+d1*b+d1**2*b*b/4=p1:
> eqn2:= a/3+d2*b+d1*a*b/6+d1*d2*b*b/2=p2:
> eqn3:= d3*b+a*a/36+d2*a*b/6+(d2**2+2*d1*d3)*b*b/4=p3:
> ans:= [solve({eqn1,eqn2,eqn3},{a,b,c})]; sol:= ans[4];
> a1a:= subs(sol,a)-a1; b1a:= subs(sol,b)-b1; c1a:= subs(sol,c)-c1;
```

$$ans := [\{b = -23.86771626,\ a = 102.0695785,\ c = 6.734078514\},\ \{$$

$$c = 48.32518677 + 4.384909251\,I,\ b = -3.649604149 - 33.82202858\,I,$$

$$a = -3.309416068 - 50.61212961\,I\},\ \{c = 48.32518677 - 4.384909251\,I,$$

$$b = -3.649604149 + 33.82202858\,I,\ a = -3.309416068 + 50.61212961\,I\},$$

$$\{b = 13.38848542,\ c = 5.277466293,\ a = -94.19143875\}]$$

$$sol := \{b = 13.38848542,\ c = 5.277466293,\ a = -94.19143875\}$$

$$a1a := .90314327$$

$$b1a := -.05045363$$

$$c1a := 5.095702963$$

```
> lowa:= sqrt(sl+0.003):  alpha1:= (lowa+high)/2:
> alpha2:= (2*lowa+alpha1)/3:  alpha3:= (alpha1+7*high)/8:
> L1:= (x-alpha2)*(x-alpha3)/(alpha1-alpha2)/(alpha1-alpha3):
> L2:= (x-alpha1)*(x-alpha3)/(alpha2-alpha1)/(alpha2-alpha3):
> L3:= (x-alpha2)*(x-alpha1)/(alpha3-alpha2)/(alpha3-alpha1):
> po2:= f(alpha1)*L1+f(alpha2)*L2+f(alpha3)*L3:
> po2a:= simplify(po2):  c1:= coeff(po2,x,0):  c2:= coeff(po2,x,1):
> c3:= coeff(po2,x,2):  d1:= c1+sqrt(s1)/2:  d2:= c2-0.333:  d3:= c3:
> eqn1:= c+d1*b+d1**2*b*b/4=p1:
> eqn2:= a/3+d2*b+d1*a*b/6+d1*d2*b*b/2=p2:
> eqn3:= d3*b+a*a/36+d2*a*b/6+(d2**2+2*d1*d3)*b*b/4=p3:
> ans:= [solve({eqn1,eqn2,eqn3},{a,b,c})]; sol:= ans[4];
> a1a:= subs(sol,a)-a1; b1a:= subs(sol,b)-b1; c1a:= subs(sol,c)-c1;
```

$$ans := [\{a = 105.2361883,\ c = 6.868076561,\ b = -24.10107695\},\ \{$$

$$c = 46.97391100 + 4.263024464\,I,\ b = -3.721784887 - 33.62112454\,I,$$

$$a = -3.060736099 - 48.39656178\,I\},\ \{b = -3.721784887 + 33.62112454\,I,$$

$$c = 46.97391100 - 4.263024464\,I,\ a = -3.060736099 + 48.39656178\,I\},$$

$$\{a = -96.03228522,\ c = 5.387168321,\ b = 13.49282926\}]$$

$$sol := \{a = -96.03228522,\ c = 5.387168321,\ b = 13.49282926\}$$

$$a1a := -.93770320$$

$$b1a := .05389021$$

$$c1a := 5.210515931$$

```
> higha:= sqrt(sh-0.003):  alpha1:= (low+higha)/2:
> alpha2:= (2*low+alpha1)/3:  alpha3:= (alpha1+7*higha)/8:
> L1:= (x-alpha2)*(x-alpha3)/(alpha1-alpha2)/(alpha1-alpha3):
```

```
> L2:= (x-alpha1)*(x-alpha3)/(alpha2-alpha1)/(alpha2-alpha3):
> L3:= (x-alpha2)*(x-alpha1)/(alpha3-alpha2)/(alpha3-alpha1):
> po2:= f(alpha1)*L1+f(alpha2)*L2+f(alpha3)*L3:
> po2a:= simplify(po2):  c1:= coeff(po2,x,0):  c2:= coeff(po2,x,1):
> c3:= coeff(po2,x,2):  d1:= c1+sqrt(s1)/2:  d2:= c2-0.333:  d3:= c3:
> eqn1:= c+d1*b+d1**2*b*b/4=p1:
> eqn2:= a/3+d2*b+d1*a*b/6+d1*d2*b*b/2=p2:
> eqn3:= d3*b+a*a/36+d2*a*b/6+(d2**2+2*d1*d3)*b*b/4=p3:
> ans:= [solve({eqn1,eqn2,eqn3},{a,b,c})]; sol:= ans[4];
> a1a:= subs(sol,a)-a1; b1a:= subs(sol,b)-b1; c1a:= subs(sol,c)-c1;
```

$$ans := [\{a = 102.0318993,\ b = -23.87228983,\ c = 6.731591569\},\ \{$$

$$a = -3.310785277 - 50.62465418\,I,\ c = 48.35098264 + 4.387216143\,I,$$

$$b = -3.649636313 - 33.83847142\,I\},\ \{c = 48.35098264 - 4.387216143\,I,$$

$$a = -3.310785277 + 50.62465418\,I,\ b = -3.649636313 + 33.83847142\,I\},$$

$$\{b = 13.39152964,\ a = -94.16907261,\ c = 5.275438004\}]$$

$$sol := \{b = 13.39152964,\ a = -94.16907261,\ c = 5.275438004\}$$

$$a1a := .92550941$$

$$b1a := -.04740941$$

$$c1a := 5.093704924$$

```
> higha:= sqrt(sh+0.003):  alpha1:= (low+higha)/2:
> alpha2:= (2*low+alpha1)/3:  alpha3:= (alpha1+7*higha)/8:
> L1:= (x-alpha2)*(x-alpha3)/(alpha1-alpha2)/(alpha1-alpha3):
> L2:= (x-alpha1)*(x-alpha3)/(alpha2-alpha1)/(alpha2-alpha3):
> L3:= (x-alpha2)*(x-alpha1)/(alpha3-alpha2)/(alpha3-alpha1):
> po2:= f(alpha1)*L1+f(alpha2)*L2+f(alpha3)*L3:
```

```
> po2a:= simplify(po2):  c1:= coeff(po2,x,0):  c2:= coeff(po2,x,1):
> c3:= coeff(po2,x,2):  d1:= c1+sqrt(s1)/2:  d2:= c2-0.333:  d3:= c3:
> eqn1:= c+d1*b+d1**2*b*b/4=p1:
> eqn2:= a/3+d2*b+d1*a*b/6+d1*d2*b*b/2=p2:
> eqn3:= d3*b+a*a/36+d2*a*b/6+(d2**2+2*d1*d3)*b*b/4=p3:
> ans:= [solve({eqn1,eqn2,eqn3},{a,b,c})]; sol:= ans[4];
> a1a:= subs(sol,a)-a1; b1a:= subs(sol,b)-b1; c1a:= subs(sol,c)-c1;
```

$$ans := [\{c = 6.871157088,\ b = -24.09733518,\ a = 105.2897838\},\ \{$$

$$b = -3.722050794 - 33.60391787\ I,\ c = 46.94371283 + 4.260276877\ I,$$

$$a = -3.057958867 - 48.37400317\ I\},\ \{b = -3.722050794 + 33.60391787\ I,$$

$$c = 46.94371283 - 4.260276877\ I,\ a = -3.057958867 + 48.37400317\ I\},$$

$$\{c = 5.389699903,\ b = 13.49011189,\ a = -96.06381360\}]$$

$$sol := \{c = 5.389699903,\ b = 13.49011189,\ a = -96.06381360\}$$

$$a1a := -.96923158$$

$$b1a := .05117284$$

$$c1a := 5.213038443$$

Bibliography

[1] L. Rosselet *et al.*, Phys. Rev. D **15**, 574 (1977).

[2] R. F. Sawyer and K. C. Wali, Phys. Rev. **119**, 1429 (1960).

[3] G. F. Chew and S. Mandlestam, Phys. Rev. **119**, 467 (1960).

[4] J. Imazato *et al.*, KEK Report 91-8, KEK, Tsukuba, Japan, 1991.

[5] S. Weinberg, Phys. Rev. Lett. **17**, 616 (1966).

[6] J. Schwinger, Phys. Lett. **24B**, 473 (1967).

[7] P. Chang and F. Gürsey, Phys. Rev. **164**, 1752 (1967).

[8] R. Jacob and M. D. Scadron, Phys. Rev. D **25**, 3073 (1982).

[9] J. Gasser and H. Leutwyler, Phys. Lett. B **125**, 325 (1983).

[10] A. N. Ivanov and N. I. Troitskaya, Sov. J. Nucl. Phys. **43**, 260 (1986).

[11] D. Lohse, J. W. Durso, K. Holinde, and J. Speth, Nucl. Phys. **A516**, 513 (1990).

[12] M. C. Ruivo, C. A. de Sousa, B. Hiller, and A. H. Blin, Nucl. Phys. **A575**, 460 (1994).

[13] V. Bernard, U.-G. Meißner, A. H. Blin, and B. Hiller, Phys. Lett. B **253**, 443 (1991).

[14] C. D. Roberts, R. T. Cahill, M. E. Sevior, and N. Iannella, Phys. Rev. D **49**, 125 (1994).

[15] D. Počanić, in *Chiral Dynamics, Theory, and Experiment*, Vol. 452 of *Lect. Notes in Phys.*, edited by A. M. Bernstein and B. R. Holstein (Springer Verl., Berlin, 1995), p. 95.

[16] E. Segre, *Nuclei and Particles*, 2 ed. (Benjamin/Cummings Publishing Company, Reading, Massachusetts, 1977).

[17] G. F. Chew and F. E. Low, Phys. Rev. **113**, 1640 (1959).

[18] E. A. Alekseeva *et al.*, Sov. Phys. JETP **55**, 591 (1982).

[19] M. Kermani *et al.*, Phys. Rev. C **58**, 3431 (1998).

[20] M. G. Olsson and L. Turner, Phys. Rev. **181**, 2141 (1969).

[21] J. Lowe *et al.*, Phys. Rev. C **44**, 956 (1991).

[22] J. L. Basdevant, C. D. Froggatt, and J. L. Peterson, Nucl. Phys. **B72**, 413 (1974).

[23] M. M. Nagels *et al.*, Nucl. Phys. **B147**, 189 (1979).

[24] Y. Kuramashi *et al.*, Phys. Rev. Lett. **71**, 2387 (1993).

[25] B. R. Martin, D. Morgan, and G. Shaw. *Pion-Pion Interactions in Particle Physics* (Academic Press, London, 1976).

[26] S. M. Roy, Phys. Lett. B **36**, 353 (1971).

[27] S. Weinberg, Phys. Rev. **166**, 1568 (1968).

[28] J. Gasser and H. Leutwyler, Ann. Phys. **158**, 142 (1984).

[29] G. D'Ambrosio and G. Isidori, Int. J. Mod. Phys. **A13**, 1 (1998).

[30] J. Goldstone, Nuovo Cimento **19**, 154 (1961).

[31] Y. Nambu and G. Jona-Lasinio, Phys. Rev. **122**, 345 (1961).

[32] J. Bardeen, L. N. Cooper, and J. R. Schrieffer, Phys. Rev. **106**, 162 (1957).

[33] J. J. Sakurai, Phys. Rev. **109**, 980 (1958).

[34] C. R. Mindas, Ph.D. thesis, Princeton University, 1998.

[35] P. D. Group, Phys. Rev. D **45**, 1 (1992).

[36] M. Aoki *et al.*, E246 Technote #11, 1993.

[37] J. Imazato, private Communication.